UNIVERSIDAD NACIONAL AUTÓNOMA DE MÉXICO

PROGRAMA DE MAESTRÍA Y DOCTORADO EN CIENCIAS MATEMÁTICAS Y DE LA ESPECIALIZACIÓN EN ESTADÍSTICA APLICADA

A NEW TWO-DIMENSIONAL BLOOD FLOW MODEL WITH ARBITRARY CROSS SECTIONS & GENERALIZED QUASI-GEOSTROPHY FOR MOIST SPATIALLY ANISOTROPIC ATMOSPHERIC FLOWS WITH PHASE CHANGE

T E S I S

QUE PARA OPTAR POR EL GRADO DE

DOCTOR EN CIENCIAS

PRESENTA:
CESAR ALBERTO ROSALES ALCANTAR

TUTOR PRINCIPAL
DR. GERARDO HERNÁNDEZ DUEÑAS (*INSTITUTO DE MATEMÁTICAS, UNAM*)

COMITÉ TUTOR:
DR. JORGE X. VELASCO HERNÁNDEZ (*INSTITUTO DE MATEMÁTICAS, UNAM*)
DR. RAMÓN GABRIEL PLAZA VILLEGAS (*INSTITUTO DE INVESTIGACIONES EN MATEMÁTICAS APLICADAS Y EN SISTEMAS, UNAM*)

CIUDAD UNIVERSITARIA, CD. MX., MARZO DE 2023

"Entre Dios y la ciencia no encontramos jamás una contradiccón. No se exculyen, como algunos piensan hoy, se complementan y se condicionan mutuamente."

Max Planck

A mis seres queridos que durante estos años han estado conmigo, en las buenas y en las malas, en encierro y en festejo, me brindaron la sabiduría, la gracia, la paciencia y la paz para concluir este escrito. GRACIAS.

Agradecimientos

"Nadie es capaz de llegar al conocimiento de asuntos divinos y humanos si no ha aprendido previamente a fondo las matemáticas."

San Agustín

Quisiera comenzar este agradecimiento dando gracias a Dios, por fortalecerme en los momentos de debilidad, enseñarme el camino de la rectitud, lealtad, fidelidad y perseverancia.

Agradezco a todo el personal administrativo y académico del Instituto de Matemáticas, Unidad Juriquilla, por el cobijo brindado y el apoyo solidario durante el desarrollo de mi proyecto doctoral. En especial, agradezco al Dr. Guillermo Ramírez Santiago por su confianza en las labores de divulgación y difusión científica.

A mis compañeros de posgrado, Valentín, Jose María, Eduardo, Joan Carlos, Ruth y Zamantha, con los cuales compartí momentos de discusión amenos acompañados siempre de un buen café o té y un pizarrón.

A mi director de tesis, Dr. Gerardo Hernández Dueñas, el cual me ha guiado con su experiencia y puntos de vista para la realización de ambos proyectos doctorales y que me ha encaminado en este fascinante mundo de la matemática aplicada y la dinámica de fluidos.

A mis sinodales, Dr. Ramón Gabriel Plaza Villegas, Dr. Marcos Aurelio Capistrán Ocampo, Dr. Miguel Ángel Moreles Vázquez y Dra. Nelly Selem Mujica, por sus valiosas aportaciones a la revisión de mi escrito final y las discusiones sobre la prespectiva de la matemática aplicada.

A mi familia, que durante esta época virtual-remota han sido mi sostén emocional y mental. A mi madre, Prudencia Alcantar Encinas, le agradezco su paciencia. A mi padre, Francisco Javier Rosales Navarro, le agradezco su serenidad. A mi esposa, Guadalupe Morales Ramírez, le agradezco su amor incondicional.

Al Consejo Nacional de Ciencia y Tecnología de México, bajo la beca nacional 701892, por solventar gastos de manutención por estos 4 años para lograr este objetivo. Así mismo, agradezco los fondos complementarios de parte de los proyectos UNAM-DGAPA-PAPIIT IN112222 y Conacyt A1-S-17634, con los cuales se realizaron asistencia a congresos y talleres de cómputo de alto rendimiento.

Al Laboratorio Nacional de Visualización Científica Avanzada de UNAM Campus Juriquilla, por el soporte técnico de parte de Luis Aguilar, Alejandro de León y Jair García.

A todas las personas y amigos que he conocido a lo largo de estos años a lo largo del país y del mundo, en mis viajes matemáticos, les dedico este trabajo.

César Alberto Rosales Alcantar

Santiago de Querétaro, Querétaro de Arteaga, México a 12 de febrero de 2023.

Contents

Introduction - Motivations

A mathematical model is a description of a system using mathematical concepts and language. The process of developing a mathematical model is termed mathematical modeling. Mathematical modeling has proven to be a key tool in many areas of science. It has helped us understanding a big variety of phenomena in our world. Mathematical models are used in the natural sciences (such as physics, biology, earth science, chemistry) and engineering disciplines (such as computer science, electrical engineering), as well as in non-physical systems such as the social sciences (such as economics, psychology, geography).

Some models are based on rates of change due to physical laws. Mathematically, many of them are written as partial differential equations (PDEs). In this thesis, we will derive and analyze two new models in two different scenarios. Part I of this thesis is related to the first model where we will analyze blood flows passing through arteries, and Part II is devoted to deriving simplified model to understand certain physical processes involved in the time evolution of atmospheric phenomena.

Although both circumstances can be analyzed with PDE-based models, their nature is somewhat different. In this thesis, we describe the properties of the model and propose robust and precise numerical schemes to approximate the solutions to such models.

Part I: A new two-dimensional blood flow model with arbitrary cross-section

Cardiovascular diseases are a class of illness that involves the heart or blood vessels. The underlying mechanisms vary depending on the disease. It is estimated that dietary risk factors are associated with 53% of related deaths. It includes coronary artery diseases such as angina and myocardial infarctions, strokes, heart failures, hypertensive heart diseases, rheumatic heart diseases, cardiomyopathies, abnormal heart rhythms, congenital heart diseases, valvular heart diseases, carditis, aortic aneurysms, peripheral artery diseases, thromboembolic diseases, and venous thrombosis among others.

Coronary artery disease, stroke, and peripheral artery disease involve atherosclerosis. This may be caused by high blood pressure, smoking, diabetes mellitus, lack of exercise, obesity, high blood cholesterol, poor diet, excessive alcohol consumption, and poor sleep, among other things. It is estimated that up to 90% of cardiovascular diseases may be preventable. Prevention of such diseases involves improving risk factors through: healthy eating, exercise, avoidance of tobacco smoke and limiting alcohol intake.

Cardiovascular diseases are the leading cause of death worldwide except Africa [1]. Their impact in our lives has motivated the development of different models for blood flows. In [2], a review of recent contributions towards the modeling of vascular flows is provided. A review of contributions regarding the mathematical modeling of the cardiovascular system is presented in [3]. In particular, the challenges in the mathematical modeling both for the arterial circulation and the hearth function are discussed. See also the notes in [4] for more on mathematical modeling and numerical simulation of the cardiovascular system. In [5], an open-source software framework for cardiovascular integrated modeling and simulation (CRIMSON) is described, which is a tool to perform three-dimensional and reduced-order computational haemodynamics studies for real world problems.

Three dimensional (3D) models provide very detailed information of the fluid's evolution. In [6], fluid velocities were measured by laser Doppler velocimetry under conditions of pulsatile flow and such measurements were compared to those given by steady flow conditions. In [7], anatomic and physiologic models are obtained with the aid of 3D imaging techniques for patient-specific modeling. However, 3D simulations are computationally

expensive and often not a practical tool for a timely evaluation before a surgical treatment. This has motivated the development of 1D models which reasonably well describe the propagation of pressure waves in arteries [8]. A 1D hyperbolic model for compliant axi-symmetric idealized vessels is derived in [9] and the properties of the model are discussed. The analysis of the blood flow after an endovascular repair is studied in [10], in which case the PDE based model has discontinuous coefficients. Furthermore, effects of viscous dissipation, viscosity of the fluid and other two dimensional effects were incorporated in a 'one-and-a-half dimensional' model in [11], where it is not necessary to prescribe an axial velocity profile *a priori*. In [12], a coupled model that describes the interaction between a shell and a mesh-like structure is derived. The structure consists of 3D mesh-like elastic objects and the model embodies a 2D shell model and a 1D network model. Well-balanced high-order numerical schemes for one-dimensional (1D) blood flow models are constructed in [13] using the Generalized Hydrostatic Reconstruction technique. Arbitrary Accuracy Derivative (ADER) finite volume methods for hyperbolic balance laws with stiff terms are extended to solve one-dimensional blood flows for viscoelastic vessels in [14], and such technique is applied to analyze the treatment of viscoelastic effects at junctions in [15]. The effects of variations of the mechanical properties of arteries due to diseases such as stenosis or aneurysms have also being studied using 1D models [16–18]. It has also been noted in [19] that 1D models are able to describe the fluid's evolution after arteriovenous fistula (AVF) surgeries in 6 out of 10 patients and selected the same AVF location as an experienced surgeon in 9 out of 10 patients. Although 1D models have shown to be a reasonably good approximation in many situations, there exist limitations due in part to simplifications such as axial symmetry. The cross section is assumed to be a circle, which impacts the results.

The contributions listed above consider the two extreme cases where the models are either 3D or 1D, and some interactions between them. In this thesis, we derive an intermediate two-dimensional (2D) model where any shape of the cross section can be considered while maintaining a still much lower computational cost compared to 3D simulations. The 2D models are a good balance that provides more realistic results compared to its 1D counterparts and it has the advantage of a low computational cost when compared to the 3D models. The derivation and implementation of a model in two dimensions is one

of our main contributions. The model is derived using asymptotic analysis that follows certain physical considerations. The velocity and vessel's radius here depend on the cross section's angle and axial position, while the 1D counterpart considers a uniform radius that varies only in the axial direction. Our model can handle perturbations and variations in the wall's elasticity affecting any specific area of the vessel while 1D simulations can only consider perturbations affecting entire cross sections. This is relevant in simulations of diseases such as aneurysms and stenosis that involve vessels with walls that have damaged areas, not necessarily entire cross sections. Furthermore, we present the properties of the model, construct a well-balanced central-upwind scheme and include numerical tests that show its merits.

Part II: Generalized Quasi-Geostrophy for Moist Spatially Anisotropic Atmospheric Flows with Phase Changes

Atmospheric science studies the Earth's atmosphere and its various inner-working physical processes. Atmospheric science has been extended to the field of planetary science and the study of the atmospheres of the planets and natural satellites of the Solar System. On the other hand, atmospheric dynamics studies the motion systems of meteorological importance. It does it by integrating observations at different locations and times and with the aid of complex theories. Common topics studied include a big variety of phenomena which includes thunderstorms, tornadoes, gravity waves, tropical cyclones, extratropical cyclones, jet streams, and global-scale circulations. The goal of dynamical studies is to explain the observed circulations on the basis of fundamental principles from physics, using mathematical modeling in some cases to understand it. The objectives of such studies incorporate improving weather forecasting, developing methods for predicting seasonal and interannual climate fluctuations, and understanding the implications of human-induced perturbations (e.g., increased carbon dioxide concentrations or depletion of the ozone layer) on the global climate [20].

Weather forecasting is the application of science and technology to predict the conditions of the atmosphere for a given location and time. People have attempted to predict the weather informally for millennia and formally since the 19th century. Weather forecasts are made by collecting quantitative data about the current state of the atmosphere, land, and ocean and using meteorology to project how the atmosphere will change at a given place.

Once calculated manually based mainly upon changes in barometric pressure, current weather conditions, and sky condition or cloud cover, weather forecasting now relies on computer-based models that take many atmospheric factors into account [21]. Human input is still required to pick the best possible forecast model to base the forecast upon, which involves pattern recognition skills, teleconnections, knowledge of model performance, and knowledge of model biases. The inaccuracy of forecasting is due to the chaotic nature of the atmosphere, the massive computational power required to solve the equations that describe the atmosphere, the land, and the ocean, the error involved in

measuring the initial conditions, and an incomplete understanding of atmospheric and related processes. Hence, forecasts become less accurate as the difference between current time and the time for which the forecast is being made (the range of the forecast) increases. The use of ensembles and model consensus help narrow the error and provide confidence level in the forecast.

It was not until the 20th century that advances in the understanding of atmospheric physics led to the foundation of modern numerical weather prediction. In 1922, English scientist Lewis Fry Richardson published "Weather Prediction By Numerical Process" [22] after finding notes and derivations he worked on as an ambulance driver in World War I. He described therein how small terms in the prognostic fluid dynamics equations governing atmospheric flow could be neglected, and a finite differencing scheme in time and space could be devised, to allow numerical prediction solutions to be found.

Despite the progress in predicting atmospheric flows, there are still many physical processes involved that are not understood. For instance, in one fluid's evolution there can be several waves interacting among them and influencing the formation of coherent structures and the corresponding trajectories. In that direction, the celebrated quasi-geostrophic equations have shown to be very useful. This system considers a balance between pressure gradients and Coriolis forces [23]. It has lead a decomposition of balanced (low frequency) and unbalanced (high frequency) components. Slow balanced components are associated, for instance, to the vortices observed in the ocean and in the atmosphere. They evolve on a slow timescale and persist over time (months) as a coherent structure. On the other hand, the fast unbalanced components are associated to intertia-gravity waves and move much faster. The study of such decomposition of the flow have received a lot of attention and a vast amount of literature exists out there regarding this phenomenon, including the spontaneous generation of inertia-gravity waves and the study of slow manifolds where flows evolve in time near balance. See [24] for a review. It has also been of interest the study of the effect of both slow and fast modes in the formation and evolution of coherent structure. In that direction, interactions between vortical and wave components in the Boussinesq and shallow water equations have been studied in [25–27].

The slow and fast modes have been mainly studied in the Boussinesq and rotating shallow water equations. In the case of the atmosphere, that corresponds to the dry case where no moist is considered at all. Very recently, a huge effort has been dedicated to developing the concept of low and high frequency components in the presence of moist. In [28],[29], the precipitating Quasi-geostrophic equations (PQG) are derived and implemented. In [29], the PQG model was analyzed in both scenarios: with saturated and unsaturated atmosphere. Although this work has been very successful, the implementation of the model is very challenging because the moist potential vorticity involves stiff terms and the PV-inversion is very complicated.

In [30], quasi-geostrophy was generalized for anisotropic rotating flows in the dry case. The model was derived using asymptotic analysis in terms of the Rossby number and assuming certain assumptions to be discussed in this thesis. In this work, we extend that approach by taking moist into consideration. Our contribution here is the derivation of a new model that encompasses a concept of balanced and unbalanced components in the moist case. We generalize quasi-geostrophy to the moist case in a different way compared to the one described above. Our limiting equations are in the opposite side since we assume a large vertical scale with non-vanishing leading vertical velocity. One advantage here is that no PV-inversion is required. The resulting model is multi-scale where the averaged moist and equivalent potential temperature evolve over a slow timescale and the fluctuations evolving on a fast timescale. The setting here allows us to analyze cyclogenesis and heat transport when vortical towers interact before forming a pre-hurricane.

Part I

A new two-dimensional blood flow model with arbitrary cross sections

Chapter 1

Introduction to Hyperbolic Conservation Laws

The impact of cardiovascular diseases in our lives has motivated the development of different models for blood flows. See for instance [2] and [3] for a review of recent contributions towards the modeling of vascular flows and the cardiovascular system. Also, in [4], a discussion about mathematical modeling and numerical simulation of the cardiovascular system is provided.

A variety of physical phenomena can be analyzed by PDE-based models. For instance, models associated to the evolution of flows in gas or geophysical fluid dynamics fall within the class of *Hyperbolic Balance Laws*. Such systems have specific theoretical challenges that have been analyzed and reported in an extensive literature. See [31] for an extensive discussion on the main aspect of such type of PDEs. On the other hand, there has been an increased interest in the community to construct stable and efficient numerical schemes. Among the desirable properties, the numerical scheme must have a high order of approximation in smooth regions while computing jump discontinuities properly near shock waves.

Blood flows can be considered a Newtonian fluid in the case of large arteries in the large circulation system. Models can be derived by taking the Navier-Stokes equations and apply an averaging process in each cross section at a given axial position. Surprisingly, the

resulting models usually form hyperbolic systems of conservation laws. See for instance, the models considered in [9, 13]. The advantage of interpreting the models with their hyperbolic properties is the knowledge available in the literature about such systems. A lot is known about the behavior of hyperbolic systems both theoretically in terms of existence of weak solutions as well as the construction of a variety of high resolution numerical schemes that are robust and efficient in approximating solutions to the aforementioned PDEs. In this chapter, we present a brief introduction to the topic of hyperbolic conservation laws. We will discuss the main theoretical and numerical challenges we may found when solving such systems, either when defining exact weak (discontinuous) solutions or when approximating them numerically. More details can be found in [31] and [32].

1.1 Classification of equations

This section is based on the material found in [32].

Physical problems can be classified in general as: equilibrium, eigenvalue and transport problems. Those physical problems can be described by the structure the equations may have and the qualitative behavior its solutions may describe. In particular, one can use the concept of *characteristics* to derive one such classification.

Although the following analysis can be carried out for a linear system of PDEs that depend on two independent variables, we focus here on the specific case of interest to us. Let us consider the following second-order quasi-linear equation given by

$$au_{xx} + bu_{xy} + cu_{yy} = f.$$

The above system is sufficiently general to represent a variety of scientific problems in physics and engineering, where the mathematical models are second-order.

Suppose the solution is known from the initial state at some curve Γ (and below it). For some P on the boundary $\partial\Gamma$, we know the derivatives of u and its directional derivatives in the direction of this curve. We require that knowing u, u_x and u_y at Γ are sufficient to determine the unique value of u_{xx}, u_{xy} and u_{yy}. If the directional derivatives of u_x and

u_y are known, we have

$$\begin{aligned} du_x &= u_{xx}dx + u_{xy}dy, \\ du_y &= u_{xy}dx + u_{yy}dy. \end{aligned}$$

Then, we get

$$\begin{pmatrix} a & b & c \\ dx & dy & 0 \\ 0 & dx & dy \end{pmatrix} \begin{pmatrix} u_{xx} \\ u_{xy} \\ u_{yy} \end{pmatrix} = \begin{pmatrix} f \\ du_x \\ du_y \end{pmatrix}.$$

A unique solution for u_{xx}, u_{xy} and u_{yy} exists and is unique unless the determinant of the 3×3 - matrix is zero. That is,

$$a\left(\frac{dy}{dx}\right)^2 - b\frac{dy}{dx} + c = 0. \tag{1.1}$$

In the case the determinant is zero, multiple solutions may exist. As a result, the partial derivatives are not unique and thus, discontinuities in the partial derivatives are expected at Γ.

The curves given by the solutions to equation (1.1) are known as *characteristics*. The direction of the characteristic curves are related to the solutions of the equation $ax^2 - bx + c = 0$, and them can be real and different, coincide or be complex, depending on wheter the value of the discriminant $b^2 - 4ac$ is positive, zero or negative, respectively. We then say that the equation

$$au_{xx} + bu_{xy} + cu_{yy} = f$$

is:

- **hyperbolic** if $b^2 - 4ac > 0$.
- **parabollic** if $b^2 - 4ac = 0$.
- **elliptic** if $b^2 - 4ac < 0$.

Specifically, in the case hyperbolic case, real-valued characteristic curves in phase space and discontinuities might propagate through those curves.

1.2 The wave equation

Let consider the wave equation

$$u_{xx} - a^2 u_{yy} = 0,$$

where a is constant. Then, the characteristic curves $y(x)$ satisfy

$$\left(\frac{dy}{dx}\right)^2 - a^2 = 0,$$

with closed-expression given by

$$y = \beta \pm ax,$$

for a constant β.

As we can see, the wave equation is hyperbolic. For the rest of this chapter, we will focus on hyperbolic problems and extend the concept to non-linear systems.

The conservation laws to be analyzed later in this chapter fall in the class of hyperbolic PDEs. This kind of equations arise in transport problems such as gas dynamics and wave mechanics among many other areas. In order to explain the main properties of such equations, let us consider the wave equation:

$$u_{tt} - a^2 u_{xx} = 0.$$

with initial conditions

$$\begin{aligned} u(x,0) &= F(x), \\ u_t(x,0) &= G(x), \end{aligned}$$

The solution of this equation can be directly calculated by the D'Alambert method. Skipping the details, the solution is computed as

$$u(x,t) = \frac{F(x+at) + F(x-at)}{2a} + \frac{1}{2a}\int_{x-at}^{x+at} G(\eta)\, d\eta$$

We note that the solution is decomposed into the sum of two solutions to the transport equation propagating at speeds $\pm a$. Below, we will take the transport equation as a base to extend the notion of hyperbolic balance laws in the non linear limit.

1.3 Hyperbolic conservation laws

The rest of the chapter will be focused in hyperbolic conservation laws. This type of equations arise in transport problems in areas such as wave mechanics, gas and fluid dynamics among many others. Our purpose here is to present the basic aspects of hyperbolic conservation laws. The information presented in this chapter is not comprehensive and it is not intended to present all the interesting details behind. The interested reader may find a detailed analysis in [31, 33, 34, 34–37] and references therein. We explain the main aspects of the above equations and the corresponding solutions by considering first scalar conservation laws but we will later on extend such concepts to systems.

1.3.1 The scalar conservation law

A scalar conservation law in one spatial-dimension is a first-order partial differential equation (PDE) of the form

$$u_t + \left(f(u)\right)_x = 0.$$

When solved in the entire real line, the associated initial value problem is written as

$$\begin{cases} u_t + \left(f(u)\right)_x = 0, & -\infty < x < \infty, \\ u\left(x, t=0\right) = u_o\left(x\right). \end{cases}$$

If the problem is solved in a bounded domain, associated boundary conditions (Neumann, Dirichlet, etc) must be included in order to properly solve the initial boundary value problem (IBVP).

Equations of this type often describe transport phenomena. Here, $u(x,t)$ is known as the conserved quantity (as density, linear momentum, mass, etc) and $f(u)$ is known as the flux function. As one will see later, the flux must be a convex function of the conserved quantity u. This is motivated by the fact that after integrating over the interval $[x_o, x_1]$, we get

$$0 = \int_{x_o}^{x_1} u_t dx + f(u(x_1,t)) - f(u(x_o,t)) = \partial_t \left(\int_{x_o}^{x_1} u dx \right) + f(u(x_1,t)) - f(u(x_o,t)), \quad (1.2)$$

which implies

$$\partial_t \left(\int_{x_o}^{x_1} u dx \right) = f(u(x_o,t)) - f(u(x_1,t)).$$

It means that the ratio of change of the total amount u contained inside any given interval $[x_o, x_1]$ is given by the flux at the boundary points. For instance, when the flux vanishes or balances at the boundary, the total amount remains constant.

1.3.2 Weak solutions

Conservation laws are distinguished by the propagation of information across characteristic curves. It is well-known that solutions to hyperbolic problems may develop shock waves in finite time even if the initial conditions are smooth. Weak solutions are to be defined in such cases. For that end, one needs to find the integral formulation of the conservation law as follows. We will not repeat the information that can be found in many textbooks. Instead, we summarize the basic aspects of the hyperbolic conservation laws in the next few sections.

Consider the scalar conservation law

$$u_t + (f(u))_x = 0.$$

A simple integration over an arbitrary rectangle $[x_o, x_1] \times [t_o, t_1]$ gives us the integral form of the conservation law:

$$\begin{aligned} 0 &= \int_{x_o}^{x_1} \int_{t_o}^{t_1} [u_t + (f(u))_x] dt dx \\ &= \int_{x_o}^{x_1} [u(x, t_1) - u(x, t_o)] dx + \int_{t_o}^{t_1} [f(u(x_1, t)) - f(u(x_o, t))] dt. \end{aligned}$$

An integrable function u is considered a weak solution provided it satisfies the above equation for all x_0, x_1, t_o, t_1 in the domain. We now present an alternative condition to determine weak solutions.

Let us assume that a solution exists with a discontinuity along a given curve $(x_{\text{shock}}(t), t)$ in phase space. So, the solution which is piece-wise smooth may be split into two smooth solutions $u_\ell(x, t)$ and $u_r(x, t)$ which are defined and smooth on the left and right sides of the shockwave respectively. Integrating over a rectangle close to the shockwave curve and using the integral form of the conservation law, one arrives at the so-called *Rankine-Hugoniot* jump conditions

$$\Delta f = s \Delta u,$$

where $\Delta u = u_r(x_{\text{shock}}(t), t) - u_\ell(x_{\text{shock}}(t), t)$, $\Delta f = f(u_r(x_{\text{shock}}(t), t)) - f(u_\ell(x_{\text{shock}}(t), t))$ are the jumps in the solution and the flux across the shockwave, and

$$s = \frac{dx_{\text{schok}}}{dt}$$

is the shockwave's speed of propagation.

It is well-known that a weak solution is said to satisfy the entropy condition if

$$f'(u_\ell) \geq s \geq f'(u_r)$$

Weak solutions satisfying the Rankine-Hugoniot jump conditions are not unique. However, the entropy condition is helpful in finding the physically relevant weak solutions. The next section explains the Riemann problem and its relation to the entropy condition must become clear.

1.3.3 The Riemann problem

The Riemann problem is often taken into consideration when developing numerical schemes because exact solutions for the non-linear problem can be found in this case. We include it in this chapter because it is also useful in understanding the entropy conditions discussed in the previous section.

The Riemann problem is an initial-valued problem where the PDE is a conservation law and the initial condition consists of a piecewise constant initial data which has a jump in the domain of interest. It may be written as

$$\begin{cases} u_t + (f(u))_x = 0 \\ u(x,0) = \begin{cases} u_\ell & \text{if} \quad x \leq 0 \\ u_r & \text{if} \quad 0 < x \end{cases} \end{cases}$$

The jump condition in the scalar case is simply $s = \dfrac{f(u_r) - f(u_\ell)}{u_r - u_\ell}$. Although this shows that a Riemann problem has at least one weak solution given by a shockwave, not all of them are physically relevant and we must discard them. For that end, notice that the characteristic curves are straight lines given by

$$x(t) = \begin{cases} x_o + f'(u_\ell)t & \text{if} \quad x_o \leq 0, \\ x_o + f'(u_r)t & \text{if} \quad 0 < x_o, \end{cases}$$

with $f'(u) = \dfrac{df}{du}(u)$.

Let us first suppose that $f'(u_\ell) > f'(u_r)$. In this case, the characteristic curves merge into the shockwave. We obtain a jump discontinuity. Furthermore, we notice that in this case the entropy condition is automatically satisfied

$$f'(u_\ell) \geq \frac{f(u_r) - f(u_\ell)}{u_r - u_\ell} \geq f'(u_r)$$

provided that $f(u)$ is a convex function of u.

The shockwave solution is simply

$$u(x,t) = \begin{cases} u_\ell & \text{if} \quad x \leq st \\ u_r & \text{if} \quad st < x \end{cases}$$

Let us now assume the opposite case where $f'(u_r) > f'(u_\ell)$. One can easily show by smoothing out the initial condition (so perturbing it) that a small change on it will create a very different solution where the characteristics expand in a rarefaction fan. This means that the shockwave proposed in the previous case is unstable to small perturbations in the initial condition. As a result, we consider it not to be a physically relevant weak solution. In addition to it, it does not satisfy the entropy condition. The discontinuous solution in this case would have characteristic curves emanating from the shockwave instead of being originated from the initial condition at $t = 0$. The physically relevant solution in this case is a **rarefaction wave**. It has a smooth transition from the left to the right state, and it is given by

$$u(x,t) = \begin{cases} u_\ell & \text{if} \quad \dfrac{x}{t} < f'(u_\ell) \\ v\left(\dfrac{x}{t}\right) & \text{if} \quad f'(u_\ell) \leq \dfrac{x}{t} \leq f'(u_r) \\ u_r & \text{if} \quad f'(u_r) < \dfrac{x}{t} \end{cases}$$

where $v(\eta)$ is the solution of $f'(v(\eta)) = \eta$. The above solution requires $f'(u)$ to be an invertible function of u. One then needs the flux to be a convex function of u, which is gain needed to fulfill the entropy conditions.

1.3.4 System of conservation laws

Let $\mathbf{U}(\mathbf{x},t) : \mathbb{R}^n \times \mathbb{R} \to \mathbb{R}^m$ be a m-dimensional vector and $\mathbf{F}_i(\mathbf{U}) : \mathbb{R}^m \to \mathbb{R}^m$, $i = 1, 2, \ldots, n$ a vector-valued function that satisfies

$$\frac{\partial \mathbf{U}}{\partial t} + \sum_{i=1}^{n} \frac{\partial \mathbf{F}_i(\mathbf{U})}{\partial x_i} = \mathbf{S}(\mathbf{U}). \tag{1.3}$$

for a specific source term vector $\mathbf{S}(\mathbf{U})$. In many applications all the independent variables x_i have the same units (length in shallow water flows for instance). We include applications where one direction refers to length (axial) while a second variable describes the angular direction (radians). One then needs to non-dimensionalize the system in order to define its hyperbolic properties. For that end, let α_i be the characteristic scale of U_i, T be the timescale, and L_i the characteristic scale in the x_i-direction. Then, system (1.3) may be rewritten as

$$\frac{\partial \tilde{\mathbf{U}}}{\partial \tilde{t}} + \sum_{i=1}^{n} \frac{\partial \tilde{\mathbf{F}}_i\left(\tilde{\mathbf{U}}\right)}{\partial \tilde{x}_i} = \tilde{\mathbf{S}}\left(\tilde{\mathbf{U}}\right). \tag{1.4}$$

where $\widetilde{(\cdot)}$ denotes the non-dimensional quantities and satisfy, $\tilde{x}_i = x_i/L_i$,

$$\widetilde{\mathbf{U}} = \begin{pmatrix} U_1/\alpha_1 \\ U_2/\alpha_2 \\ \vdots \\ U_m/\alpha_m \end{pmatrix}, \quad \widetilde{\mathbf{F}}_i = \begin{pmatrix} (\mathbf{F}_i)_1/(\alpha_1 L_i/T) \\ (\mathbf{F}_i)_2/(\alpha_2 L_i/T) \\ \vdots \\ (\mathbf{F}_i)_m/(\alpha_m L_i/T) \end{pmatrix}$$

We now define the non-dimensional Jacobian simply by $J_{\widetilde{\mathbf{U}}}(\widetilde{\mathbf{F}}_i) = \partial \widetilde{\mathbf{F}}_i/\partial \widetilde{\mathbf{U}}$. The PDE (1.3) is said to be a hyperbolic system of conservation laws provided that for any unitary vector $(\eta - 1, \ldots, \eta_m)$, the linear combination of the dimensionless Jacobians $J_{\widetilde{\mathbf{U}}}(\widetilde{\mathbf{F}}_i)$

$$\eta_1 J\left(\tilde{\mathbf{F}}_1\right) + \eta_2 J\left(\tilde{\mathbf{F}}_2\right) + \cdots + \eta_n J\left(\tilde{\mathbf{F}}_n\right)$$

has real eigenvalues and a complete set of m linear independent eigenvectors.

Changing the characteristic scales would result in a rescaling of the η coefficients. Therefore, the above definition of hyperbolicity is independent of the non-dimensionalization. The vector-valued functions $\mathbf{F}_i$ with j-th component $(\mathbf{F}_i)_j$ are called the flux function in the x_i-direction for the conserved quantity U_j.

Some examples of physical phenomena that can be modeled by hyperbolic conservation laws are the Euler equations, the shallow water equations over an arbitrary topography and the (1D) axisymmetric blood flow model [9].

1.4 Finite volume methods for hyperbolic conservation laws.

In one space dimension, a finite volume method is based on subdividing the spatial domain into intervals, so-called *finite volumes* or *grid cells*, and keeping track of an approximation to the integral of the conserved quantity u in each cell. In each time step, we update these values using approximations to the flux through the cells' interfaces.

Denote the j-th grid cell by $I_j = \left[x_{j-\frac{1}{2}}, x_{j+\frac{1}{2}}\right]$ as shown. Let us denote by $U_j^{(n)}$ the approximation to the average value over the j-th cell at time $t^{(n)}$:

$$U_j^{(n)} \approx \frac{1}{\Delta x_j} \int_{I_j} u\left(x, t^{(n)}\right) dx,$$

where $\Delta x_j = x_{j+\frac{1}{2}} - x_{j-\frac{1}{2}}$ is the length of the cell. For simplicity, we assume an uniform grid, that is, $x_j = (j-1)\,\Delta x$ for a fixed Δx.

When deriving a numerical scheme, we would like to achieve desirable properties that can make the numerical approximation robust and accurate. In particular, **conservation** at a discrete level is crucial when calculating flows near shockwaves. The Riemann sum

$$\sum_{j=1}^{N} U_j^{(n)} \Delta x$$

approximates the integral of u over the entire interval $[a, b]$. Conservative numerical schemes can preserve that quantity constant over time at a discrete level in the absence of source terms.

At a continuous level, conservation reads

$$\frac{d}{dt} \int_{I_j} u\,(x,t)\,dx = f\left(u\left(x_{j+\frac{1}{2}}, t\right)\right) - f\left(u\left(x_{j-\frac{1}{2}}, t\right)\right).$$

By the second fundamental theorem of calculus, the integration of the above expression over the time-step $\left[t^{(n)}, t^{(n+1)}\right]$ yields

$$\int_{I_j} u\left(x, t^{(n+1)}\right) dx - \int_{I_j} u\left(x, t^{(n)}\right) dx = \int_{t^{(n)}}^{t^{(n+1)}} f\left(u\left(x_{j+\frac{1}{2}}, t\right)\right) dt - \int_{t^{(n)}}^{t^{(n+1)}} f\left(u\left(x_{j-\frac{1}{2}}, t\right)\right) dt.$$

Rearranging the last expression and dividing by Δx gives

$$\begin{aligned} \frac{1}{\Delta x}\int_{I_j} u\left(x, t^{(n+1)}\right) dx &= \frac{1}{\Delta x}\int_{I_j} u\left(x, t^{(n)}\right) dx \\ &\quad - \frac{1}{\Delta x}\left[\int_{t^{(n)}}^{t^{(n+1)}} f\left(u\left(x_{j+\frac{1}{2}}, t\right)\right) dt - \int_{t^{(n)}}^{t^{(n+1)}} f\left(u\left(x_{j-\frac{1}{2}}, t\right)\right) dt\right]. \end{aligned}$$

This explains to us how exactly the cell average of u should be updated in one time step. However, we cannot evaluate the time integrals on the right-hand side of the equation exactly. This suggests the use of numerical methods of the form

$$U_j^{(n+1)} = U_j^{(n)} - \frac{\Delta t}{\Delta x}\left[F_{j+\frac{1}{2}}^{(n)} - F_{j-\frac{1}{2}}^{(n)}\right]$$

where $F_{j-\frac{1}{2}}^{(n)}$ is an appropriate approximation of the average flux across the interface $x = x_{j-\frac{1}{2}}$,

$$F_{j-\frac{1}{2}}^{(n)} \approx \frac{1}{\Delta t}\int_{t^{(n)}}^{t^{(n+1)}} f\left(u\left(x_{j-\frac{1}{2}}, t\right)\right) dt.$$

It sounds reasonable to suppose the value of $F_{j-\frac{1}{2}}^{(n)}$ only depends of the cell averages $U_{j-1}^{(n)}$ and $U_j^{(n)}$ of this interfaces, because the information propagates at finite time in hyperbolic problems. We might need to extrapolate that information to approximate the data at the interface. So, we may use a formula of the form

$$F_{j-\frac{1}{2}}^{(n)} = \mathcal{F}\left(U_{j-1}^{(n)}, U_j^{(n)}\right) \tag{1.5}$$

where $\mathcal{F}$ is so-called the **numerical flux function**. Now, we have

$$U_j^{(n+1)} = U_j^{(n)} - \frac{\Delta t}{\Delta x}\left[\mathcal{F}\left(U_j^{(n)}, U_{j+1}^{(n)}\right) - \mathcal{F}\left(U_{j-1}^{(n)}, U_j^{(n)}\right)\right]$$

Although this specific type of numerical method depends of the particular choice of $\mathcal{F}$, the above method is well-known as a **explicit three-point stencil method**. Some of this particular choices are:

- One-sided left scheme:

$$\mathcal{F}\left(U_{j-1}^{(n)}, U_j^{(n)}\right) = f\left(U_{j-1}^{(n)}\right),$$

$$U_j^{(n+1)} = U_j^{(n)} - \frac{\Delta t}{\Delta x}\left[f\left(U_j^{(n)}\right) - f\left(U_{j-1}^{(n)}\right)\right].$$

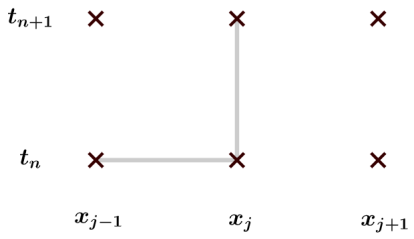

FIGURE 1.1: One-sided left scheme.

- One-sided right scheme:

$$\mathcal{F}\left(U_{j-1}^{(n)}, U_j^{(n)}\right) = f\left(U_j^{(n)}\right),$$

$$U_j^{(n+1)} = U_j^{(n)} - \frac{\Delta t}{\Delta x}\left[f\left(U_{j+1}^{(n)}\right) - f\left(U_j^{(n)}\right)\right].$$

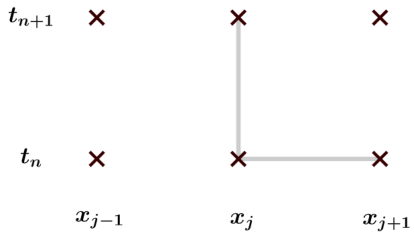

FIGURE 1.2: One-sided right scheme.

- Forward Euler scheme:

$$\mathcal{F}\left(U_{j-1}^{(n)}, U_j^{(n)}\right) = \frac{f\left(U_{j-1}^{(n)}\right) + f\left(U_j^{(n)}\right)}{2},$$

$$U_j^{(n+1)} = U_j^{(n)} - \frac{\Delta t}{2\Delta x}\left[f\left(U_{j+1}^{(n)}\right) - f\left(U_{j-1}^{(n)}\right)\right].$$

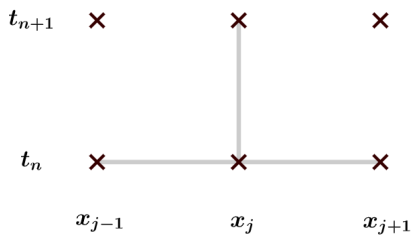

FIGURE 1.3: Forward Euler scheme.

- Lax-Friedrich scheme:

$$\mathcal{F}\left(U_{j-1}^{(n)}, U_j^{(n)}\right) = \frac{f\left(U_{j-1}^{(n)}\right) + f\left(U_j^{(n)}\right) - \frac{\Delta x}{\Delta t}\left[U_j^{(n)} - U_{j-1}^{(n)}\right]}{2},$$

$$U_j^{(n+1)} = \frac{U_{j-1}^{(n)} + U_{j+1}^{(n)}}{2} - \frac{\Delta t}{2\Delta x}\left[f\left(U_{j+1}^{(n)}\right) - f\left(U_{j-1}^{(n)}\right)\right].$$

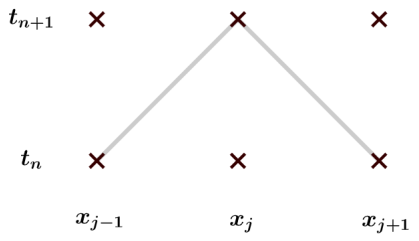

FIGURE 1.4: Lax-Friedrich scheme

1.4.1 The Central-Upwind method

The central-upwind method is based on the idea of taking the difference between each cell-volume average. The procedure of this method is done by a reconstruction of the cell-volume average at the interfaces of the grid cells C_j.

The solution U is approximated by a piecewise polynomial reconstruction $p_j(x)$. This reconstruction must be **conservative**, **second-order accurate** and **non-oscillatory**,

$$\tilde{U}(x,t) = \sum_{C_j} p_j(x,t)\,\mathbb{I}_{C_j}(x), \text{ where } \mathbb{I}_{C_j}(x) = \begin{cases} 1 & x_j \le x < x_{j+1}, \\ 0 & \text{otherwise.} \end{cases}$$

The second-order accurate needs a piecewise linear reconstruction, as

$$\tilde{U}(x,t) = U_j^{(n)} + (U_x)_j (x - x_j)$$

where x_j is the center of each grid-cell. The non-oscillatory property must be obtained via a nonlinear limiter, for example, the minmod limiter

$$(U_x)_j = \text{minmod}\left(\theta\frac{U_j^{(n)} - U_{j-1}^{(n)}}{\Delta x}, \frac{U_{j+1}^{(n)} - U_{j-1}^{(n)}}{2\Delta x}, \theta\frac{U_{j+1}^{(n)} - U_j^{(n)}}{\Delta x}\right), \quad \theta \in [1,2]$$

where

$$\text{minmod}(a,b,c) = \begin{cases} \min_j\{z_j\} & \text{if} \quad z_j > 0 \ \forall j, \\ \max_j\{z_j\} & \text{if} \quad z_j < 0 \ \forall j, \\ 0 & \text{otherwise.} \end{cases}$$

After this step, we reconstruct U at the interface $x = x_{j+\frac{1}{2}}$ as

$$\begin{aligned} U_{j+\frac{1}{2}}^{-} &= U_j^{(n)} + \frac{\Delta x}{2}(U_x)_j, \\ U_{j+\frac{1}{2}}^{+} &= U_{j+1}^{(n)} - \frac{\Delta x}{2}(U_x)_{j+1}. \end{aligned}$$

The discontinuities that appears at the reconstruction step in the interfaces propagates at finite speed, estimated by

$$\begin{aligned} a_{j+\frac{1}{2}}^{+} &= \max\left\{f'\left(U_{j+\frac{1}{2}}^{-}\right), f'\left(U_{j+\frac{1}{2}}^{+}\right), 0\right\}, \\ a_{j+\frac{1}{2}}^{-} &= \min\left\{f'\left(U_{j+\frac{1}{2}}^{-}\right), f'\left(U_{j+\frac{1}{2}}^{+}\right), 0\right\}. \end{aligned}$$

In the case of higher dimensions, with $\mathbf{U}$ a vector of N dimensions and $\mathbf{F}$ also a vector of N dimensions,

$$\begin{aligned} a^+_{j+\frac{1}{2}} &= \min\left\{\lambda_N\left(J_{\widehat{\mathbf{U}}}\left(\mathbf{F}\right)\left(U^-_{j+\frac{1}{2}}\right)\right), \lambda_N\left(J_{\widehat{\mathbf{U}}}\left(\mathbf{F}\right)\left(U^+_{j+\frac{1}{2}}\right)\right), 0\right\}, \\ a^-_{j+\frac{1}{2}} &= \min\left\{\lambda_1\left(J_{\widehat{\mathbf{U}}}\left(\mathbf{F}\right)\left(U^-_{j+\frac{1}{2}}\right)\right), \lambda_1\left(J_{\widehat{\mathbf{U}}}\left(\mathbf{F}\right)\left(U^+_{j+\frac{1}{2}}\right)\right), 0\right\}, \end{aligned}$$

where $\lambda_1 < \lambda_2 < \cdots < \lambda_N$ are the eigenvalues of the Jacobian $J\left(\mathbf{F}\right)$ at U. Then, the numerical flux is calculated by

$$\mathcal{F}\left(U^{(n)}_{j-1}, U^{(n)}_j\right) = \frac{a^+_{j+\frac{1}{2}} f\left(U^-_{j+\frac{1}{2}}\right) - a^-_{j+\frac{1}{2}} f\left(U^+_{j+\frac{1}{2}}\right)}{a^+_{j+\frac{1}{2}} - a^-_{j+\frac{1}{2}}} + \frac{a^+_{j+\frac{1}{2}} a^-_{j+\frac{1}{2}}}{a^+_{j+\frac{1}{2}} - a^-_{j+\frac{1}{2}}}\left[U^+_{j+\frac{1}{2}} - U^-_{j+\frac{1}{2}}\right]$$

Chapter 2

Derivation of the blood flow model

2.1 The geometry of the vessel

We consider the dynamics of a blood flow passing through an artery, which is mathematically interpreted as a cylindrical-shape domain with a flow moving mainly in its axial direction. Considering the 3D flow given by the Navier-Stokes equations can give important details of the flow but it can be computationally very expensive. As an alternative, reduced models can provide enough details to analyze specific features in the vessel, such as pressure waves. Following that idea, 1D models have been derived in the past few years by taking the Navier-Stokes equations in cylindrical coordinates and averaging over each cross section. Such models need to assume axi-symmetry, which is an important restriction. In this thesis, we consider a 2D model that falls between the two extremes. That is, we only take a radial average in each cross section, allowing for variations in the angular direction. As a result, we obtain a model that has a better balance between computational cost and complexity.

Although it can be easily generalized, let us assume for simplicity that the vessel is aligned in the $x - z$ plane and that it extends along a curve that passes through each cross section. The parametrization of such curve is assumed to be known and its location is then represented by its arclength's position s and coordinates $(x_o(s), y_o = 0, z_o(s))$. Each cross section is identified with the arclength position s of the curve intersecting

it. Any position in each cross section is located with the angle θ formed between the displacement from the intersection and a reference vector. The variables and parameters are functions of the axial position s and angle θ. As a result, the model allows for arbitrary cross sections and variations in each angle θ, resulting in a 2D model.

The above parametrization is done such that $s = 0$ corresponds to the left end of the vessel, while $s = s_L$ is related to the right end. For each s, the cross-section denoted by $C(s)$ is contained in a plane passing through $(x_o(s), y_o = 0, z_o(s))$ and perpendicular to the unit tangent vector $\mathbf{T}(s) = (\cos(\alpha(s)), 0, \sin(\alpha(s)))$. Here $\alpha(s)$ is the angle of the curve with respect to the horizontal axis x. Furthermore, for a point (x, y, z) in the cross-section $C(s)$, let θ be the angle between the normal vector $(-\sin(\alpha(s)), 0, \cos(\alpha(s)))$ and the displacement $(x, y, z) - (x_o(s), 0, z_o(s))$. This gives the following change of variables:

$$\begin{aligned} x(r, s, \theta) &= x_o(s) - r\sin(\alpha(s))\sin(\theta), \\ y(r, s, \theta) &= r\cos(\theta), \\ z(r, s, \theta) &= z_o(s) + r\cos(\alpha(s))\sin(\theta), \end{aligned} \tag{2.1}$$

where r is the norm of the displacement. A sufficient condition for the change of variables to be valid is that the radius r for any point in the cross section does not exceed the radius of curvature of the parametrization. That is,

$$r \leq \mathfrak{R}(s) = \frac{1}{\kappa(s)},$$

where $\kappa(s) = |\alpha'(s)|$ is the vessel's curvature and $\mathfrak{R}$ is the radius of curvature.

Figure 2.1 shows the schematic of the model to be derived below. The vessel's radius may vary as a function of angle, axial position and time, $R = R(\theta, s, t)$. As a result, the vessel may have any cross-sectional shape. On the contrary, one-dimensional models assume a uniform radius, independent of θ, restricting the cross section to be axi-symmetric. The derivation of the model requires rewriting the Navier-Stokes equations [38] combined with

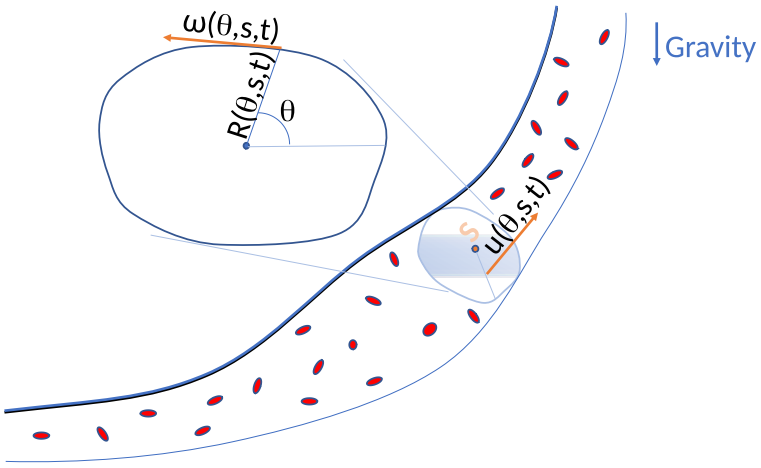

FIGURE 2.1: Schematic of model for blood flows passing through a compliant vessel. Here, R, u and ω are the vessel's cross-sectional radius, the radially-averaged axial velocity and the radially-averaged angular velocity, respectively. See section 2.2.

the incompressibility condition given by

$$\begin{aligned}
\tfrac{D}{Dt}\,\rho &= 0,\\
\tfrac{D}{Dt}\,(\rho V_x) &= -\partial_x\, P + \nu\Delta\, V_x,\\
\tfrac{D}{Dt}\,(\rho V_y) &= -\partial_y\, P + \nu\Delta\, V_y,\\
\tfrac{D}{Dt}\,(\rho V_z) &= -\partial_z\, P + \nu\Delta\, V_z - \rho g,\\
\nabla\cdot\mathbf{V} &= 0.
\end{aligned} \tag{2.2}$$

in cylindrical coordinates (2.1) (subsection 2.1.1) and carry out an asymptotic analysis to determine the leading order contribution under the following assumptions (subsection 2.1.2).

2.1.1 The equations in cylindrical coordinates

The derivation of the model requires the description of equations (2.2) in the coordinate system (s, r, θ). These equations, in compact form with $\mathbf{e}_3 = (0, 0, 1)^T$, are

$$\begin{aligned}
\frac{D}{Dt}\,(\rho) &= 0,\\
\frac{D}{Dt}\,(\rho\mathbf{V}) &= -\nabla\,(P) + \nu\Delta\,(\mathbf{V}) - \rho g\mathbf{e}_3\\
\nabla\cdot\mathbf{V} &= 0.
\end{aligned}$$

We describe here the material derivative $\frac{D}{Dt}$, the gradient ∇ and the Laplacian Δ in the variables (s, r, θ)-coordinate system. Let us note that the gradient in cartesian coordinates $\nabla = (\partial_x, \partial_y, \partial_z)$ and the gradient in (s, r, θ)-coordinates $\nabla_c = (\partial_s, \partial_r, \partial_\theta)$ are related by

$$\begin{aligned}
\partial_s &= \frac{|J|}{r}\Big\{ \cos(\alpha(s))\,\partial_x + \sin(\alpha(s))\,\partial_z \Big\} \\
\partial_r &= -\sin(\alpha(s))\sin(\theta)\,\partial_x + \cos(\theta)\,\partial_y + \cos(\alpha(s))\sin(\theta)\,\partial_z \\
\partial_\theta &= r\Big\{ -\sin(\alpha(s))\cos(\theta)\,\partial_x - \sin(\theta)\,\partial_y + \cos(\alpha(s))\cos(\theta)\,\partial_z \Big\}.
\end{aligned} \tag{2.3}$$

Also, the velocity field in cartesian coordinates $\mathbf{V} = (V_x, V_y, V_z)$ and the velocity field in the (s, r, θ)-coordinates $\mathbf{V}_c = (V_s, V_r, V_\theta)$ are related by

$$\begin{aligned}
V_s &= \frac{r}{|J|}\Big\{ \cos(\alpha(s))\,V_x + \sin(\alpha(s))\,V_z \Big\}, \\
V_r &= -\sin(\alpha(s))\sin(\theta)\,V_x + \cos(\theta)\,V_y + \cos(\alpha(s))\sin(\theta)\,V_z, \\
V_\theta &= \frac{1}{r}\Big\{ -\sin(\alpha(s))\cos(\theta)\,V_x - \sin(\theta)\,V_y + \cos(\alpha(s))\cos(\theta)\,V_z \Big\}.
\end{aligned} \tag{2.4}$$

Equations (2.3) and (2.4) can be reformulated by

$$\mathbf{V}_c = J^{-1}\mathbf{V}, \quad \nabla_c = J^T\nabla,$$

where

$$J = \begin{pmatrix}
(1 - r\sin(\theta)\,\alpha'(s))\cos(\alpha(s)) & -\sin(\theta)\sin(\alpha(s)) & -r\cos(\theta)\sin(\alpha(s)) \\
0 & \cos(\theta) & -r\sin(\theta) \\
(1 - r\sin(\theta)\,\alpha'(s))\sin(\alpha(s)) & \sin(\theta)\cos(\alpha(s)) & r\cos(\theta)\cos(\alpha(s))
\end{pmatrix} \tag{2.5}$$

is the jacobian of the change of variable (2.1). The corresponding determinant of the Jacobian is given by

$$|J| = r\,(1 - r\sin(\theta)\,\alpha'(s)).$$

The jacobian can be rewrite as

$$J = \begin{pmatrix} \frac{|J|}{r}\mathbf{J}_s & \mathbf{J}_r & r\mathbf{J}_\theta \end{pmatrix}$$

with

$$\mathbf{J}_s = \begin{pmatrix} \cos(\alpha(s)) \\ 0 \\ \sin(\alpha(s)) \end{pmatrix}, \quad \mathbf{J}_r = \begin{pmatrix} -\sin(\theta)\sin(\alpha(s)) \\ \cos(\theta) \\ \sin(\theta)\cos(\alpha(s)) \end{pmatrix}, \quad \text{and}$$

$$\mathbf{J}_\theta = \begin{pmatrix} -\cos(\theta)\sin(\alpha(s)) \\ -\sin(\theta) \\ \cos(\theta)\cos(\alpha(s)) \end{pmatrix}. \tag{2.6}$$

The above vectors are orthonormal, and also satisfies

$$\left(\mathbf{J}_s^{\perp}\right)^T \cdot \mathbf{J}_r = \sin(\theta), \quad \left(\mathbf{J}_s^{\perp}\right)^T \cdot \mathbf{J}_\theta = \cos(\theta)$$

Moreover, the expresion for J^{-1} is

$$J^{-1} = \left(J^T J\right)^{-1} J^T = \begin{pmatrix} \frac{r}{|J|}\mathbf{J}_s^T \\ \mathbf{J}_r^T \\ \frac{1}{r}\mathbf{J}_\theta^T \end{pmatrix},$$

$$J^T J = \begin{pmatrix} \left(\frac{|J|}{r}\right)^2 & 0 & 0 \\ 0 & 1 & 0 \\ 0 & 0 & r^2 \end{pmatrix}, \quad \left(J^T J\right)^{-1} = \begin{pmatrix} \left(\frac{r}{|J|}\right)^2 & 0 & 0 \\ 0 & 1 & 0 \\ 0 & 0 & \frac{1}{r^2} \end{pmatrix}.$$

The divergence operator, in the (s, r, θ)-coordinates is

$$\nabla \cdot (F_1, F_2, F_3) = \frac{1}{|J|}\nabla_c \cdot \left[|J| J^{-1}(F_1, F_2, F_3)\right]. \tag{2.7}$$

In the case of $(F_1, F_2, F_3) = \mathbf{V}$, we get that

$$\nabla \cdot \mathbf{V} = \frac{1}{|J|} \nabla_c \cdot (|J| \mathbf{V}_c) \,,$$

and for any function f,

$$\nabla \cdot (f\mathbf{V}) = \frac{1}{|J|} \nabla_c \cdot (|J| f \mathbf{V}_c) \,.$$

The above expression helps us to rewrite the material derivative in the (s, r, θ)-coordinates as

$$\begin{aligned} \frac{Df}{Dt} &= \partial_t (f) + \mathbf{V} \cdot \nabla (f) \\ &= \partial_t (f) + \nabla \cdot (f\mathbf{V}) - f \nabla \cdot \mathbf{V} \\ &= \partial_t (f) + \frac{1}{|J|} \nabla_c \cdot (|J| f \mathbf{V}_c) - \frac{f}{|J|} \nabla_c \cdot (|J| \mathbf{V}_c) \\ &= \frac{1}{|J|} \Big\{ \partial_t (|J| f) + \nabla_c \cdot (|J| f \mathbf{V}_c) - f \nabla_c \cdot (|J| \mathbf{V}_c) \Big\}. \end{aligned} \tag{2.8}$$

In the case of incompressible fluids, the last term vanishes and we obtain

$$\begin{aligned} \frac{Df}{Dt} &= \frac{1}{|J|} \Big\{ \partial_t (|J| f) + \nabla_c \cdot (|J| f \mathbf{V}_c) \Big\} \\ &= \frac{1}{|J|} \Big\{ \partial_t (|J| f) + \partial_s (|J| f V_s) + \partial_r (|J| f V_r) + \partial_\theta (|J| f V_\theta) \Big\}. \end{aligned} \tag{2.9}$$

Furthermore, the Laplacian can be expressed as

$$\Delta (f) = \frac{1}{|J|} \partial_s \left(\frac{r^2}{|J|} \partial_s \, f \right) + \frac{1}{|J|} \partial_r \Big(|J| \partial_r \, f \Big) + \frac{1}{|J|} \partial_\theta \left(\frac{|J|}{r^2} \partial_\theta \, f \right).$$

The Lapacian, by definition, is

$$\Delta (f) \equiv \nabla \cdot \nabla (f) \,.$$

In (s,r,θ)-coordinates, we have

$$\begin{aligned}
\Delta(f) &= \frac{1}{|J|}\nabla_c\cdot\left(|J|\left(J^TJ\right)^{-1}\nabla_c(f)\right)\\
&= \frac{1}{|J|}\partial_s\left(\frac{r^2}{|J|}\partial_s(f)\right)+\frac{1}{|J|}\partial_r\left(|J|\partial_r(f)\right)+\frac{1}{|J|}\partial_\theta\left(\frac{|J|}{r^2}\partial_\theta(f)\right)\\
&= \left(\frac{r}{|J|}\right)^2\partial_{ss}(f)+\frac{1}{|J|}\partial_s\left(\frac{r^2}{|J|}\right)\partial_s(f)+\partial_{rr}(f)+\frac{1}{|J|}\partial_r(|J|)\,\partial_r(f)\\
&\quad+\frac{1}{r^2}\partial_{\theta\theta}(f)+\frac{1}{|J|}\partial_\theta\left(\frac{|J|}{r^2}\right)\partial_\theta(f)\\
&= \left(\left(J^TJ\right)^{-1}\nabla_c\right)\cdot\nabla_c(f)+\frac{1}{|J|}\nabla_c\left(|J|\mathbf{diag}\left(\left(J^TJ\right)^{-1}\right)\right)\cdot\nabla_c(f)
\end{aligned}$$

One important property of our laplacian is

$$\Delta(fg)=f\Delta(g)+2\nabla(f)\cdot\nabla(g)+g\Delta(f)$$

for any functions f,g. In (s,r,θ)-coordinates,

$$\Delta(fg)=f\Delta(g)+2\left(\left(J^TJ\right)^{-1}\nabla_c\right)(f)\cdot\nabla_c(g)+g\Delta(f).$$

Now, we have

$$\begin{aligned}
\frac{D}{Dt}(\rho\mathbf{V}_c) &= \frac{D}{Dt}\left(\rho J^{-1}\mathbf{V}\right)\\
&= \frac{D}{Dt}\left(J^{-1}\right)\rho\mathbf{V}+J^{-1}\frac{D}{Dt}(\rho\mathbf{V})\\
&= \frac{D}{Dt}\left(J^{-1}\right)J\rho\mathbf{V}_c+J^{-1}\Big[-\nabla(P)+\nu\Delta(\mathbf{V})-\rho g\mathbf{e}_3\Big]\\
&= \frac{D}{Dt}\left(J^{-1}\right)J\rho\mathbf{V}_c-J^{-1}\left(J^T\right)^{-1}\nabla_c(P)-\rho gJ^{-1}\mathbf{e}_3+\nu J^{-1}\Delta(\mathbf{V})\\
&= \frac{D}{Dt}\left(J^{-1}\right)J\rho\mathbf{V}_c-\left(J^TJ\right)^{-1}\nabla_c(P)-\rho gJ^{-1}\mathbf{e}_3\\
&\quad+\nu J^{-1}\Big[J\Delta(\mathbf{V}_c)+\frac{2r^2}{|J|^2}\partial_s(J)\,\partial_s(\mathbf{V}_c)+2\partial_r(J)\,\partial_r(\mathbf{V}_c)\\
&\quad+\frac{2}{r^2}\partial_\theta(J)\,\partial_\theta(\mathbf{V}_c)+\frac{1}{|J|}\partial_s\left(\frac{r^2}{|J|}\right)\partial_s(J)\,\mathbf{V}_c+\frac{1}{|J|}\partial_r(|J|)\,\partial_r(J)\,\mathbf{V}_c\\
&\quad+\frac{1}{|J|}\partial_\theta\left(\frac{|J|}{r^2}\right)\partial_\theta(J)\,\mathbf{V}_c+\frac{r^2}{|J|^2}\partial_{ss}(J)\,\mathbf{V}_c+\partial_{rr}(J)\,\mathbf{V}_c+\frac{1}{r^2}\partial_{\theta\theta}(J)\,\mathbf{V}_c\Big].
\end{aligned}$$

In order to summarize the calculations, we present the following list.

- $\frac{D}{Dt}\left(J^{-1}\right)J$.

$$\frac{D}{Dt}\left(J^{-1}\right) = \begin{pmatrix} -\left(\frac{r}{|J|}\right)^2\left(\nabla_c\left(\frac{|J|}{r}\right)\cdot\mathbf{V}_c\right)\mathbf{J}_s^T + \alpha'(s)\frac{r}{|J|}V_s\mathbf{J}_s^{\perp T} \\ \partial_r\left(\frac{|J|}{r}\right)V_s\mathbf{J}_s^T + \tilde{v}\mathbf{J}_\theta^T \\ \frac{1}{r^2}\partial_\theta\left(\frac{|J|}{r}\right)V_s\mathbf{J}_s^T - \frac{1}{r}\tilde{v}\mathbf{J}_r^T - \frac{1}{r^2}V_r\mathbf{J}_\theta^T \end{pmatrix}$$

$$\frac{D}{Dt}\left(J^{-1}\right)J = \begin{pmatrix} -\frac{r}{|J|}\nabla_c\left(\frac{|J|}{r}\right)\cdot\mathbf{V}_c & -\frac{r}{|J|}\partial_r\left(\frac{|J|}{r}\right)V_s & -\frac{r}{|J|}\partial_\theta\left(\frac{|J|}{r}\right)V_s \\ \frac{|J|}{r}\partial_r\left(\frac{|J|}{r}\right)V_s & 0 & rV_\theta \\ \frac{1}{r^2}\frac{|J|}{r}\partial_\theta\left(\frac{|J|}{r}\right)V_s & -\frac{1}{r}V_\theta & -\frac{1}{r}V_r \end{pmatrix}$$

- $J^{-1}\partial_s(J)$.

$$\partial_s(J) = \begin{pmatrix} \partial_s\left(\frac{|J|}{r}\right)\mathbf{J}_s + \alpha'(s)\frac{|J|}{r}\mathbf{J}_s^{\perp} & \partial_r\left(\frac{|J|}{r}\right)\mathbf{J}_s & \partial_\theta\left(\frac{|J|}{r}\right)\mathbf{J}_s \end{pmatrix}$$

$$J^{-1}\partial_s(J) = \begin{pmatrix} \frac{r}{|J|}\partial_s\left(\frac{|J|}{r}\right) & \frac{r}{|J|}\partial_r\left(\frac{|J|}{r}\right) & \frac{r}{|J|}\partial_\theta\left(\frac{|J|}{r}\right) \\ -\frac{|J|}{r}\partial_r\left(\frac{|J|}{r}\right) & 0 & 0 \\ -\frac{1}{r^2}\frac{|J|}{r}\partial_\theta\left(\frac{|J|}{r}\right) & 0 & 0 \end{pmatrix}$$

- $J^{-1}\partial_r(J)$.

$$\begin{aligned}\partial_r(J) &= \begin{pmatrix} \partial_r\left(\frac{|J|}{r}\right)\mathbf{J}_s & \mathbf{0} & \mathbf{J}_\theta \end{pmatrix} \\ J^{-1}\partial_r(J) &= \begin{pmatrix} \frac{r}{|J|}\partial_r\left(\frac{|J|}{r}\right) & 0 & 0 \\ 0 & 0 & 0 \\ 0 & 0 & \frac{1}{r} \end{pmatrix}\end{aligned}$$

- $J^{-1}\partial_\theta(J)$.

$$\begin{aligned}\partial_\theta(J) &= \begin{pmatrix} \partial_\theta\left(\frac{|J|}{r}\right)\mathbf{J}_s & \mathbf{J}_\theta & -r\mathbf{J}_r \end{pmatrix} \\ J^{-1}\partial_\theta(J) &= \begin{pmatrix} \frac{r}{|J|}\partial_\theta\left(\frac{|J|}{r}\right) & 0 & 0 \\ 0 & 0 & -r \\ 0 & \frac{1}{r} & 0 \end{pmatrix}\end{aligned}$$

- $J^{-1}\partial_{ss}(J)$.

$$\partial_{ss}(J) = \begin{pmatrix} \left[\partial_{ss}\left(\frac{|J|}{r}\right) - (\alpha'(s))^2\frac{|J|}{r}\right]\mathbf{J}_s + & \partial_{sr}\left(\frac{|J|}{r}\right)\mathbf{J}_s + & \partial_{s\theta}\left(\frac{|J|}{r}\right)\mathbf{J}_s + \\ \left[\alpha'(s)\partial_s\left(\frac{|J|}{r}\right) + \partial_s\left(\alpha'(s)\frac{|J|}{r}\right)\right]\mathbf{J}_s^\perp & \alpha'(s)\partial_r\left(\frac{|J|}{r}\right)\mathbf{J}_s^\perp & \alpha'(s)\partial_\theta\left(\frac{|J|}{r}\right)\mathbf{J}_s^\perp \end{pmatrix}$$

$$J^{-1}\partial_{ss}(J) = \begin{pmatrix} \frac{r}{|J|}\left[\partial_{ss}\left(\frac{|J|}{r}\right) - (\alpha'(s))^2\frac{|J|}{r}\right] & \frac{r}{|J|}\partial_{sr}\left(\frac{|J|}{r}\right) & \frac{r}{|J|}\partial_{s\theta}\left(\frac{|J|}{r}\right) \\ -\partial_s\left(\frac{|J|}{r}\right)\partial_r\left(\frac{|J|}{r}\right) - \partial_s\left(\frac{|J|}{r}\partial_r\left(\frac{|J|}{r}\right)\right) & -\left[\partial_r\left(\frac{|J|}{r}\right)\right]^2 & -\partial_r\left(\frac{|J|}{r}\right)\partial_\theta\left(\frac{|J|}{r}\right) \\ -\frac{1}{r^2}\left[\partial_s\left(\frac{|J|}{r}\right)\partial_\theta\left(\frac{|J|}{r}\right) + \partial_s\left(\frac{|J|}{r}\partial_\theta\left(\frac{|J|}{r}\right)\right)\right] & -\frac{1}{r^2}\partial_r\left(\frac{|J|}{r}\right)\partial_\theta\left(\frac{|J|}{r}\right) & -\frac{1}{r^2}\left[\partial_\theta\left(\frac{|J|}{r}\right)\right]^2 \end{pmatrix}$$

- $J^{-1}\partial_{rr}(J)$.

$$\partial_{rr}(J) = \begin{pmatrix} \mathbf{0} & \mathbf{0} & \mathbf{0} \end{pmatrix}$$

$$J^{-1}\partial_{\theta}(J) = \begin{pmatrix} 0 & 0 & 0 \\ 0 & 0 & 0 \\ 0 & 0 & 0 \end{pmatrix}$$

- $J^{-1}\partial_{\theta\theta}(J)$.

$$\partial_{\theta\theta}(J) = \begin{pmatrix} \partial_{\theta\theta}\left(\frac{|J|}{r}\right)\mathbf{J}_s & -\mathbf{J}_r & -r\mathbf{J}_{\theta} \end{pmatrix}$$

$$J^{-1}\partial_{\theta}(J) = \begin{pmatrix} \frac{r}{|J|}\partial_{\theta\theta}\left(\frac{|J|}{r}\right) & 0 & 0 \\ 0 & -1 & 0 \\ 0 & 0 & -1 \end{pmatrix}$$

Now, let expand the matrix

$$
\begin{aligned}
&\tfrac{D}{Dt}\left(\rho\mathbf{V}_c\right) = \\
&\begin{pmatrix} -\frac{r}{|J|}\nabla_c\left(\frac{|J|}{r}\right)\cdot\mathbf{V}_c & -\frac{r}{|J|}\partial_r\left(\frac{|J|}{r}\right)V_s & -\frac{r}{|J|}\partial_\theta\left(\frac{|J|}{r}\right)V_s \\ \frac{|J|}{r}\partial_r\left(\frac{|J|}{r}\right)V_s & 0 & rV_\theta \\ \frac{1}{r^2}\frac{|J|}{r}\partial_\theta\left(\frac{|J|}{r}\right)V_s & -\frac{1}{r}V_\theta & -\frac{1}{r}V_r \end{pmatrix}\rho\mathbf{V}_c - \begin{pmatrix} \left(\frac{r}{|J|}\right)^2 & 0 & 0 \\ 0 & 1 & 0 \\ 0 & 0 & \frac{1}{r^2} \end{pmatrix}\nabla_c\left(P\right) \\
&-\rho g\begin{pmatrix} \frac{r}{|J|}\mathbf{J}_s^T \\ \mathbf{J}_r^T \\ \frac{1}{r}\mathbf{J}_\theta^T \end{pmatrix}\mathbf{e}_3 + \nu\Big\{\Delta\left(\mathbf{V}_c\right) + 2\begin{pmatrix} \frac{r}{|J|}\partial_r\left(\frac{|J|}{r}\right) & 0 & 0 \\ 0 & 0 & 0 \\ 0 & 0 & \frac{1}{r} \end{pmatrix}\partial_r\left(\mathbf{V}_c\right) + \tfrac{2}{r^2}\begin{pmatrix} \frac{r}{|J|}\partial_\theta\left(\frac{|J|}{r}\right) & 0 & 0 \\ 0 & 0 & -r \\ 0 & \frac{1}{r} & 0 \end{pmatrix}\partial_\theta\left(\mathbf{V}_c\right) \\
&+\tfrac{2r^2}{|J|^2}\begin{pmatrix} \frac{r}{|J|}\partial_s\left(\frac{|J|}{r}\right) & \frac{r}{|J|}\partial_r\left(\frac{|J|}{r}\right) & \frac{r}{|J|}\partial_\theta\left(\frac{|J|}{r}\right) \\ -\frac{|J|}{r}\partial_r\left(\frac{|J|}{r}\right) & 0 & 0 \\ -\frac{1}{r^2}\frac{|J|}{r}\partial_\theta\left(\frac{|J|}{r}\right) & 0 & 0 \end{pmatrix}\partial_s\left(\mathbf{V}_c\right) + \tfrac{1}{|J|}\partial_r\left(|J|\right)\begin{pmatrix} \frac{r}{|J|}\partial_r\left(\frac{|J|}{r}\right) & 0 & 0 \\ 0 & 0 & 0 \\ 0 & 0 & \frac{1}{r} \end{pmatrix}\mathbf{V}_c \\
&+\tfrac{1}{|J|}\partial_\theta\left(\tfrac{|J|}{r^2}\right)\begin{pmatrix} \frac{r}{|J|}\partial_\theta\left(\frac{|J|}{r}\right) & 0 & 0 \\ 0 & 0 & -r \\ 0 & \frac{1}{r} & 0 \end{pmatrix}\mathbf{V}_c + \tfrac{1}{|J|}\partial_s\left(\tfrac{r^2}{|J|}\right)\begin{pmatrix} \frac{r}{|J|}\partial_s\left(\frac{|J|}{r}\right) & \frac{r}{|J|}\partial_r\left(\frac{|J|}{r}\right) & \frac{r}{|J|}\partial_\theta\left(\frac{|J|}{r}\right) \\ -\frac{|J|}{r}\partial_r\left(\frac{|J|}{r}\right) & 0 & 0 \\ -\frac{1}{r^2}\frac{|J|}{r}\partial_\theta\left(\frac{|J|}{r}\right) & 0 & 0 \end{pmatrix}\mathbf{V}_c \\
&+\left(\tfrac{r}{|J|}\right)^2\begin{pmatrix} \frac{r}{|J|}\left[\partial_{ss}\left(\frac{|J|}{r}\right) - \left(\alpha'\left(s\right)\right)^2\frac{|J|}{r}\right] & \frac{r}{|J|}\partial_{sr}\left(\frac{|J|}{r}\right) & \frac{r}{|J|}\partial_{s\theta}\left(\frac{|J|}{r}\right) \\ -\partial_s\left(\frac{|J|}{r}\right)\partial_r\left(\frac{|J|}{r}\right) - \partial_s\left(\frac{|J|}{r}\partial_r\left(\frac{|J|}{r}\right)\right) & -\left[\partial_r\left(\frac{|J|}{r}\right)\right]^2 & -\partial_r\left(\frac{|J|}{r}\right)\partial_\theta\left(\frac{|J|}{r}\right) \\ -\frac{1}{r^2}\left[\partial_s\left(\frac{|J|}{r}\right)\partial_\theta\left(\frac{|J|}{r}\right) + \partial_s\left(\frac{|J|}{r}\partial_\theta\left(\frac{|J|}{r}\right)\right)\right] & -\frac{1}{r^2}\partial_r\left(\frac{|J|}{r}\right)\partial_\theta\left(\frac{|J|}{r}\right) & -\frac{1}{r^2}\left[\partial_\theta\left(\frac{|J|}{r}\right)\right]^2 \end{pmatrix}\mathbf{V}_c \\
&+\tfrac{1}{r^2}\begin{pmatrix} \frac{r}{|J|}\partial_{\theta\theta}\left(\frac{|J|}{r}\right) & 0 & 0 \\ 0 & -1 & 0 \\ 0 & 0 & -1 \end{pmatrix}\mathbf{V}_c\Big\}
\end{aligned}
$$

Straightforward but long calculations gives the Navier-Stokes equations combined with the incompressibility conditions (2.2) in cylindrical coordinates (2.1). The new system is

given by

$$
\begin{aligned}
\tfrac{D}{Dt}(\rho) &= 0,\\
\tfrac{D}{Dt}\left(\rho\left[\tfrac{|J|}{r}\right]^2 V_s\right) &= -\partial_s P_2 + \tfrac{|J|}{r}\partial_s\left(\tfrac{|J|}{r}\right)\rho V_s^2 - \sin(\alpha(s))\,\rho g,\\
&\quad +\nu\Bigg\{\Delta\left(\left[\tfrac{|J|}{r}\right]^2 V_s\right) - \Delta\left(\left[\tfrac{|J|}{r}\right]^2\right)V_s + 2\tfrac{r}{|J|}\partial_r\left[\tfrac{|J|}{r}\right]\partial_s(V_r)\\
&\quad +2\tfrac{r}{|J|}\partial_\theta\left(\tfrac{|J|}{r}\right)\partial_s(V_\theta) + \nabla_c\left(\tfrac{r}{|J|}\partial_s\left(\tfrac{|J|}{r}\right)\right)\cdot\mathbf{V}_c\Bigg\},\\
\tfrac{D}{Dt}(\rho V_r) &= -\partial_r(P_2) + \tfrac{|J|}{r}\partial_r\left(\tfrac{|J|}{r}\right)\rho V_s^2 + r\rho V_\theta^2\\
&\quad +\nu\Bigg\{\Delta(V_r) - 2\tfrac{r}{|J|}\partial_r\left(\tfrac{|J|}{r}\right)\partial_s(V_s) - \tfrac{2}{r}\partial_\theta(V_\theta)\\
&\quad -\left(\tfrac{r}{|J|}\right)^2\partial_s\left(\tfrac{|J|}{r}\partial_r\left(\tfrac{|J|}{r}\right)\right)V_s\\
&\quad -\tfrac{1}{|J|^2}\left[\left(\tfrac{|J|}{r}\right)^2 + \left(\tfrac{|J|}{r}-1\right)^2\right]V_r - \tfrac{\partial_r(|J|)\partial_\theta(|J|)}{|J|^2}V_\theta\Bigg\},\\
\tfrac{D}{Dt}(\rho r^2 V_\theta) &= -\partial_\theta(P_2) + \tfrac{|J|}{r}\partial_\theta\left(\tfrac{|J|}{r}\right)\rho V_s^2\\
&\quad +\nu\Bigg\{\Delta(r^2 V_\theta) - 2\tfrac{r}{|J|}\partial_\theta\left(\tfrac{|J|}{r}\right)\partial_s(V_s)\\
&\quad +\tfrac{2}{r}\partial_\theta(V_r) - \tfrac{2}{|J|}\partial_r(|J|rV_\theta) - \left[\tfrac{r}{|J|}\right]^2\partial_s\left(\tfrac{|J|}{r}\partial_\theta\left(\tfrac{|J|}{r}\right)\right)V_s\\
&\quad +\tfrac{r}{|J|^2}\partial_\theta\left(\tfrac{|J|}{r}\right)V_r - \left[\tfrac{r}{|J|}\partial_\theta\left(\tfrac{|J|}{r}\right)\right]^2 V_\theta\Bigg\},\\
\nabla_c\cdot(|J|\mathbf{V}_c) &= 0,
\end{aligned}
\tag{2.10}
$$

where $P_2 = P + r\cos(\alpha(s))\sin(\theta)\rho g$ is the transmural pressure.

2.1.2 The dimensionless equations

We carry out an asymptotic analysis to remove small terms in the equations that do not add a significant contribution in the budget and allows us to simplify the model. Following [9], we define $V_{s,0}$, $V_{r,0}$, and $V_{\theta,0}$ be the characteristic radial, axial and angular velocities. Let also λ and R_0 be the characteristic axial and radial lengthscales. Each quantity is non-dimensionalized as $r = R_0\tilde{r}$, $s = \lambda\tilde{s}$, $t = \frac{\lambda}{V_0}\tilde{t}$, $V_s = V_{s,0}\tilde{V}_s$, $V_r = V_{r,0}\tilde{V}_r$, $V_\theta = V_{\theta,0}\tilde{V}_\theta$, $P = \rho V_0^2\tilde{P}$.

The dimensionless version of (2.10) is given by

$$
\begin{aligned}
\tilde{\frac{D}{Dt}}\left(\tilde{\rho}\right) &= 0 \\
\tilde{\frac{D}{Dt}}\left(\tilde{\rho}\left[\tilde{\frac{|J|}{r}}\right]^2\tilde{V}_s\right) &= -\tilde{\frac{[P]}{\rho_0 V_{s,0}^2}}\tilde{\partial}_s\,\tilde{P}_2 - \tilde{\frac{gT}{V_{s,0}}}\sin\left(\alpha\left(s\right)\right)\tilde{\rho} + \tilde{\frac{|J|}{r}}\tilde{\partial}_s\left(\tilde{\frac{|J|}{r}}\right)\tilde{\rho}\tilde{V_s}^2 \\
&\quad + \tilde{\frac{\nu T}{\rho_0 R_0^2}}\Bigg\{\left(\frac{R_0}{\lambda}\right)^2\tilde{\frac{1}{|J|}}\tilde{\partial}_s\left(\tilde{\frac{r^2}{|J|}}\tilde{\partial}_s\left(\left[\tilde{\frac{|J|}{r}}\right]^2\tilde{V}_s\right)\right) \\
&\quad + \tilde{\frac{1}{|J|}}\tilde{\partial}_r\left(|\tilde{J}|\tilde{\partial}_r\left(\left[\tilde{\frac{|J|}{r}}\right]^2\tilde{V}_s\right)\right) + \tilde{\frac{1}{|J|}}\tilde{\partial}_\theta\left(\tilde{\frac{|J|}{r^2}}\tilde{\partial}_\theta\left(\left[\tilde{\frac{|J|}{r}}\right]^2\tilde{V}_s\right)\right) \\
&\quad + 2\tilde{\frac{r}{|J|}}\tilde{\partial}_r\left(\tilde{\frac{|J|}{r}}\right)\tilde{\partial}_s\left(\tilde{V}_r\right) + 2\tilde{\frac{r}{|J|}}\tilde{\partial}_\theta\left(\tilde{\frac{|J|}{r}}\right)\tilde{\partial}_s\left(\tilde{V}_\theta\right) \\
&\quad + \left(\frac{R_0}{\lambda}\right)^2\tilde{\nabla}_c\left(\tilde{\frac{r}{|J|}}\tilde{\partial}_s\left(\tilde{\frac{|J|}{r}}\right)\right)\cdot\tilde{\mathbf{V}}_c \\
&\quad - \left(\frac{R_0}{\lambda}\right)^2\tilde{\frac{1}{|J|}}\tilde{\partial}_s\left(\tilde{\frac{r^2}{|J|}}\tilde{\partial}_s\left(\left[\tilde{\frac{|J|}{r}}\right]^2\right)\right)\tilde{V}_s \\
&\quad - \tilde{\frac{1}{|J|}}\tilde{\partial}_r\left(|\tilde{J}|\tilde{\partial}_r\left(\left[\tilde{\frac{|J|}{r}}\right]^2\right)\right)\tilde{V}_s - \tilde{\frac{1}{|J|}}\tilde{\partial}_\theta\left(\tilde{\frac{|J|}{r^2}}\tilde{\partial}_\theta\left(\left[\tilde{\frac{|J|}{r}}\right]^2\right)\right)\tilde{V}_s\Bigg\} \\
\tilde{\frac{D}{Dt}}\left(\tilde{\rho}\tilde{V}_r\right) &= -\tilde{\frac{[P]}{\rho_0 V_{r,0}^2}}\tilde{\partial}_r\,\tilde{P}_2 + \left(\frac{V_{s,0}}{V_{r,0}}\right)^2\tilde{\frac{|J|}{r}}\tilde{\partial}_r\left(\tilde{\frac{|J|}{r}}\right)\tilde{\rho}\tilde{V_s}^2 + \tilde{\rho}\tilde{r}\tilde{V_\theta}^2 \\
&\quad + \tilde{\frac{\nu T}{\rho_0 R_0^2}}\Bigg\{\left(\frac{R_0}{\lambda}\right)^2\tilde{\frac{1}{|J|}}\tilde{\partial}_s\left(\tilde{\frac{r^2}{|J|}}\tilde{\partial}_s\left(\tilde{V}_r\right)\right) + \tilde{\frac{1}{|J|}}\tilde{\partial}_r\left(|\tilde{J}|\tilde{\partial}_r\left(\tilde{V}_r\right)\right) \\
&\quad + \tilde{\frac{1}{|J|}}\tilde{\partial}_\theta\left(\tilde{\frac{|J|}{r^2}}\tilde{\partial}_\theta\left(\tilde{V}_r\right)\right) - 2\tilde{\frac{r}{|J|}}\tilde{\partial}_r\left(\tilde{\frac{|J|}{r}}\right)\tilde{\partial}_s\left(\tilde{V}_s\right) - \tilde{\frac{2}{r}}\tilde{\partial}_\theta\left(\tilde{V}_\theta\right) \\
&\quad - \left(\tilde{\frac{r}{|J|}}\right)^2\tilde{\partial}_r\left(\tilde{\frac{|J|}{r}}\right)\tilde{\nabla}_c\left(\tilde{\frac{|J|}{r}}\right)\cdot\tilde{\mathbf{V}}_c \\
&\quad - \tilde{\frac{r}{|J|}}\tilde{\partial}_s\tilde{\partial}_r\left(\tilde{\frac{|J|}{r}}\right)\tilde{V}_s - \tilde{\frac{1}{r^2}}\tilde{V}_r - \tilde{\frac{1}{|J|}}\tilde{\partial}_\theta\left(\tilde{\frac{|J|}{r}}\right)\tilde{V}_\theta\Bigg\} \\
\tilde{\frac{D}{Dt}}\left(\tilde{\rho}\left(\tilde{r}\right)^2\tilde{V}_\theta\right) &= -\tilde{\frac{[P]}{\rho_0 R_0^2 V_{\theta,0}^2}}\tilde{\partial}_\theta\,\tilde{P}_2 + \left(\frac{V_{s,0}}{R_0 V_{\theta,0}}\right)^2\tilde{\frac{|J|}{r}}\tilde{\partial}_\theta\left(\tilde{\frac{|J|}{r}}\right)\tilde{\rho}\tilde{V_s}^2 \\
&\quad + \tilde{\frac{\nu T}{\rho_0 R_0^2}}\Bigg\{\left(\frac{R_0}{\lambda}\right)^2\tilde{\frac{1}{|J|}}\tilde{\partial}_s\left(\tilde{\frac{r^2}{|J|}}\tilde{\partial}_s\left(\left(\tilde{r}\right)^2\tilde{V}_\theta\right)\right) + \tilde{\frac{1}{|J|}}\tilde{\partial}_r\left(|\tilde{J}|\tilde{\partial}_r\left(\left(\tilde{r}\right)^2\tilde{V}_\theta\right)\right) \\
&\quad + \tilde{\frac{1}{|J|}}\tilde{\partial}_\theta\left(\tilde{\frac{|J|}{r^2}}\tilde{\partial}_\theta\left(\left(\tilde{r}\right)^2\tilde{V}_\theta\right)\right) - \tilde{\frac{2r}{|J|}}\tilde{\partial}_\theta\left(\tilde{\frac{|J|}{r}}\right)\tilde{\partial}_s\left(\tilde{V}_s\right) + \tilde{\frac{2}{r}}\tilde{\partial}_\theta\left(\tilde{V}_r\right) \\
&\quad - \tilde{\frac{2}{|J|}}\tilde{\partial}_r\left(|\tilde{J}|\tilde{r}\tilde{V}_\theta\right) - \left[\tilde{\frac{r}{|J|}}\right]^2\tilde{\partial}_s\left(\tilde{\frac{|J|}{r}}\tilde{\partial}_\theta\left(\tilde{\frac{|J|}{r}}\right)\right)\tilde{V}_s \\
&\quad - \tilde{\frac{r}{|J|^2}}\tilde{\partial}_\theta\left(\tilde{\frac{|J|}{r}}\right)\tilde{V}_r - \left[\tilde{\frac{r}{|J|}}\tilde{\partial}_\theta\left(\tilde{\frac{|J|}{r}}\right)\right]^2\tilde{V}_\theta\Bigg\} \\
\tilde{\nabla}_c\cdot\left(|\tilde{J}|\tilde{\mathbf{V}}_c\right) &= 0.
\end{aligned}
\tag{2.11}
$$

The small parameter in this expansion is the ratio between radial and axial lengthscales

$$\epsilon := \frac{R_o}{\lambda} = \frac{V_{r,o}}{V_{s,o}}. \tag{2.12}$$

Typical values in the aorta between the renal and the iliac arteries gives $\epsilon \approx 10^{-2}$ [9]. Furthermore, we assume that the gravity g, the scales of pressure ($[P]$), radius (R_o), time (T), axial and linear angular velocities ($V_{s,o}, V_{\theta,o}$) satisfy

$$\frac{[P]}{\rho_o V_{s,o}^2} = \mathcal{O}(1), \quad \frac{V_{s,o}}{R_o V_{\theta,o}} = \mathcal{O}(1), \quad \frac{gT}{V_{s,o}} = \mathcal{O}(1). \tag{2.13}$$

Under these assumptions, the acceleration of gravity is comparable to the characteristic acceleration of the system in the axial direction. This is reasonable for typical velocities of order $\mathcal{O}(1\ \mathrm{ms}^{-1})$ and a timescale of $T = 0.1$ s. On the other hand, the change of variables is valid provided $r|\alpha'(s)| < 1$. As a stronger assumption, we assume that $r\alpha'(s)$ is small, which implies that the artery's radius of curvature is large compared to its cross-sectional radius. On the other hand, an approximate value for blood viscosity in arteries can be taken as a constant $\nu = 4$ cP $= 4 \times 10^{-2}$ g (s cm)$^{-1}$ [18]. Using $\rho_o = 1050$ kg m^{-3}, and $R_o = 0.82$ cm, it gives us $\frac{\nu T}{\rho_o R_o^2} = 0.56 \times 10^{-2}$. Based on this estimation, we assume

$$R_o\,|\alpha'(s)| = \mathcal{O}\left(\epsilon\right), \quad \text{and} \quad \frac{\nu T}{\rho_o R_o^2} = \mathcal{O}\left(\epsilon\right). \tag{2.14}$$

There is just one leading order term in the momentum equation in the radial direction that is found as follows. The first term in the right-hand side has a factor of

$$\frac{[P]}{\rho_o V_{r,o}^2} = \frac{[P]}{\rho_o V_{s,o}^2}\frac{V_{s,o}^2}{V_{r,o}^2} = \mathcal{O}(\epsilon^{-2}).$$

The second term has a factor of order $\mathcal{O}(\epsilon^{-2})$. However, we ignore that term because

$$\partial_r(|J|/r) = -\sin(\theta)\alpha'(s)R_o = \mathcal{O}(\epsilon).$$

The viscosity terms are all order $\mathcal{O}(\epsilon)$ or higher, and the left-hand side is $\mathcal{O}(1)$. Thus, taking the leading order term, we obtain

$$\partial_{\tilde{r}} \left(\tilde{P}_2 \right) = 0,$$

which implies that $\tilde{P}_2$ is independent of $\tilde{r}$. In the equation of balance for the angular momentum, we will exclude only terms that are order $\mathcal{O}(\epsilon)$ or higher to keep the contribution of the artery's curvature on the flow. The first term in the right-hand side has a factor

$$\frac{[P]}{\rho_o (R_o V_{\theta,o})^2} = \frac{[P]}{\rho_o V_{s,o}^2} \frac{V_{s,o}^2}{(R_o V_{\theta,o})^2} = \mathcal{O}(1),$$

and we keep it. As discussed above, the non-dimensional parameter involving the viscosity term is order $\mathcal{O}(\epsilon)$. For the terms inside the brackets, we assume that rV_θ, V_r and $|J|/r$ depend all weakly on θ, which is consistent with the fact that the blood flow moves mainly in the axial direction. As a result, only two terms in front of the viscosity coefficient have a leading contribution, as specified below in equation (2.15).

Similarly, we only exclude terms in the momentum equation that are order $\mathcal{O}(\epsilon)$ or higher. All the terms before the viscosity coefficient are order $\mathcal{O}(1)$ or $\mathcal{O}(\epsilon)$. Only one viscosity term inside the brackets has a leading contribution. The other terms have either a factor of order $\mathcal{O}(\epsilon)$, or can be neglected due to the weak dependance on θ.

The averaged leading order equations

After removing terms of order $\mathcal{O}(\epsilon^2)$ in the dimensionaless equations (2.11), we obtain

$$
\begin{aligned}
|\tilde{J}|\frac{\tilde{D}}{Dt}\left(\tilde{\rho}\right) &= 0, && \text{(2.15a)}\\
|\tilde{J}|\frac{\tilde{D}}{Dt}\left(\tilde{\rho}\left[\frac{|\tilde{J}|}{\tilde{r}}\right]^2\tilde{V}_s\right) &= \tilde{r}\left(\frac{|\tilde{J}|}{\tilde{r}}\right)^2\tilde{\partial}_s\left(\frac{|\tilde{J}|}{\tilde{r}}\right)\tilde{\rho}\tilde{V_s}^2 - \frac{[P]}{\rho_0 V_{s,0}^2}|\tilde{J}|\tilde{\partial}_s\left(\tilde{P}_2\right)\\
&\quad -\frac{gT}{V_{s,0}}\sin\left(\alpha\left(s\right)\right)|\tilde{J}|\tilde{\rho} + \frac{\nu T}{\rho_0 R_0^2}\tilde{\partial}_r\left(|\tilde{J}|\tilde{\partial}_r\left(\left[\frac{|\tilde{J}|}{\tilde{r}}\right]^2\tilde{V}_s\right)\right), && \text{(2.15b)}\\
|\tilde{J}|\frac{\tilde{D}}{Dt}\left(\tilde{\rho}\left(\tilde{r}\right)^2\tilde{V}_\theta\right) &= \tilde{r}\left(\frac{|\tilde{J}|}{\tilde{r}}\right)^2\tilde{\partial}_\theta\left(\frac{|\tilde{J}|}{\tilde{r}}\right)\tilde{\rho}\tilde{V_s}^2 - \frac{[P]}{\rho_0 V_{s,0}^2}|\tilde{J}|\tilde{\partial}_\theta\left(\tilde{P}_2\right)\\
&\quad + \frac{\nu T}{\rho_0 R_0^2}\tilde{\partial}_r\left(|\tilde{J}|\left[\tilde{\partial}_r\left(\left(\tilde{r}\right)^2\tilde{V}_\theta\right) - 2\tilde{r}\tilde{V}_\theta\right]\right), && \text{(2.15c)}\\
\tilde{\nabla}_c\cdot\left(|\tilde{J}|\tilde{\mathbf{V}}_c\right) &= 0. && \text{(2.15d)}
\end{aligned}
$$

Going back with units, we have that

$$
\begin{aligned}
|J|\frac{D}{Dt}\left(\rho\right) &= 0\\
|J|\frac{D}{Dt}\left(\rho\left[\frac{|J|}{r}\right]^2 V_s\right) &= r\left[\frac{|J|}{r}\right]^2\partial_s\left(\frac{|J|}{r}\right)\rho V_s^2 - |J|\partial_s\left(P_2\right) - |J|\sin\left(\alpha\left(s\right)\right)\rho g\\
&\quad +\nu\partial_r\left(|J|\partial_r\left(\left[\frac{|J|}{r}\right]^2 V_s\right)\right)\\
|J|\frac{D}{Dt}\left(\rho r^2 V_\theta\right) &= r\left[\frac{|J|}{r}\right]^2\partial_\theta\left(\frac{|J|}{r}\right)\rho V_s^2 - |J|\partial_\theta\left(P_2\right)\\
&\quad +\nu\partial_r\left(|J|\left[\partial_r\left(r^2 V_\theta\right) - 2rV_\theta\right]\right)\\
\nabla_c\cdot\left(|J|\mathbf{V}_c\right) &= 0.
\end{aligned}
$$

Although our system has 5 variables (V_s, V_r, V_θ, P_2 and ρ) and 4 equations, we will provide a closed-form of the pressure in terms of the radially-integrated Jacobian, as presented in the next section. This closed-forms brings us a way to get a system of 3 equations with 3 variables which are conservation laws without non-conservative terms.

2.2 The main system

Let $R(s,\theta,t)$ denote the vessel's cross-sectional radius at each position s, angle θ and time t. Using (2.9), the incompressibility equation (2.15d) and the Leibniz integral rule, we have

$$\begin{aligned}\int_o^R |J|\frac{Df}{Dt}dr &= \partial_t\left(\int_o^R f|J|dr\right)+\partial_s\left(\int_o^R fV_s|J|dr\right)+\partial_\theta\left(\int_o^R fV_\theta|J|dr\right)\\ &\quad+\Big[f|J|\Big]_{r=R}\Big\{[V_r]_{r=R}-\partial_t(R)-[V_s]_{r=R}\,\partial_s(R)-[V_\theta]_{r=R}.\partial_\theta(R)\Big\}\end{aligned}$$

After an integration in the radial direction of (2.15a)-(2.15c) assuming a streamline condition

$$[V_r]_{r=R}=\partial_t(R)+[V_s]_{r=R}\,\partial_s(R)+[V_\theta]_{r=R}\,\partial_\theta(R)$$

at the artery's wall and a slowly varying density, which is approximated by a constant value respect to r, we obtain

$$\begin{array}{llll}
\partial_t\left(\int_0^R|J|dr\right) & + \partial_s\left(\int_0^R V_s|J|dr\right) & + \partial_\theta\left(\int_0^R V_\theta|J|dr\right) & = 0\\
\partial_t\left(\int_0^R\left[\frac{|J|}{r}\right]^2V_s|J|dr\right) & + \partial_s\left(\int_0^R\left[\frac{|J|}{r}\right]^2V_s^2|J|dr\right) & + \partial_\theta\left(\int_0^R\left[\frac{|J|}{r}\right]^2V_sV_\theta|J|dr\right) & \\
 & = \int_0^R r\left[\frac{|J|}{r}\right]^2\partial_s\left(\frac{|J|}{r}\right)V_s^2dr & - \partial_s\left(\frac{P_2}{\rho}\right)\int_0^R|J|dr & \\
 & -\sin(\alpha(s))\,g\int_0^R|J|dr & + \frac{\nu}{\rho}\left[|J|\partial_r\left(\left[\frac{|J|}{r}\right]^2V_s\right)\right]_{r=R} & \\
\partial_t\left(\int_0^R r^2V_\theta|J|dr\right) & + \partial_s\left(\int_0^R r^2V_sV_\theta|J|dr\right) & + \partial_\theta\left(\int_0^R r^2V_\theta^2|J|dr\right) & \\
 & = \int_0^R r\left[\frac{|J|}{r}\right]^2\partial_\theta\left(\frac{|J|}{r}\right)V_s^2dr & - \partial_\theta\left(\frac{P_2}{\rho}\right)\int_0^R|J|dr & \\
 & +\frac{\nu}{\rho}\left[|J|\left(\partial_r\left(r^2V_\theta\right)-2rV_\theta\right)\right]_{r=R}. & &
\end{array}$$

Let us define

$$A(R,s,\theta,t)=\int_0^R|J|dr,\quad u(s,\theta,t)=\frac{1}{A}\int_0^R V_s|J|dr,\ \ \omega(s,\theta,t)=\frac{1}{A}\int_o^R V_\theta|J|dr,\ \ (2.16)$$

where

$$A=A(R,s,\theta)=\frac{R^2}{2}-\frac{R^3}{3}\sin(\theta)\alpha'(s)$$

is the radially integrated Jacobian. On the other hand, u and ω are the radially-averaged

axial velocity and angular velocity, respectively. The radially-averaged angular momentum L is defined as

$$L = A_\theta \omega, \quad A_\theta = \frac{\int_o^R r^2 V_\theta |J| dr}{\int_o^R V_\theta |J| dr}.$$

Under the new variables, the model is

$$\begin{aligned}
\partial_t (A) + \partial_s (A\, u) + \partial_\theta (A\, \omega) &= 0, \\
\partial_t (\psi_{s,o} A u) + \partial_s (\psi_{s,1} A u^2) + \partial_\theta (\psi_{s,2} A u \omega) &= -A\partial_s \left(\tfrac{p}{\rho}\right) - gA\sin(\alpha(s)) \\
&\quad + \int_o^R r \left[\tfrac{|J|}{r}\right]^2 \partial_s \left(\tfrac{|J|}{r}\right) V_s^2 dr \\
&\quad + \tfrac{\nu}{\rho} \left(|J| \partial_r \left(\left[\tfrac{|J|}{r}\right]^2 V_s \right) \right) \Big|_o^R , \qquad (2.17) \\
\partial_t (AL) + \partial_s (\psi_{\theta,1} A L u) + \partial_\theta (\psi_{\theta,2} A L \omega) &= -A\partial_\theta \left(\tfrac{p}{\rho}\right) \\
&\quad + \int_o^R r \left[\tfrac{|J|}{r}\right]^2 \partial_\theta \left(\tfrac{|J|}{r}\right) V_s^2 dr \\
&\quad + \tfrac{\nu}{\rho} \left(|J| [\partial_r (r^2 V_\theta) - 2 r V_\theta] \right) \Big|_o^R ,
\end{aligned}$$

where $\psi_{s,o}, \psi_{s,1}, \psi_{s,2}, \psi_{\theta,1}$ and $\psi_{\theta,2}$ are Coriolis terms satisfying

$$\begin{aligned}
\psi_{s,o} A u &= \int_o^R |J| \left[\tfrac{|J|}{r}\right]^2 V_s dr, \\
\psi_{s,1} A u^2 &= \int_o^R |J| \left[\tfrac{|J|}{r}\right]^2 V_s^2 dr, \quad \psi_{\theta,1} A^2 u \omega = \int_o^R |J| r^2 V_\theta V_s dr, \qquad (2.18) \\
\psi_{s,2} A u \omega &= \int_o^R |J| \left[\tfrac{|J|}{r}\right]^2 V_s V_\theta dr, \quad \psi_{\theta,2} A^2 \omega^2 = \int_o^R |J| r^2 V_\theta^2 dr.
\end{aligned}$$

The integral of the Jacobian in the radial direction A is one of our conserved variables. This variable A satisfies that $\int_{s_0}^{s_1} \int_0^{2\pi} A d\theta ds$ is the volume in the corresponding artery's region. In the case of a circular cross section, the integral with respect to θ gives us the cross-sectional area. The balance of axial and angular momenta determines the other two conserved quantities, given by

$$Q_1 = \psi_{s,o} A u, \quad Q_2 = AL, \qquad (2.19)$$

where $\psi_{s,o}$ takes into account the effect of curvature in the artery, and $\psi_{s,o} = 1$ for horizontal vessels. One still needs to determine a profile for the axial and angular velocities V_s and V_θ as functions of r to close the system. For a given profile, the non-dimensional Coriolis terms $\psi_{s,o}, \psi_{s,1}, \psi_{s,2}, \psi_{\theta,1}$ and $\psi_{\theta,2}$ are all explicit functions of A, s and θ. In fact, those parameters are explicit functions of $R\sin(\theta)\alpha'(s)$ for the profiles considered in this work, and are therefore constant parameters for vessels with zero curvature. See section 3.2 for more details.

Transmural pressure

The transmural pressure, which is the pressure difference between the two sides of the artery's wall is denoted by P_2. The elasticity properties of the vessel are determined by a relationship between P_2, the area A and possibly the variables s and θ due to non-uniform properties in the artery (explicit dependence on parameters). That is, we assume that the transmural pressure is an explicit function

$$P_2 = P_2(A, s, \theta).$$

Furthermore, we assume that the transmural pressure vanishes at a given state at rest $A_o = A_o(s, \theta) = \frac{R_o^2}{2} - \frac{R_o^3}{3}\sin(\theta)\alpha'(s)$ with $R_o = R_o(s, \theta)$ such that

$$P_2(A_o(s, \theta), s, \theta) = 0.$$

Some properties such as the hyperbolicity of the system are shown independently of the profiles, and we take equation (2.17) as the most general form of the system. This closes the system since everything is given in terms of the conserved quantities A, Q_1 and Q_2, and s, θ due to the presence of varying parameters.

Conservation form

The model can be written in conservation form. For that end, we need to introduce the following notation. The transmural pressure and other parameters such as the Coriolis terms are explicit functions $q = q(A, s, \theta)$ of A, s and θ. On the other hand, model parameters such as R_o and A_o depend explicitly on (s, θ). We will denote by $\partial_1, \partial_2, \partial_3$

the derivatives with respect to A, s and θ, keeping the other terms fixed. Thus

$$\partial_s(P_2(A(s,\theta,t),s,\theta)) = \partial_1 P_2\, \partial_s A + \partial_2 P_2,$$

$$\partial_\theta(P_2(A(s,\theta,t),s,\theta)) = \partial_1 P_2\, \partial_\theta A + \partial_3 P_2.$$

We distinguish them from ∂_s and ∂_θ, which take into account the variations of the conserved variables with respect to s and θ over time.

In order to get the conservation form, we define the splitting of the transmural pressure as

$$P_2 = \widehat{p} + \overline{p},$$

where

$$\widehat{p}\,(A,s,\theta) = \frac{1}{A}\int_{A_o}^{A} \mathcal{A}\partial_1\left(P_2\left(\mathcal{A},s,\theta\right)\right) d\mathcal{A},$$

which satisfy

$$\begin{aligned} A\partial_s\left(P_2\right) &= \partial_s\left(A\widehat{p}\right) + A\partial_2\overline{p}, \text{ and} \\ A\partial_\theta\left(P_2\right) &= \partial_\theta\left(A\widehat{p}\right) + A\partial_3\overline{p}. \end{aligned}$$

The 2D model for blood flows in arteries with arbitrary cross sections is written as a hyperbolic system of balance as

$$\partial_t \mathbf{U} + \partial_s\, \mathbf{F}\left(\mathbf{U}\right) + \partial_\theta\, \mathbf{G}\left(\mathbf{U}\right) = S\left(\mathbf{U}\right), \tag{2.20}$$

$$\begin{aligned} \mathbf{U} &= \begin{pmatrix} A \\ \psi_{s,o} Au \\ AL \end{pmatrix}, \quad \mathbf{F}\left(\mathbf{U}\right) = \begin{pmatrix} Au \\ \psi_{s,1} Au^2 + \frac{1}{\rho} A\widehat{p} \\ \psi_{\theta,1} AuL \end{pmatrix}, \quad \text{and} \\ \mathbf{G}\left(\mathbf{U}\right) &= \begin{pmatrix} A\omega \\ \psi_{s,2} Au\omega \\ \psi_{\theta,2} AL\omega + \frac{1}{\rho} A\widehat{p} \end{pmatrix} \end{aligned} \tag{2.21}$$

are the vectors of conserved variables and the fluxes in the axial and angular directions, respectively. The vector of source terms is

$$\mathbf{S}(\mathbf{U}) = \begin{pmatrix} 0 \\ -\frac{A}{\rho}\partial_2\overline{p} - A\sin(\alpha(s))\, g & +\int_o^R \frac{|J|}{r}\partial_s\left(\frac{|J|}{r}\right)V_s^2|J|dr \\ & +\frac{\nu}{\rho}\left[|J|\partial_r\left(\left[\frac{|J|}{r}\right]^2 V_s\right)\right]_{r=R} \\ -\frac{A}{\rho}\partial_3\overline{p} + \int_o^R \frac{|J|}{r}\partial_\theta & \left(\frac{|J|}{r}\right)V_s^2|J|dr \\ & +\frac{\nu}{\rho}\left[|J|\partial_r\left(r^2 V_\theta\right) - 2r|J|V_\theta\right]_{r=R} \end{pmatrix}. \tag{2.22}$$

We note that none of the source terms are non-conservative products. The source terms only involve derivatives of the model parameters with respect to the explicit dependance on (s, θ) and no derivates of the solution itself are present. This prevents both theoretical and numerical complications when shockwaves arise. Below we show explicit expressions of the source and Coriolis terms for a particular choice of profiles for the transmural pressure, axial and angular velocities. As we will see, the expressions are very simple in the case of horizontal arteries ($\alpha'(s) = 0$).

Chapter 3

Properties of the model

3.1 Hiperbolicity of the model

The conservation form in equation (2.20) is crucial because it allows us to formulate the Rankine-Hugoniot conditions for weak solutions in the presence of shock-waves. We can apply the theory of weak solutions provided the model is hyperbolic. The hyperbolic properties of system (2.20) can be studied through its quasilinear formulation.

In equation (2.19), we present the conserved variables of the model, as A, $Q_1 = \psi_{s,o} A u$ and $Q_2 = AL$. The flux in the axial and angular direction, in term of the conserved quantities, are given by

$$F(\mathbf{U}) = \begin{pmatrix} \dfrac{Q_1}{\psi_{s,o}} \\ \dfrac{\psi_{s,1} Q_1^2}{\psi_{s,o}^2 A} + \dfrac{1}{\rho} A \widehat{p} \\ \dfrac{\psi_{\theta,1} Q_1 Q_2}{\psi_{s,o} A} \end{pmatrix}, \quad G(\mathbf{U}) = \begin{pmatrix} \dfrac{Q_2}{A_\theta} \\ \dfrac{\psi_{s,2} Q_1 Q_2}{\psi_{s,o} A A_\theta} \\ \dfrac{\psi_{\theta,2} Q_2^2}{A A_\theta} + \dfrac{1}{\rho} A \widehat{p} \end{pmatrix}.$$

The quasilinear formulation, which is given by

$$\partial_t \mathbf{U} + M_s(\mathbf{U}) \partial_s \mathbf{U} + M_\theta(\mathbf{U}) \partial_\theta \mathbf{U} = \tilde{\mathbf{S}}(\mathbf{U}), \tag{3.1}$$

where the coefficient matrix are

$$M_s(\mathbf{U}) = \begin{pmatrix} \partial_1\left(\frac{1}{\psi_{s,o}}\right)Q_1 & \frac{1}{\psi_{s,o}} & 0 \\ \partial_1\left(\frac{1}{\rho}A\widehat{p}\right) + \partial_1\left(\frac{\psi_{s,1}}{\psi_{s,o}^2 A}\right)Q_1^2 & \frac{2\psi_{s,1}Q_1}{\psi_{s,o}^2 A} & 0 \\ \partial_1\left(\frac{\psi_{\theta,1}}{\psi_{s,o}A_\theta}\right)Q_1Q_2 & \frac{\psi_{\theta,1}Q_2}{\psi_{s,o}A_\theta} & \frac{\psi_{\theta,1}Q_1}{\psi_{s,o}A_\theta} \end{pmatrix}, \tag{3.2}$$

and

$$M_\theta(\mathbf{U}) = \begin{pmatrix} \partial_1\left(\frac{1}{\psi_{\theta,o}A}\right)Q_2 & 0 & \frac{1}{A_\theta} \\ \partial_1\left(\frac{\psi_{s,2}}{\psi_{s,o}AA_\theta}\right)Q_1Q_2 & \frac{\psi_{s,2}Q_2}{\psi_{s,o}AA_\theta} & \frac{\psi_{s,2}Q_1}{\psi_{s,o}AA_\theta} \\ \partial_1\left(\frac{1}{\rho}A\widehat{p}\right) + \partial_1\left(\frac{\psi_{\theta,2}}{A_\theta^2}\right)Q_2^2 & 0 & \frac{2\psi_{\theta,2}Q_2}{A_\theta^2} \end{pmatrix}. \tag{3.3}$$

The vector of source terms of the quasi-linear formulation is

$$\tilde{S}(\mathbf{U}) = S(\mathbf{U}) - \begin{pmatrix} \partial_2\left(\frac{1}{\psi_{s,o}}\right)Q_1 + \partial_3\left(\frac{1}{A_\theta}\right)Q_2 \\ \partial_2\left(\frac{1}{\rho}A\widehat{p}\right) + \partial_2\left(\frac{\psi_{s,1}}{\psi_{s,o}^2 A}\right)Q_1^2 + \partial_3\left(\frac{\psi_{s,2}}{\psi_{s,o}AA_\theta}\right)Q_1Q_2 \\ \partial_3\left(\frac{1}{\rho}A\widehat{p}\right) + \partial_2\left(\frac{\psi_{\theta,1}}{\psi_{s,o}A_\theta}\right)Q_1Q_2 + \partial_3\left(\frac{\psi_{\theta,2}}{A_\theta^2}\right)Q_2^2 \end{pmatrix}. \tag{3.4}$$

In terms of A, u, ω and L, the matrices are

$$M_s(\mathbf{U}) = \begin{pmatrix} -\frac{A}{\psi_{s,o}}\partial_1(\psi_{s,o})u & \frac{1}{\psi_{s,o}} & 0 \\ \frac{1}{\rho}\partial_1(A\widehat{p}) - \left(\frac{\psi_{s,1}}{\psi_{s,o}}\right)^2\partial_1\left(\frac{\psi_{s,o}^2 A}{\psi_{s,1}}\right)u^2 & 2\frac{\psi_{s,1}}{\psi_{s,o}}u & 0 \\ -\frac{\psi_{\theta,1}^2}{\psi_{s,o}}\partial_1\left(\frac{\psi_{s,o}A}{\psi_{\theta,1}}\right)uL & \frac{\psi_{\theta,1}}{\psi_{s,o}}L & \psi_{\theta,1}u \end{pmatrix}, \tag{3.5}$$

and

$$M_\theta(\mathbf{U}) = \begin{pmatrix} -\dfrac{A}{A_\theta}\partial_1(A_\theta)\,\omega & 0 & \dfrac{1}{A_\theta} \\ -\dfrac{\psi_{s,2}^2}{\psi_{s,o}A_\theta}\partial_1\left(\dfrac{\psi_{s,o}AA_\theta}{\psi_{s,2}}\right)u\omega & \dfrac{\psi_{s,2}}{\psi_{s,o}}\omega & \dfrac{\psi_{s,2}}{A_\theta}u \\ \dfrac{1}{\rho}\partial_1(A\widehat{p}) - \psi_{\theta,2}^2\partial_1\left(\dfrac{AA_\theta}{\psi_{\theta,2}}\right)\omega^2 & 0 & 2\psi_{\theta,2}\omega \end{pmatrix}. \tag{3.6}$$

The vector of source terms of the quasi-linear formulation is

$$\tilde{S}(\mathbf{U}) = S(\mathbf{U}) + \begin{pmatrix} \dfrac{A}{\psi_{s,o}}\partial_2(\psi_{s,o})\,u + \dfrac{A}{A_\theta}\partial_3(A_\theta)\,\omega \\ -\dfrac{1}{\rho}\partial_2(A\widehat{p}) + \left(\dfrac{\psi_{s,1}}{\psi_{s,o}}\right)^2\partial_2\left(\dfrac{\psi_{s,o}^2A}{\psi_{s,1}}\right)u^2 + \dfrac{\psi_{s,2}^2}{\psi_{s,o}A_\theta}\partial_3\left(\dfrac{\psi_{s,o}AA_\theta}{\psi_{s,2}}\right)u\omega \\ -\dfrac{1}{\rho}\partial_3(A\widehat{p}) + \dfrac{\psi_{\theta,1}^2}{\psi_{s,o}}\partial_2\left(\dfrac{\psi_{s,o}A}{\psi_{\theta,1}}\right)uL + \psi_{\theta,2}^2\partial_3\left(\dfrac{AA_\theta}{\psi_{\theta,2}}\right)\omega^2 \end{pmatrix}. \tag{3.7}$$

The matrices M_s and M_θ have two null entries in one column and their eigenvalues have explicit expressions given by

$$\lambda_o^s = \frac{\psi_{\theta,1}}{\psi_{\theta,o}}u, \quad \lambda_\pm^s = \frac{2\psi_{s,1} - A\partial_1(\psi_{s,o})}{2\psi_{s,o}}u \;\pm\; \sqrt{\frac{\frac{1}{\rho}\partial_1(A\widehat{p})}{\psi_{s,o}} + \Upsilon_1 u^2}, \tag{3.8}$$

for M_s, and

$$\lambda_o^\theta = \frac{\psi_{s,2}}{\psi_{s,o}}\omega, \quad \lambda_\pm^\theta = \frac{2\psi_{\theta,2}A_\theta - A\partial_1(A_\theta)}{2A_\theta}\omega \pm \sqrt{\frac{\frac{1}{\rho}\partial_1(A\widehat{p})}{A_\theta} + \Upsilon_2\omega^2} \tag{3.9}$$

for M_θ, respectively. Here,

$$\begin{aligned} \Upsilon_1 &= \tfrac{1}{\psi_{s,o}^2}\left[\psi_{s,1} - \tfrac{1}{2}A\partial_1(\psi_{s,o})\right]^2 + \tfrac{1}{\psi_{s,o}}\left[A\partial_1(\psi_{s,1}) - \psi_{s,1}\right], \text{ and} \\ \Upsilon_2 &= \tfrac{1}{A_\theta^2}\left[\psi_{\theta,2}A_\theta - \tfrac{1}{2}A\partial_1(A_\theta)\right]^2 + \tfrac{1}{A_\theta}\left[A\partial_1(\psi_{\theta,2}A_\theta) - \psi_{\theta,2}A_\theta\right] \end{aligned} \tag{3.10}$$

are all non-dimensional quantities.

Below we specify the profiles for the axial and angular velocities. For those specific profiles, we show that $\Upsilon_1 = \Upsilon_1(\Gamma)$ and $\Upsilon_2 = \Upsilon_2(\Gamma)$ are explicit rational functions of Γ, where

$$\Gamma = R\sin(\theta)\alpha'(s). \tag{3.11}$$

Such functions satisfy $\Upsilon_1(\Gamma=0)=\dfrac{\psi_{s,1}}{\psi_{s,o}}\left(\dfrac{\psi_{s,1}}{\psi_{s,o}}-1\right)$ and $\Upsilon_2(\Gamma=0)=\left(\psi_{\theta,2}-\dfrac{1}{2}\right)^2$. The special case $\Gamma=0$ corresponds to a horizontal vessel.

Proposition 3.1. *Let us assume that p is strictly increasing with respect A, with positive partial derivative, except possibly at $A=0$ where the vessel collapses. The coefficient matrices M_s and M_θ given by (3.5) and (3.6) have real eigenvalues and a complete set of eigenvectors, subject to the conditions $0<R<\frac{1}{|\alpha'(s)|}$, and $\Upsilon_1,\Upsilon_2\geq 0$.*

The condition $0<R<\frac{1}{|\alpha'(s)|}$ indicates that the artery's radius must not exceed the artery's radius of curvature and it is required for the change of variables to cylindrical coordinates to be valid. This implies that the non-dimensional parameter Γ satisfies $|\Gamma|\leq 1$. For specific profiles used in this paper for the axial and angular velocities, Υ_1 and Υ_2 are in fact non-negative for $\Gamma\in[-1,1]$.

Proof. Under the above hypothesis, and the fact that

$$\partial_1(A\hat{p})=A\partial_1 p\geq 0,$$

the expressions inside the square roots in equations (3.8) and (3.9) are non-negative. As a result, all the eigenvalues are real. The expressions inside the square roots could only vanish if $A=0$ (or equivalently $R=0$). It would also require that $u=0$ or $\omega=0$ if $\Upsilon_1=0$ or $\Upsilon_2=0$ respectively. This could happen for certain parameter choices, specially in horizontal vessels. In any case, the condition $R>0$ is sufficient to guarantee that $\lambda^s_+\neq\lambda^s_-$ and $\lambda^\theta_+\neq\lambda^\theta_-$. However, the eigenvalue λ^s_o may still have multiplicity 2 if it coincides with λ^s_+ or λ^s_-. And the same applies for the matrix M_θ.

In the case when the eigenvalues for M_s are different and writing $M_s=(a_{ij})$, the eigenvectors form a basis and are given by

$$\mathbf{v}^s_o=\begin{pmatrix}0\\0\\1\end{pmatrix},\quad \mathbf{v}^s_\pm=\begin{pmatrix}a_{12}\\ \lambda^s_\pm-a_{11}\\ \frac{(a_{11}-\lambda^s_\pm)a_{32}-a_{12}a_{31}}{a_{33}-\lambda^s_\pm}\end{pmatrix}.$$

If $\lambda_o^s = \lambda_-^s$, the eigenvectors are given by

$$\mathbf{v}_o^s = \begin{pmatrix} 0 \\ 0 \\ 1 \end{pmatrix}, \quad \mathbf{v}_-^s = \begin{pmatrix} a_{12} \\ \lambda_-^s - a_{11} \\ 0 \end{pmatrix}, \quad \mathbf{v}_+^s = \begin{pmatrix} a_{12} \\ \lambda_+^s - a_{11} \\ \frac{\left(a_{11}-\lambda_+^s\right)a_{32}-a_{12}a_{31}}{a_{33}-\lambda_+^s} \end{pmatrix}.$$

Since $\lambda_+^s \neq \lambda_-^s$, one can easily check that the eigenvectors form a complete basis because $a_{12} = \frac{1}{\psi_{s,o}} > 0$. The case $\lambda_o^s = \lambda_+^s$ and the analysis for M_θ are analogous. □

The hyperbolicity of the model requires that $n_s M_s + n_\theta R_o M_\theta$ has real eigenvalues and a complete set of eigenvectors for all $n_s, n_\theta \in \mathbb{R}$ such that $n_s^2 + n_\theta^2 = 1$. Here R_o is a constant in units of length that appears due to the fact that s and θ have different units. For the general case, the matrix $n_s M_s + n_\theta R_o M_\theta$ has not a simple form. However, one can easily analyze the special case of a horizontal vessel ($\alpha'(s) = 0$) and $\omega = 0$. In such case, $\psi_{s,o}, \psi_{s,1}, \psi_{s,2}, \psi_{\theta,1}$ are all constant, and the characteristic polynomial is

$$P(\lambda) = -\lambda^3 + c_2\lambda^2 + c_1\lambda + c_o,$$

where

$$\begin{aligned} c_2 &= (2\psi_{s,1} + \psi_{\theta,1})\, u n_s, \\ c_1 &= \tfrac{1}{\rho}\partial_1(A\hat{p})\left(n_s^2 + \tfrac{R_o^2}{A_\theta} n_\theta^2\right) + \left(-\psi_{s,1} - 2\psi_{s,1}\psi_{\theta,1}\right)\, u^2\, n_s^2, \\ c_o &= \left[-\tfrac{1}{\rho}\partial_1(A\hat{p}) + \psi_{s,1}u^2\right]\psi_{\theta,1}\, n_s^3\, u \\ &\quad + \tfrac{1}{\rho}\partial_1(A\hat{p})\, \tfrac{R_o^2}{A_\theta}(-2\psi_{s,1} + \psi_{s,2})\, n_\theta^2\, u\, n_s. \end{aligned}$$

Using Cardano's approach, we know the characteristic polynomial has three distinct real eigenvalues if

$$
\begin{aligned}
0 \;<\;& -27c_o^2 - 18c_2c_1c_o + 4c_1^3 - 4c_2^3c_o + c_2^2c_1^2 \\
=\;& 4\left(\tfrac{1}{\rho}\partial_1(A\hat{p}) + \psi_{s,1}(\psi_{s,1}-1)u^2\right)\left[\tfrac{1}{\rho}\partial_1(A\hat{p}) + (2\psi_{s,1}\psi_{\theta,1} - \psi_{s,1} - \psi_{\theta,1}^2)u^2\right]^2 n_s^6 \\
&+12\tfrac{\left(\frac{1}{\rho}\partial_1(A\hat{p})\right)^3 R_o^2}{A_\theta} n_s^4 n_\theta^2 \\
&+4\tfrac{\left(\frac{1}{\rho}\partial_1(A\hat{p})\right)^2 R_o^2 u^2}{A_\theta}\left(20\psi_{s,1}^2 + \psi_{\theta,1}(9\psi_{s,2}+5\psi_{\theta,1}) - \psi_{s,1}(6+9\psi_{s,2}+19\psi_{\theta,1})\right) n_s^4 n_\theta^2 \\
&+4\tfrac{\frac{1}{\rho}\partial_1(A\hat{p}) R_o^2 u^4}{A_\theta}\Big[16\psi_{s,1}^4 - \psi_{s,2}\psi_{\theta,1}^3 - 4\psi_{s,1}^3(5+2\psi_{s,2}+4\psi_{\theta,1}) \\
&\qquad +\psi_{s,1}\psi_{\theta,1}\left[3\psi_{s,2}(-3+\psi_{\theta,1}) + (-5+\psi_{\theta,1})\psi_{\theta,1}\right] \\
&\qquad +\psi_{s,1}^2(3+\psi_{\theta,1}(19+2\psi_{\theta,1}) + \psi_{s,2}(9+6\psi_{\theta,1}))\Big] n_s^4 n_\theta^2 \\
&+12\tfrac{\left(\frac{1}{\rho}\partial_1(A\hat{p})\right)^3 R_o^4}{A_\theta^2} n_s^2 n_\theta^4 \\
&+\tfrac{\left(\frac{1}{\rho}\partial_1(A\hat{p})\right)^2 R_o^4}{A_\theta^2} u^2\Big[-32\psi_{s,1}^2 - 27\psi_{s,2}^2 - 18\psi_{s,2}\psi_{\theta,1} + \psi_{\theta,1}^2 \\
&\qquad +4\psi_{s,1}(-3+18\psi_{s,2}+4\psi_{\theta,1})\Big] n_s^2 n_\theta^4 \\
&+4\tfrac{\left(\frac{1}{\rho}\partial_1(A\hat{p})\right)^3 R_o^6}{A_\theta^3} n_\theta^6.
\end{aligned}
$$

A sufficient condition for hyperbolicity is then

$$
\begin{aligned}
&\psi_{s,1} > 1, \\
&20\psi_{s,1}^2 + \psi_{\theta,1}(9\psi_{s,2}+5\psi_{\theta,1}) - \psi_{s,1}(6+9\psi_{s,2}+19\psi_{\theta,1}) > 0, \\
&16\psi_{s,1}^4 - \psi_{s,2}\psi_{\theta,1}^3 - 4\psi_{s,1}^3(5+2\psi_{s,2}+4\psi_{\theta,1}) \\
&\qquad +\psi_{s,1}\psi_{\theta,1}\left[3\psi_{s,2}(-3+\psi_{\theta,1}) + (-5+\psi_{\theta,1})\psi_{\theta,1}\right] \\
&\qquad\qquad +\psi_{s,1}^2(3+\psi_{\theta,1}(19+2\psi_{\theta,1}) + \psi_{s,2}(9+6\psi_{\theta,1})) > 0, \\
&-32\psi_{s,1}^2 - 27\psi_{s,2}^2 - 18\psi_{s,2}\psi_{\theta,1} + \psi_{\theta,1}^2 + 4\psi_{s,1}(-3+18\psi_{s,2}+4\psi_{\theta,1}) > 0.
\end{aligned}
$$

We have verified that such condition is met when we use the specific profiles and parameter values in Section 3.2. Although the hyperbolicity has been proved for the special case of horizontal vessels with vanishing angular velocity, we believe this property is satisfied in a much more general context because Proposition 3.1 shows that each coefficient matrix can be diagonalized.

3.2 Specific profiles of pressure, axial and radial velocities

We present specific profiles for axial and angular velocity, which are linear functions of the radially-axial velocity u and angular velocity ω, respectively. Also, these profiles must catch information about the curvature of the vessel, which is represented by coefficients e_s and e_θ, respectively. Following [9], a Hagen-Poiseuille profile is assumed for the axial velocity:

$$V_s = e_s V_s^\star u, \;\; V_s^\star = \frac{r}{|J|}\left[1 - \left(\frac{r}{R}\right)^{\gamma_s}\right], \tag{3.12}$$

where

$$e_s\left(A, s, \theta\right) = \frac{A}{\int_o^R V_s^\star\left(r, R\right)|J| dr}.$$

This profile vanishes at the artery's wall and it is strongest at the center. The exponent γ_s controls the transition from the center to the walls. Taking $\gamma_s = 9$, we get the effect of a Newtonian fluid [39]. On the other hand, we use a similar profile for the angular velocity,

$$V_\theta = e_\theta V_\theta^\star \omega, \;\; V_\theta^\star = \left[1 - \frac{\gamma_\theta}{\gamma_\theta + 1}\frac{r}{R}\right]\left(\frac{r}{R}\right)^{\gamma_\theta - 1}, \tag{3.13}$$

where

$$e_\theta\left(A, s, \theta\right) = \frac{A}{\int_o^R V_\theta^\star\left(r, R\right)|J| dr}.$$

In the numerical simulations we take $\gamma_\theta = 2$. It satisfies that the linear velocity rV_θ vanishes at the center and $\partial_r(rV_\theta) = 0$ at $r = R$. In terms of the above profiles

$$\begin{aligned}
\psi_{s,o} &= \frac{e_s}{A}\int_o^R \left[\frac{|J|}{r}\right]^2 V_s^\star |J| dr, \\
\psi_{s,1} &= \frac{e_s^2}{A}\int_o^R \left[\frac{|J|}{r}\right]^2 \left(V_s^\star\right)^2 |J| dr, \quad \psi_{\theta,1} = \frac{e_s e_\theta}{A^2}\int_o^R r^2 V_\theta^\star V_s^\star |J| dr, \\
\psi_{s,2} &= \frac{e_s e_\theta}{A}\int_o^R \left[\frac{|J|}{r}\right]^2 V_s^\star V_\theta^\star |J| dr, \quad \psi_{\theta,2} = \frac{e_\theta^2}{A^2}\int_o^R r^2 \left(V_\theta^\star\right)^2 |J| dr,
\end{aligned} \tag{3.14}$$

where it can be found that each one of the above terms are functions of Γ, and, in the case of $\alpha'(s) = 0$, these terms are constants. These gives:

$$
\begin{aligned}
\psi_{s,o} &= 1 - \frac{4(\gamma_s+2)}{3(\gamma_s+3)}\Gamma + \frac{\gamma_s+2}{2(\gamma_s+4)}\Gamma^2, \\
\psi_{s,1} &= \frac{\gamma_s+2}{\gamma_s+1}\left[1-\frac{2}{3}\Gamma\right]\left[1-\frac{2(2\gamma_s+2)(\gamma_s+2)}{3(2\gamma_s+3)(\gamma_s+3)}\Gamma\right], \\
\psi_{s,2} &= \frac{\gamma_s+2}{\gamma_s}\left[1-\frac{(\gamma_\theta+2)(2\gamma_\theta+\gamma_s+2)}{2(\gamma_\theta+\gamma_s+1)(\gamma_\theta+\gamma_s+2)}\right]\frac{1-\frac{2}{3}\Gamma}{1-\frac{2\gamma_\theta+3}{2(\gamma_\theta+3)}\Gamma}\times \\
&\quad\left[1-\frac{2(\gamma_\theta+\gamma_s+1)(3\gamma_\theta^2+2\gamma_\theta\gamma_s+11\gamma_\theta+3\gamma_s+9)}{(\gamma_\theta+3)(\gamma_\theta+\gamma_s+3)(3\gamma_\theta+2\gamma_s+4)}\Gamma\right. \\
&\quad\left.+\frac{(\gamma_\theta+2)(\gamma_\theta+\gamma_s+1)(\gamma_\theta+\gamma_s+2)(3\gamma_\theta^2+2\gamma_s\gamma_\theta+15\gamma_\theta+4\gamma_s+16)}{(\gamma_\theta+3)(\gamma_\theta+4)(\gamma_\theta+\gamma_s+3)(\gamma_\theta+\gamma_s+4)(3\gamma_\theta+2\gamma_s+4)}\Gamma^2\right], \\
\psi_{\theta,1} &= \frac{\gamma_s+2}{\gamma_s}\left[1-\frac{(\gamma_\theta+3)(\gamma_\theta+4)(2\gamma_\theta+\gamma_s+4)}{2(\gamma_\theta+2)(\gamma_\theta+\gamma_s+3)(\gamma_\theta+\gamma_s+4)}\right]\frac{1-\frac{2}{3}\Gamma}{1-\frac{(\gamma_\theta+3)(2\gamma_\theta+5)}{2(\gamma_\theta+2)(\gamma_\theta+5)}\Gamma}, \\
\psi_{\theta,2} &= \frac{(\gamma_\theta+3)(\gamma_\theta+4)(5\gamma_\theta+6)}{16(\gamma_\theta+2)(2\gamma_\theta+3)}\frac{\left[1-\frac{2}{3}\Gamma\right]\left[1-\frac{2\left(5\gamma_\theta^2+14\gamma_\theta+10\right)}{(2\gamma_\theta+5)(5\gamma_\theta+6)}\Gamma\right]}{\left[1-\frac{2\gamma_\theta+3}{2(\gamma_\theta+3)}\Gamma\right]\left[1-\frac{(\gamma_\theta+3)(2\gamma_\theta+5)}{2(\gamma_\theta+2)(\gamma_\theta+5)}\Gamma\right]}, \text{ and} \\
A_\theta &= \frac{(\gamma_\theta+2)^2}{(\gamma_\theta+3)(\gamma_\theta+4)}\left[\frac{1-\frac{(\gamma_\theta+3)(2\gamma_\theta+5)}{2(\gamma_\theta+2)(\gamma_\theta+5)}\Gamma}{1-\frac{2\gamma_\theta+3}{2(\gamma_\theta+3)}\Gamma}\right]R^2.
\end{aligned}
$$

Transmural pressure

The elasticity properties of the vessel can be described by the dependence of the transmural pressure on the radius A, and it must be an increasing function of A in order to maintain hyperbolicity. As discussed in [40], the elastic properties of the vessel's wall may be impacted by the contraction of surrounding muscles or pathologies such as aneurysms, among others. Although deriving an explicit dependence $p = p(A, s, \theta)$ is complicated, valid expressions can be found in [4, 13, 40]. Following [9], the numerical tests use the following expression of the transmural pressure,

$$
p(A, s, \theta) = G_o(s, \theta)\left(\left(\frac{A}{A_o(s, \theta)}\right)^{\beta/2} - 1\right), \tag{3.15}
$$

where A_o as defined above. This includes the effect of the wall's thickness and the stress-strain response. Here, G_o is the elasticity coefficient. Shear stress is ignored, and it is

assumed that the transmural pressure of the fluid is the only force exerted on the vessel's wall. The parameter $\beta > 1$ corresponds to a non-linear stress-strain response. The value $\beta = 2$ provides a good approximation for experimental data [9]. The dependence of G_o and R_o on s and θ allows us to explore the change in elasticity properties of the vessel's wall, or to explore the influence of vessel tapering on shock formation [8, 10]. Here we adopt the parametrization of the elasticity parameter in terms of the Young's modulus and wall's thickness given by [41]

$$G_o(s,\theta) = \frac{4}{3} E_Y \frac{h_d}{r_d}, \tag{3.16}$$

where E_Y is the Young's modulus, $r_d(s,\theta)$ is the radius at diastolic pressure and $h_d(s,\theta)$ is the wall's thickness. In this thesis, we take that $r_d = R_o$ and h_d will keep constant.

The explicit expressions of the transmural pressure decomposition that appears in model (2.20) that correspond to the transmural pressure relation (3.15) are

$$\widehat{p}(A,s,\theta) = \frac{\beta}{\beta+2} p - \frac{\beta}{\beta+2} G_o \frac{A_o - A}{A}, \quad \overline{p}(A,s,\theta) = \frac{2}{\beta+2} p + \frac{\beta}{\beta+2} G_o \frac{A_o - A}{A}.$$

The transmural pressure terms in the source can be written in terms of the derivative of the parameters as

$$\partial_2 \overline{p} = \frac{\overline{p}}{G_o} \partial_2 G_o - \frac{\widehat{p}}{A_o} \partial_2 A_o, \quad \partial_3 \overline{p} = \frac{\overline{p}}{G_o} \partial_3 G_o - \frac{\widehat{p}}{A_o} \partial_3 A_o. \tag{3.17}$$

Furthermore, the needed expressions to compute the source terms are given by

$$\begin{aligned}
\int_o^R r \partial_s \left(\frac{|J|}{r}\right) \left[\frac{|J|}{r} V_s\right]^2 dr &= -\frac{8(\gamma_s+2)^2}{(\gamma_s+3)(2\gamma_s+3)} \left(\frac{A}{R}\right)^2 R \sin(\theta)\, \alpha''(s)\, u^2, \\
\int_o^R r \partial_\theta \left(\frac{|J|}{r}\right) \left[\frac{|J|}{r} V_s\right]^2 dr &= -\frac{8(\gamma_s+2)^2}{(\gamma_s+3)(2\gamma_s+3)} \left(\frac{A}{R}\right)^2 R \cos(\theta)\, \alpha'(s)\, u^2, \\
\left[|J| \partial_r \left(\left[\frac{|J|}{r}\right]^2 V_s\right)\right]_{r=R} &= -(\gamma_s+2)[1-\Gamma]^2 \frac{2A}{R^2} u, \\
\left[|J| \partial_r \left(r^2 V_\theta\right) - 2|J| r V_\theta\right]_{r=R} &= -\frac{(\gamma_\theta+1)(\gamma_\theta+3)(\gamma_\theta+4)}{4(\gamma_\theta+2)} \\
&\quad \times \left[\frac{1-\Gamma}{1 - \frac{(\gamma_\theta+3)(2\gamma_\theta+5)}{2(\gamma_\theta+2)(\gamma_\theta+5)}\Gamma}\right] \frac{2A}{R^2} L.
\end{aligned}$$

3.3 Steady-States

Although transient flows provide a more complete description of pulsatile blood flows, it has been shown that under certain circumstances, steady states (i.e., those independent of time) provide enough information for clinical assessment. In [42], a 5% difference was found in the time-averaged wall shear stress between transient and steady states. There are, however, other clinical situations where transient flows are necessary for an accurate description of the pulsatile blood flow. In any case, our numerical scheme is constructed to accurately compute transient flows, including those near steady states.

The 2D model (2.20) admits a large class of steady states that arise when a delicate balance between flux gradients and source terms occurs. Here, we characterize those steady states for vessels with zero curvature ($\alpha'(s) = 0$, or $\alpha = \alpha_o$ constant), zero viscosity ($\nu = 0$) for fluids moving in the axial direction ($\omega = 0$). In those cases, equation (2.17) becomes

$$\begin{aligned} \partial_s (A\,u) &= 0, \\ \partial_s (\psi_{s,1} A u^2) &= -A\partial_s \left(\tfrac{p}{\rho}\right) - gA\sin(\alpha_o), \\ 0 &= -A\partial_\theta \left(\tfrac{p}{\rho}\right), \end{aligned}$$

which implies $Au = Q_1(\theta)$ is independent of s. The parameter $\psi_{s,1}$ is constant in vessels with zero curvature with the profiles in Section 3.2. The second equation for the balance of momentum can be re-written as

$$A\partial_s \left(\psi_{s,1}\frac{u^2}{2} + \frac{p}{\rho} + g z_o(s)\right) = 0,$$

where

$$z_o(s) = \sin(\alpha_o)\; s$$

is the artery's elevation above a reference height. As a result, smooth steady states for vessels with zero curvature, zero viscosity and vanishing angular velocity satisfy that the discharge $Q_1 = Au$ and the energy $E = \psi_{s,1}\frac{u^2}{2} + \frac{p}{\rho} + g z_o(s)$ are independent of s, whereas the transmural pressure p is independent of θ. In particular, one could have constant

discharge and energy. The steady states at rest correspond to the special case

$$u = 0, \omega = 0, R = R_o(s, \theta), \alpha(s) = 0. \tag{3.18}$$

Below we construct a numerical scheme that respects those steady states at rest for arteries with arbitrary cross sections.

Chapter 4

Central-upwind Numerical Scheme

In this work, we use a central-upwind scheme, whose semi-discrete formulation is obtained after integrating equation (2.20) over each cell $\mathcal{C}_{j,k} := \left[s_{j-\frac{1}{2}}, s_{j+\frac{1}{2}}\right] \times \left[\theta_{k-\frac{1}{2}}, \theta_{k+\frac{1}{2}}\right]$, with center at (s_j, θ_k), $s_{j\pm\frac{1}{2}} = s_j \pm \Delta s/2$ and $\theta_{k\pm\frac{1}{2}} = \theta_k \pm \Delta\theta/2$. The cell averages $\overline{\mathbf{U}}_{j,k}(t)$

$$\overline{\mathbf{U}}_{j,k}(t) = \frac{1}{\Delta s \Delta\theta} \int_{\mathcal{C}_{j,k}} \int \mathbf{U}(s,\theta,t)\, ds d\theta$$

are approximated by solving the semi-discrete formulation

$$\frac{d}{dt}\overline{\mathbf{U}}_{j,k}(t) = -\frac{\mathbf{H}^F_{j+\frac{1}{2},k}(t) - \mathbf{H}^F_{j-\frac{1}{2},k}(t)}{\Delta s} - \frac{\mathbf{H}^G_{j,k+\frac{1}{2}}(t) - \mathbf{H}^G_{j,k-\frac{1}{2}}(t)}{\Delta\theta} + \overline{\mathbf{S}}_{j,k}(t), \tag{4.1}$$

with numerical fluxes $\mathbf{H}^F$ and $\mathbf{H}^G$ given by [43],

$$\begin{aligned}
\mathbf{H}^F_{j+\frac{1}{2},k}(t) &= \frac{a^+_{j+\frac{1}{2},k} F\left(\mathbf{U}^-_{j+\frac{1}{2},k}\right) - a^-_{j+\frac{1}{2},k} F\left(\mathbf{U}^+_{j+\frac{1}{2},k}\right)}{a^+_{j+\frac{1}{2},k} - a^-_{j+\frac{1}{2},k}} \\
&\quad + \frac{a^+_{j+\frac{1}{2},k} a^-_{j+\frac{1}{2},k}}{a^+_{j+\frac{1}{2},k} - a^-_{j+\frac{1}{2},k}} \left[\mathbf{U}^+_{j+\frac{1}{2},k} - \mathbf{U}^-_{j+\frac{1}{2},k}\right] \\
\mathbf{H}^G_{j,k+\frac{1}{2}}(t) &= \frac{b^+_{j,k+\frac{1}{2}} G\left(\mathbf{U}^-_{j,k+\frac{1}{2}}\right) - b^-_{j,k+\frac{1}{2}} G\left(\mathbf{U}^+_{j,k+\frac{1}{2}}\right)}{b^+_{j,k+\frac{1}{2}} - b^-_{j,k+\frac{1}{2}}} \\
&\quad + \frac{b^+_{j,k+\frac{1}{2}} b^-_{j,k+\frac{1}{2}}}{b^+_{j,k+\frac{1}{2}} - b^-_{j,k+\frac{1}{2}}} \left[\mathbf{U}^+_{j,k+\frac{1}{2}} - \mathbf{U}^-_{j,k+\frac{1}{2}}\right].
\end{aligned} \tag{4.2}$$

For any quantity of interest $q = q(\mathbf{U})$, the corresponding interface values are obtained via the following piece-wise linear reconstruction

$$\begin{aligned} q^{-}_{j+\frac{1}{2},k} &= \overline{q}_{j,k} + \tfrac{\Delta s}{2}\left(q_s\right)_{j,k}, \\ q^{+}_{j-\frac{1}{2},k} &= \overline{q}_{j,k} - \tfrac{\Delta s}{2}\left(q_s\right)_{j,k}, \\ q^{-}_{j,k+\frac{1}{2}} &= \overline{q}_{j,k} + \tfrac{\Delta \theta}{2}\left(q_\theta\right)_{j,k}, \\ q^{+}_{j,k-\frac{1}{2}} &= \overline{q}_{j,k} - \tfrac{\Delta \theta}{2}\left(q_\theta\right)_{j,k}, \end{aligned} \tag{4.3}$$

where the slopes $\left(q_s\right)_{j,k}$ and $\left(q_\theta\right)_{j,k}$ are calculated using the generalized minmod limiter

$$\left(q_s\right)_{j,k} = \text{minmod}\left(\phi\frac{\overline{q}_{j,k}-\overline{q}_{j-1,k}}{\Delta s}, \frac{\overline{q}_{j+1,k}-\overline{q}_{j-1,k}}{2\Delta s}, \phi\frac{\overline{q}_{j+1,k}-\overline{q}_{j,k}}{\Delta s}\right), \tag{4.4}$$

$$\left(q_\theta\right)_{j,k} = \text{minmod}\left(\phi\frac{\overline{q}_{j,k}-\overline{q}_{j,k-1}}{\Delta \theta}, \frac{\overline{q}_{j,k+1}-\overline{q}_{j,k-1}}{2\Delta \theta}, \phi\frac{\overline{q}_{j,k+1}-\overline{q}_{j,k}}{\Delta \theta}\right), \tag{4.5}$$

where

$$\text{minmod}\left(z_1, z_2, \cdots\right) = \begin{cases} \min_j\{z_j\} & \text{if} \quad z_j > 0 \ \forall j, \\ \max_j\{z_j\} & \text{if} \quad z_j < 0 \ \forall j, \\ 0 & \text{otherwise.} \end{cases}$$

Here, the parameter ϕ is used to control the amount of numerical viscosity present in the resulting scheme.

The discretization of the averaged source terms

$$\overline{\mathbf{S}}_{j,k}\left(t\right) = \frac{1}{\Delta s \Delta \theta}\int_{\mathcal{C}_{j,k}}\int S\left(\mathbf{U}\right)\left(s,\theta,t\right) ds d\theta$$

is carried out so as to satisfy the well-balanced property. This is explained in more detail in Section 4.1.

The one-sided local speeds in the $s-$ and $\theta-$directions, $a^{\pm}_{j+\frac{1}{2},k}$ and $b^{\pm}_{j,k+\frac{1}{2}}$, are obtained

from the largest and the smallest eigenvalues of the Jacobians $\frac{\partial F(\mathbf{U})}{\partial \mathbf{U}}$ and $\frac{\partial G(\mathbf{U})}{\partial \mathbf{U}}$, respectively. Using (3.8) and (3.9), it follows that:

$$a^+_{j+\frac{1}{2},k} = \max\Big\{ \left(\lambda^s_o\right)^-_{j+\frac{1}{2},k}, \left(\lambda^s_+\right)^-_{j+\frac{1}{2},k}, u^-_{j+\frac{1}{2},k}, \left(\lambda^s_o\right)^+_{j+\frac{1}{2},k}, \left(\lambda^s_+\right)^+_{j+\frac{1}{2},k}, u^+_{j+\frac{1}{2},k}, 0\Big\}, \tag{4.6a}$$

$$a^-_{j+\frac{1}{2},k} = \min\Big\{ \left(\lambda^s_o\right)^-_{j+\frac{1}{2},k}, \left(\lambda^s_-\right)^-_{j+\frac{1}{2},k}, u^-_{j+\frac{1}{2},k}, \left(\lambda^s_o\right)^+_{j+\frac{1}{2},k}, \left(\lambda^s_-\right)^+_{j+\frac{1}{2},k}, u^+_{j+\frac{1}{2},k}, 0\Big\}, \tag{4.6b}$$

$$b^+_{j,k+\frac{1}{2}} = \max\Big\{ \left(\lambda^\theta_o\right)^-_{j,k+\frac{1}{2}}, \left(\lambda^\theta_+\right)^-_{j,k+\frac{1}{2}}, \omega^-_{j,k+\frac{1}{2}}, \left(\lambda^\theta_o\right)^+_{j,k+\frac{1}{2}}, \left(\lambda^\theta_+\right)^+_{j,k+\frac{1}{2}}, \omega^+_{j,k+\frac{1}{2}}, 0\Big\}, \tag{4.6c}$$

$$b^-_{j,k+\frac{1}{2}} = \min\Big\{ \left(\lambda^\theta_o\right)^-_{j,k+\frac{1}{2}}, \left(\lambda^\theta_-\right)^-_{j,k+\frac{1}{2}}, \omega^-_{j,k+\frac{1}{2}}, \left(\lambda^\theta_o\right)^+_{j,k+\frac{1}{2}}, \left(\lambda^\theta_-\right)^+_{j,k+\frac{1}{2}}, \omega^+_{j,k+\frac{1}{2}}, 0\Big\}. \tag{4.6d}$$

The time integration of the ODE system (4.1) is done using the second-order strong stability preserving Runge-Kutta scheme [44]

$$\mathbf{U}^{(1)} = \overline{\mathbf{U}}(t) + \Delta t\, \mathbf{C}[\overline{\mathbf{U}}(t)], \tag{4.7a}$$

$$\mathbf{U}^{(2)} = \frac{1}{2}\overline{\mathbf{U}} + \frac{1}{2}\left(\mathbf{U}^{(1)} + \Delta t\, \mathbf{C}[\mathbf{U}^{(1)}]\right), \tag{4.7b}$$

$$\overline{\mathbf{U}}(t+\Delta t) := \mathbf{U}^{(2)}, \tag{4.7c}$$

with

$$\mathbf{C}[\mathbf{U}(t)]_{j,k} = -\frac{\mathbf{H}^F_{j+\frac{1}{2},k}(t) - \mathbf{H}^F_{j-\frac{1}{2},k}(t)}{\Delta s} - \frac{\mathbf{H}^G_{j,k+\frac{1}{2}}(t) - \mathbf{H}^G_{j,k-\frac{1}{2}}(t)}{\Delta \theta} + \overline{\mathbf{S}}_{j,k}(t).$$

The Courant-Friedrichs-Lewy (CFL) condition that determines the time step Δt is

$$\Delta t \le \frac{1}{4}\min\left\{\frac{\Delta s}{a}, \frac{\Delta \theta}{b}\right\}, \tag{4.8}$$

where

$$a = \max_{j,k}\left\{\max\left(a^+_{j+\frac{1}{2},k}, -a^-_{j+\frac{1}{2},k}\right)\right\}, \text{ and } b = \max_{j,k}\left\{\max\left(b^+_{j,k+\frac{1}{2}}, -b^-_{j,k+\frac{1}{2}}\right)\right\}.$$

4.1 Steady states at rest and positivity of the cross-sectional radius

The quantities of interest to compute the numerical flux in equation (4.2) are reconstructed at the interfaces via equation (4.3) using the minmod limiter given by equation (4.4). However, the reconstructed values need to be implemented carefully in order to guarantee the well-balance property. For that end, we assume that the radius at rest $R_o(s,\theta)$ is defined at the interfaces $\left(s_j, \theta_{k\pm\frac{1}{2}}\right)$ and at $\left(s_{j\pm\frac{1}{2}}, \theta_k\right)$, and we define it at the center of each cell as

$$R_{o,j,k} := \frac{1}{4}\left[R_o\left(s_{j-\frac{1}{2}}, \theta_k\right) + R_o\left(s_{j+\frac{1}{2}}, \theta_k\right) + R_o\left(s_j, \theta_{k-\frac{1}{2}}\right) + R_o\left(s_j, \theta_{k+\frac{1}{2}}\right)\right]. \tag{4.9}$$

On the other hand, the angle $\alpha(s)$ is defined at each interface point $s_{j+\frac{1}{2}}$. The derivatives both at the center of each cell and at the interfaces are approximated via centered differences as

$$\begin{aligned} &\alpha'(s_j) \approx \frac{\alpha\left(s_{j+\frac{1}{2}}\right)-\alpha\left(s_{j-\frac{1}{2}}\right)}{\Delta s}, \quad \alpha(s_j) \approx \frac{\alpha\left(s_{j+\frac{1}{2}}\right)+\alpha\left(s_{j-\frac{1}{2}}\right)}{2}, \\ &\alpha'(s_{j+\frac{1}{2}}) \approx \frac{\alpha(s_{j+1})-\alpha(s_j)}{\Delta s}, \end{aligned} \tag{4.10}$$

which gives

$$\begin{aligned} A_{o,j+\frac{1}{2},k} &= \frac{R^2_{o,j+\frac{1}{2},k}}{2} - \frac{R^3_{o,j+\frac{1}{2},k}}{3}\sin(\theta_k)\alpha'\left(s_{j+\frac{1}{2}}\right), \\ A_{o,j,k+\frac{1}{2}} &= \frac{R^2_{o,j,k+\frac{1}{2}}}{2} - \frac{R^3_{o,j,k+\frac{1}{2}}}{3}\sin(\theta_{k+\frac{1}{2}})\alpha'\left(s_j\right). \end{aligned}$$

In order to reconstruct A at the interfaces, we define $\mathcal{A} = A/A_o$ and reconstruct the values $\mathcal{A}^{\pm}_{j+\frac{1}{2},k}$ and $\mathcal{A}^{\pm}_{j,k+\frac{1}{2}}$ at the cell interfaces using equation (4.3). The cross-sectional area at the cell interfaces are then given by

$$A^{\pm}_{j+\frac{1}{2},k} = \mathcal{A}^{\pm}_{j+\frac{1}{2},k} A_{o,j+\frac{1}{2},k}, \quad A^{\pm}_{j,k+\frac{1}{2}} = \mathcal{A}^{\pm}_{j,k+\frac{1}{2}} A_{o,j,k+\frac{1}{2}}. \tag{4.11}$$

This way, if $R = R_o$ or equivalently $A = A_o$ at the center of each cell (as it occurs for steady states at rest), the same equality holds at the cell interfaces. Once the variable A

is reconstructed, this gives the reconstruction for R by inverting it in terms of A. One also obtains the reconstruction for the parameter Γ via the relation

$$\Gamma^{\pm}_{j+\frac{1}{2},k} = R^{\pm}_{j+\frac{1}{2},k}\sin(\theta_k)^{\pm}\alpha'(s_{j+\frac{1}{2}}), \quad \Gamma^{\pm}_{j,k+\frac{1}{2}} = R^{\pm}_{j,k+\frac{1}{2}}\sin(\theta_{k+\frac{1}{2}})\alpha'(s_j). \tag{4.12}$$

This immediately defines all the parameter functions $\psi_{s,o}, \psi_{s,1}, \psi_{s,2}, \psi_{\theta,1}, \psi_{\theta,2}$ and A_θ at the interfaces. The conserved variables $Q_1 = \psi_{s,o}Au$ and $Q_2 = AL$ are reconstructed directly via equation (4.3), from which we can recover the reconstructed values for $u = \frac{Q_1}{\psi_{s,o}A}$, $L = \frac{Q_2}{A}$, and $\omega = \frac{L}{A_\theta}$.

The source terms in equation (2.22) do not involve derivatives of the solution itself and one can use the cell averages to discretize them. The partial derivatives $\partial_2\bar{p}$ and $\partial_3\bar{p}$ are with respect to the explicit dependance of the fixed parameters involved in the definition of the transmural pressure. For instance, the transmural pressure p given by equation (3.15) involves the radius at rest $R_o(s,\theta)$ and the parameter $G_o(s,\theta)$. The parameter $G_o(s,\theta)$ is defined at the interfaces $\left(s_j, \theta_{k\pm\frac{1}{2}}\right)$ and $\left(s_{j\pm\frac{1}{2}}, \theta_k\right)$, and we define it at the center of each cell as

$$G_{o,j,k} := \frac{1}{4}\left[G_o\left(s_{j-\frac{1}{2}}, \theta_k\right) + G_o\left(s_{j+\frac{1}{2}}, \theta_k\right) + G_o\left(s_j, \theta_{k-\frac{1}{2}}\right) + G_o\left(s_j, \theta_{k+\frac{1}{2}}\right)\right]. \tag{4.13}$$

The terms $\partial_2\bar{p}$ and $\partial_3\bar{p}$ are given explicitly by equation (3.17). In that case, one only needs partial derivatives of G_o and A_o which are approximated as

$$\begin{aligned}
\partial_2 G_o(s_j,\theta_k) &\approx \tfrac{G_o(s_{j+\frac{1}{2},k}) - G_o(s_{j-\frac{1}{2},k})}{\Delta s}, \\
\partial_3 G_o(s_j,\theta_k) &\approx \tfrac{G_o(s_{j,k+\frac{1}{2}}) - G_o(s_{j,k-\frac{1}{2}})}{\Delta\theta},
\end{aligned} \tag{4.14}$$

$$\begin{aligned}
\partial_2 A_o(s_j,\theta_k) &\approx \tfrac{A_o(s_{j+\frac{1}{2},k}) - A_o(s_{j-\frac{1}{2},k})}{\Delta s}, \\
\partial_3 A_o(s_j,\theta_k) &\approx \tfrac{A_o(s_{j,k+\frac{1}{2}}) - A_o(s_{j,k-\frac{1}{2}})}{\Delta\theta}.
\end{aligned} \tag{4.15}$$

In a steady state at rest given by equation (3.18), the reconstructed values of u and ω are zero, and the equality $R = R_o$ holds at the interfaces. As a result, all the numerical

fluxes $\mathbf{H}^F_{j+\frac{1}{2},k}, \mathbf{H}^G_{j,k+\frac{1}{2}}$ and the source terms $\overline{\mathbf{S}}_{j,k}$ vanish. We have proved the following proposition.

Proposition 4.1. *Consider system* (2.20), (2.21) *and* (2.22) *with transmural pressure given by* (3.15). *Then, the numerical scheme* (4.2)-(4.8) *with the discretizations given by* (4.9)-(4.15) *is well-balanced, i.e.,* $\overline{\mathbf{U}}(t+\Delta t) = \overline{\mathbf{U}}(t)$ *for steady states at rest.*

The following proposition shows that the CFL condition (4.8) guarantees the positivity of A when the solution is computed with the Runge-Kutta method (4.7) and a slight modification is applied to the reconstruction at the interfaces. This is particularly important in situations where the cross section is small. This is not a relevant case from the medical point of view. However, we present it here for the sake of completeness and it would be useful for applications involving collapsed tubes.

Since we have reconstructed $\mathcal{A} = A/A_o$ at the interfaces,

$$\overline{A}_{j,k} = \frac{1}{4}\left[A^+_{j-\frac{1}{2},k} + A^-_{j+\frac{1}{2},k} + A^-_{j,k+\frac{1}{2}} + A^+_{j,k-\frac{1}{2}}\right] \tag{4.16}$$

does not necessarily hold unless A_o is constant. In the cases where one decides to implement the positivity-preserving property, a modification in the reconstruction must be implemented. Namely,

$$\mathcal{A}^-_{j+\frac{1}{2},k} = \overline{\mathcal{A}}_{j,k} + \frac{\Delta s}{2}\left(\mathcal{A}_s\right)_{j,k} \tag{4.17a}$$

$$A^-_{j+\frac{1}{2},k} = \min\left(\max\{\mathcal{A}^-_{j+\frac{1}{2},k}A_{o,j+\frac{1}{2},k}, A_{th}\}, 2\bar{A}_{j,k}\right) \tag{4.17b}$$

$$A^+_{j-\frac{1}{2},k} = 2\bar{A}_{j,k} - A^-_{j+\frac{1}{2},k} \tag{4.17c}$$

with the analogous procedure for $A^\pm_{j,k\pm\frac{1}{2}}$. Here A_{th} is a threshold value needed to maintain positivity in the reconstruction of the interface values. The threshold value can be chosen empirically. This has been done in different contexts and it has shown to be useful in achieving the positivity-preserving property. See for instance [45], where a scheme with this property was derived for the shallow water equations. The threshold will be used only when the corresponding variable (cross sectional area in our case) is small and there is a risk of getting negative unphysical values. Despite the fact that the threshold is

obtained empirically, it does not affect the performance of the numerical scheme and the alternative of not using it could result in unphysical situations. In this work, we did not include numerical tests where a threshold is needed but it could be used in a future work.

Proposition 4.2. *Consider the scheme with the reconstruction algorithm described in section 4.1. If the cell averages* $\overline{A}_{j,k}(t)$ *are such that*

$$\overline{A}_{j,k}(t) \geq 0 \quad \forall \; j,k,$$

then the cell averages $\overline{A}_{j,k}(t+\Delta t)$ *computed with the Runge-Kutta method (4.7) for all* j,k*, under the CFL limitation (4.8), will yield*

$$\overline{A}_{j,k}(t+\Delta t) \geq 0 \quad \forall \; j,k,$$

Proof. Since our Runge-Kutta numerical scheme can be written as a convex combination of Euler steps, one only needs to prove it for just one forward Euler step. The first component in equation (4.1) can be written as

$$\begin{aligned}\overline{A}_{j,k}(t+\Delta t) &= \overline{A}_{j,k}(t) - \tfrac{\Delta t}{\Delta s}\left[\left(\mathbf{H}^F_{j+\frac{1}{2},k}\right)^{(1)} - \left(\mathbf{H}^F_{j-\frac{1}{2},k}\right)^{(1)}\right] \\ &\quad - \tfrac{\Delta t}{\Delta \theta}\left[\left(\mathbf{H}^G_{j,k+\frac{1}{2}}\right)^{(1)} - \left(\mathbf{H}^G_{j,k-\frac{1}{2}}\right)^{(1)}\right].\end{aligned}$$

Using (4.2), we can rewrite it as

$$\begin{aligned}\overline{A}_{j,k}(t+\Delta t) &= \left[\frac{1}{4} - \frac{\Delta t}{\Delta s}a^+_{j+\frac{1}{2},k}\frac{u^-_{j+\frac{1}{2},k} - a^-_{j+\frac{1}{2},k}}{a^+_{j+\frac{1}{2},k} - a^-_{j+\frac{1}{2},k}}\right]A^-_{j+\frac{1}{2},k} + \left[\frac{1}{4} + \frac{\Delta t}{\Delta s}a^-_{j-\frac{1}{2},k}\frac{a^+_{j-\frac{1}{2},k} - u^+_{j-\frac{1}{2},k}}{a^+_{j-\frac{1}{2},k} - a^-_{j-\frac{1}{2},k}}\right]A^+_{j-\frac{1}{2},k} \\ &\quad + \left[\frac{1}{4} - \frac{\Delta t}{\Delta \theta}b^+_{j,k+\frac{1}{2}}\frac{\omega^-_{j,k+\frac{1}{2}} - b^-_{j,k+\frac{1}{2}}}{b^+_{j,k+\frac{1}{2}} - b^-_{j,k+\frac{1}{2}}}\right]A^-_{j,k+\frac{1}{2}} + \left[\frac{1}{4} + \frac{\Delta t}{\Delta \theta}b^-_{j,k-\frac{1}{2}}\frac{b^+_{j,k-\frac{1}{2}} - \omega^+_{j,k-\frac{1}{2}}}{b^+_{j,k-\frac{1}{2}} - b^-_{j,k-\frac{1}{2}}}\right]A^+_{j,k-\frac{1}{2}} \\ &\quad - \frac{\Delta t}{\Delta s}a^-_{j+\frac{1}{2},k}\frac{a^+_{j+\frac{1}{2},k} - u^+_{j+\frac{1}{2},k}}{a^+_{j+\frac{1}{2},k} - a^-_{j+\frac{1}{2},k}}A^+_{j+\frac{1}{2},k} + \frac{\Delta t}{\Delta s}a^+_{j-\frac{1}{2},k}\frac{u^-_{j-\frac{1}{2},k} - a^-_{j-\frac{1}{2},k}}{a^+_{j-\frac{1}{2},k} - a^-_{j-\frac{1}{2},k}}A^-_{j-\frac{1}{2},k} \\ &\quad - \frac{\Delta t}{\Delta \theta}b^-_{j,k+\frac{1}{2}}\frac{b^+_{j,k+\frac{1}{2}} - \omega^+_{j,k+\frac{1}{2}}}{b^+_{j,k+\frac{1}{2}} - b^-_{j,k+\frac{1}{2}}}A^+_{j,k+\frac{1}{2}} + \frac{\Delta t}{\Delta \theta}b^+_{j,k-\frac{1}{2}}\frac{\omega^-_{j,k-\frac{1}{2}} - b^-_{j,k-\frac{1}{2}}}{b^+_{j,k-\frac{1}{2}} - b^-_{j,k-\frac{1}{2}}}A^-_{j,k-\frac{1}{2}} \\ &\quad + \overline{A}_{j,k} - \frac{1}{4}\left[A^+_{j-\frac{1}{2},k} + A^-_{j+\frac{1}{2},k} + A^-_{j,k+\frac{1}{2}} + A^+_{j,k-\frac{1}{2}}\right].\end{aligned}$$

The first four terms in the above equation will be non negative under the CFL restriction (4.8). Also, since $a^-_{j+\frac{1}{2},k} \leq 0$, $b^-_{j,k+\frac{1}{2}} \leq 0$, $a^+_{j-\frac{1}{2},k} \geq 0$ and $b^+_{j,k-\frac{1}{2}} \geq 0$, the following four terms in the above equation are also non negative, which concludes the proof.

□

Chapter 5

Numerical Experiments

Different numerical experiments are presented to show the merits of the numerical scheme and the dynamics of the flow given by the model derived in this work. One can analyze situations where vessels exhibit non-uniform elasticity properties and the corresponding effect on the dynamics of the flow.

The velocity field in 3D views of the artery is computed as follows. First, we need to compute the curvature radius, which is given by

$$R_c = \frac{(R^2 + R_\theta^2)^{\frac{3}{2}}}{R^2 + 2R_\theta^2 - RR_{\theta\theta}} = \frac{R\left(1 + \left(\frac{R_\theta}{R}\right)^2\right)^{\frac{3}{2}}}{1 + 2\left(\frac{R_\theta}{R}\right)^2 - \frac{R_{\theta\theta}}{R}},$$

and we also define

$$R_\theta = \partial_\theta R, \quad R_{\theta\theta} = \partial^2_{\theta\theta} R.$$

The total velocity at each point

$$\Big(x(s,\theta), y(s,\theta), z(s,\theta)\Big) =$$

$$\Big(- R\sin\left(\alpha\left(s\right)\right)\sin\left(\theta\right) + x_o\left(s\right) \ , \ R\cos\left(\theta\right) \ , \ R\cos\left(\alpha\left(s\right)\right)\sin\left(\theta\right) + z_o\left(s\right)\Big)$$

is given by

$$\mathbf{V}\left(s,\theta\right) = u\mathbf{J}_s + \frac{R_c}{\sqrt{R^2 + R_\theta^2}} U_{Tang}\left(\mathbf{J}_\theta + \frac{R_\theta}{R}\mathbf{J}_r\right), \tag{5.1}$$

where

$$U_{Tang} = \frac{1}{A}\int_o^R rV_\theta |J| dr = \frac{e_\theta}{A}\left(\int_o^R rV_\theta^\star |J| dr\right)\omega. \tag{5.2}$$

For convenience and easy of notation, we define the strain $\mathcal{R} = R/R_o$ at the center of each cell.

In all cases, we apply periodic boundary conditions in θ. The boundary conditions in the axial directions are specified in each numerical test. Also, the parameters used for these numerical experiments are: blood density $\rho = 1050$ kg m^{-3}, blood viscosity $\nu = 4$ cP, $\beta = 2$, $\gamma_s = 9$, $\gamma_\theta = 2$, Young modulus $E_Y = 400$ kPa and $h_d = 0.5$ mm. Finally, we take $r_d = R_o$.

5.1 Horizontal vessel with tapering: evolution of perturbation

In this first numerical test, we consider the simple case of a horizontal vessel ($\alpha(s) = 0$) with tapering. That is, A_o is given by

$$A_o(s,\theta) = A_o^\star(1 - sT_p), \quad R_o(s,\theta) = \sqrt{2A_o(s,\theta)},$$

where $T_p = 0.005$ cm^{-1} is the tapering factor and $A_o^\star = (0.82 \text{ cm})^2$. The initial vessel's radius consist of a perturbation from a steady state. The perturbation is located in the middle of the artery. Specifically, the center is at $s^\star = 25$ cm and $\theta^\star = \frac{\pi}{4}$ rad. The initial radius is then given by

$$R(0,s,\theta) = \mathcal{R}(0,s,\theta)\, R_o(s,\theta), \text{ where}$$

$$\mathcal{R}(0,s,\theta) = \begin{cases} 1 & \text{if} \quad \frac{d(s,\theta)}{R_o(s^\star,\theta^\star)} > 1, \\ 1 + \frac{1}{5}\sin\left(\left[1 - \frac{d(s,\theta)}{R_o(s^\star,\theta^\star)}\right]\frac{\pi}{2}\right) & \text{if} \quad \frac{d(s,\theta)}{R_o(s^\star,\theta^\star)} \leq 1, \end{cases}$$

and

$$d(s,\theta) = \sqrt{\frac{1}{4}\left[x(s^\star,\theta^\star) - x(s,\theta)\right]^2 + \left[y(s^\star,\theta^\star) - y(s,\theta)\right]^2 + \left[z(s^\star,\theta^\star) - z(s,\theta)\right]^2}.$$

Neumann boundary conditions are imposed at both ends $(s = 0, s_L)$ with $s_L = 50$ cm.

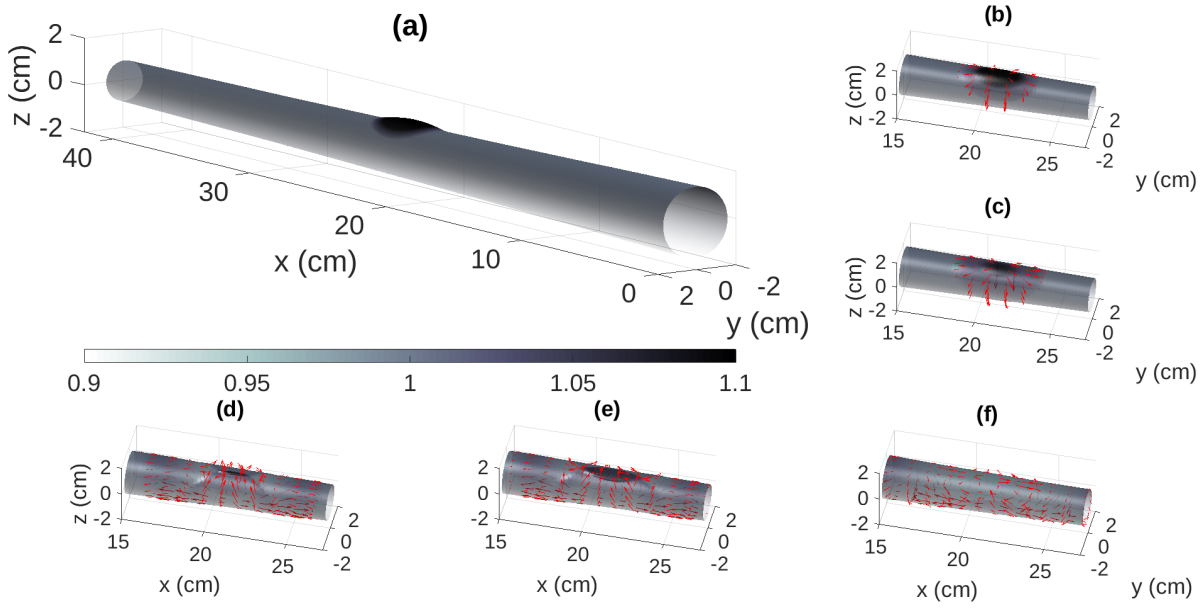

FIGURE 5.1: A 3D view of the vessel. The arrows near the wall indicate the velocity field given by equation (5.1). The color bar indicates the strain at time t ($\mathcal{R}(t\,; s, \theta)$). The initial conditions, which consists of a radius perturbation near $s^\star = 25$ cm and $\theta^\star = \pi/4$ rad is shown in (a), where the entire artery is visualized. The rest of the panels show a section 15 cm $\leq s \leq$ 35 cm where the perturbation evolves at times $t = 0.0005$ s (b), $t = 0.001$ s (c), $t = 0.0045$ s (d), $t = 0.005$ s (e) and $t = 0.1$ s (f). The arrows indicate the 3D velocity field given by equation (5.1).

In this first numerical test, the initial conditions consist of a radius perturbation from a steady state. That is, the transmural pressure is zero everywhere in the artery, except in an area near $(s^\star, \theta^\star)$ where the radius is above the steady state one and the transmural pressure becomes positive. Figure 5.1 shows a 3D view of the artery with the above initial conditions in panel (a). This generates a displacement that consist of a radial expansion at early times, and it can be observed in panels (b) and (c). The color bar indicates the ratio of the vessel radius at time t and its initial value $(R(t\,; s, \theta)/R_o(s, \theta))$, which can help us identify the evolution of the perturbation. The initial perturbation covers only a partial side of the artery's wall and the displacement goes in both the axial and angular directions. At later times in panels (d) and (e), the displacement has already reached the

Segment	Length cm	Left radius cm	Right radius cm
I	7.0357	1.52	1.39
II	0.8	1.39	1.37
III	0.9	1.37	1.35
IV	6.4737	1.35	1.23
V	15.2	1.23	0.99
VI	1.8	0.99	0.97
VII	0.7	0.97	0.962
VIII	0.7	0.962	0.955
IX	4.3	0.955	0.907
X	4.3	0.907	0.86

TABLE 5.1: Description of aorta's geometry and dimensions. The segments, their lengths, left and right radii are shown in the first four columns. Such values were obtained from [41, Table IV].

opposite side of the wall and it has come back to the initial location by periodicity in the angular direction. The last panel (f) shows the solution at time $t = 0.1$ s where the displacement has already propagated in the axial direction outside the visualized region. As a result, the artery has recovered its initial unperturbed steady state.

5.2 Aorta vessel with discharge

The previous case showed that the model and the numerical scheme produces good results for perturbations to steady states in horizontal vessels. For the rest of the numerical tests, we will consider geometries similar to an idealized aorta without branches.

Let $R_o^\star(s)$ be the piecewise linear function of s obtained according to the radius at diastolic pressure shown in [41, Table IV], which we present in table 5.1 for the convenience of the reader. The initial conditions for the artery's geometry is described by cross sections given by

$$R_o(s,\theta) = R_o^\star(s)\, h(\theta),$$

where $h(\theta)$ is a function that determines the type of cross section that we may have. We note that we obtain circular cross sections when $h(\theta)$ is constant. As it is reported in [46], however, we may observe cross sections that have an elliptical-like shape in the

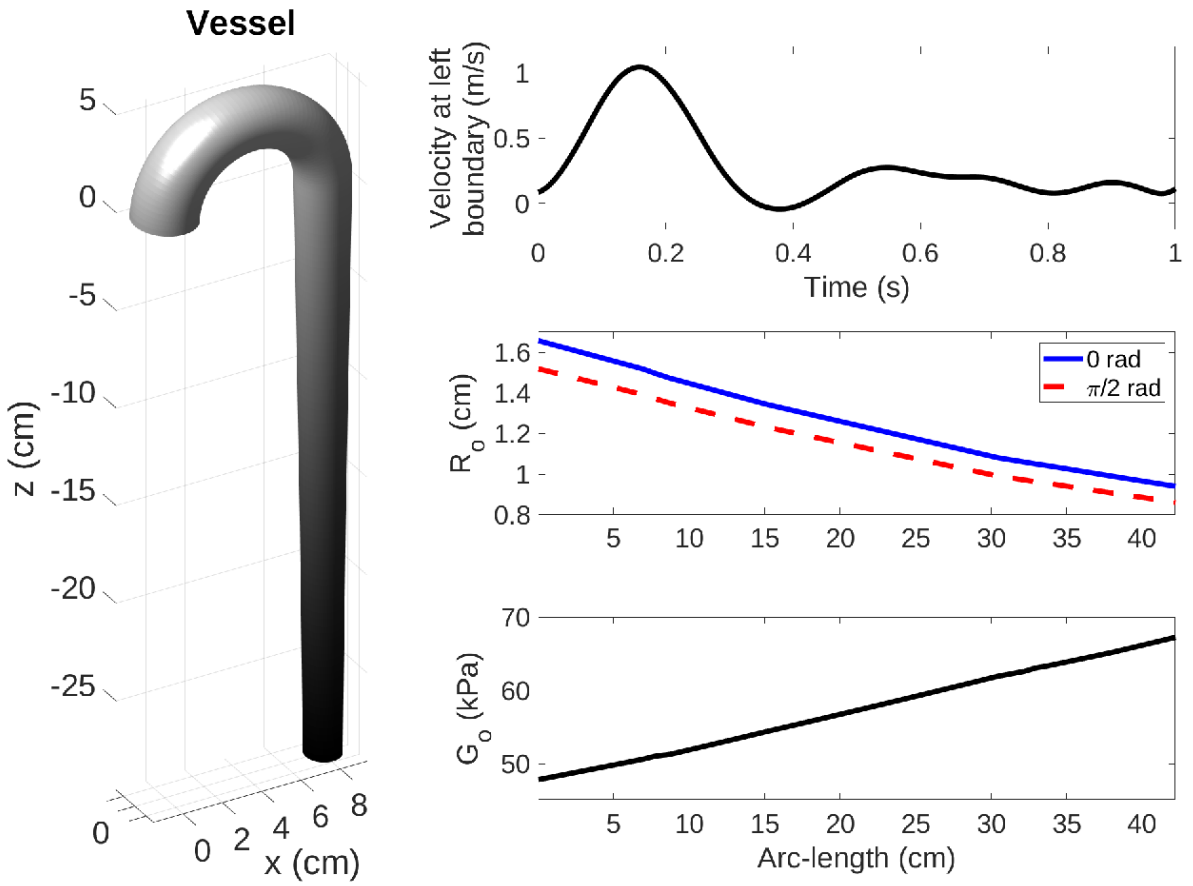

FIGURE 5.2: Blood flow simulation passing through the full aorta. Left panel: 3D view of the aorta. Top right: Velocity at the left boundary in a cardiac cycle as a function of time. Middle right: Profile of R_o as a function of arc-length s for different angles. Bottom right: Profile of G_o as function of arc-length s.

aorta. We then choose

$$h(\theta) = \sqrt{\frac{1 - \xi^2 \sin(\theta)^2}{1 - \xi^2}},$$

where ξ is the eccentricity and $\xi \in [0, 1)$. Graphs of R_o as a function of axial position s for different values of θ are displayed in the middle right panel of Figure 5.2 .

The parameter $G_o^\star(s)$ is given by equation (3.16). A graph of G_o is displayed in the bottom right panel of Figure 5.2. As an approximation to the aorta's curvature, the

angle $\alpha\,(s)$ is given by

$$\alpha\,(s) = \begin{cases} \left[1 - \frac{s}{12.63\ \text{cm}}\right] \frac{\pi}{2} & \text{if} \quad 0 \leq s \leq 12.63\ \text{cm}, \\ \\ -\frac{\pi}{2} & \text{if} \quad s > 12.63\ \text{cm}. \end{cases}$$

That is, the vessel is straight up at the upstream boundary $\alpha(0\ \text{cm}) = \pi/2$ and points down at $s = 12.63$ cm, where $\alpha(12.63\ \text{cm}) = -\pi/2$. Figure 5.2 (left panel) shows a 3D view of the tapered vessel at time $t = 0$ s. Here, we use 200 grid points in the axial direction and 180 grid points in the angular direction. The initial condition is given by $A = A_o$, $u = 0$ and $L = 0$ in a tilted vessel with elliptical geometric shape ($\xi = 0.4$), which would have corresponded to a steady state if the vessel was horizontal.

At the left boundary ($s = 0$), we impose a velocity that corresponds to a cardiac cycle (to be specified below) and Dirichlet boundary conditions for the radius $R = R_o$ and $\omega = 0$. The discharge at the left boundary breaks the balance and induces a moving state. Neumann boundary conditions are imposed at the right boundary. The time series for the velocity at the left boundary was obtained from [10], and it was approximated using the first 15 elements of its Fourier decomposition. Initially, the velocity at the left boundary increases up to speeds above 1 ms^{-1}. A graph of the inlet velocity as a function of time can be found in the top right panel of Figure 5.2 .

In Figure 5.3, we show the evolution of four variables, radius R, axial velocity u, pressure p and tangential velocity U_{Tang}, over 2 seconds at $s = 21.10$ cm. Here, the vessel's radius R is increased due to the influence of the inlet velocity given by the cardiac cycle. On the hand, the transmural pressure reaches its maximum of approximately 7.1 kPa near $t = 0.2$ seconds, followed by a decay. Here, the transmural pressure profile is similar for each θ. In the top right panel we observe the evolution of the axial velocity. Since the initial condition is $u = 0$, the profile starts with an increment to 0.61 ms^{-1}, followed by a decay to -0.1 ms^{-1}, and by an increment to 0.44 ms^{-1} reached at 0.52 s. After this time, the profiles given by different θ values diverge from each other. At $\theta = \pi/2$ rad the velocity reached a maximum of approximately 0.69 ms^{-1} at $t = 0.70$ seconds, while the

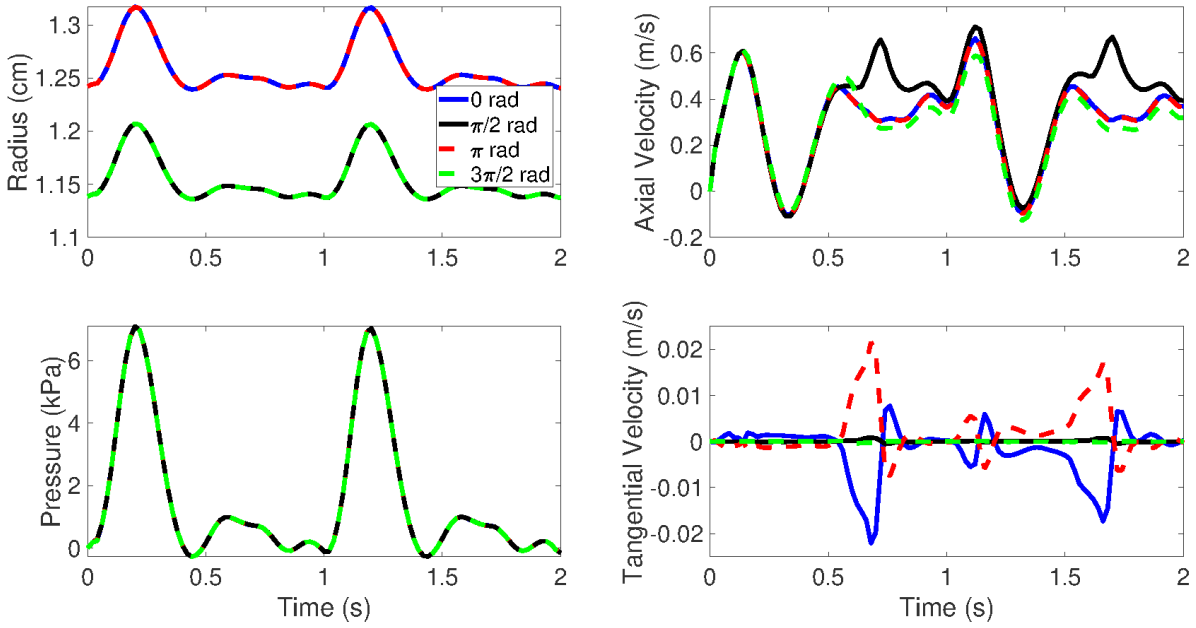

FIGURE 5.3: Profiles as a function of time at $s = 21.10$ cm. Top left: Radius R at different angles. Top right: Axial velocity u. Bottom left: Pressure p. Bottom right: Tangential velocity U_{Tang}.

other profiles show a decay to 0.31 ms^{-1} at the same time. After that, the profiles evolve in a quasi-periodic way.

Finally, the tangential velocity profiles are shown in the bottom right panel of Figure 5.3. Here, we observe that the value is much lower than the axial velocity. One can observe that the tangential velocities are much weaker at angles $\theta = \pi/2$ and $\theta = 3\pi/2$ rad, while the other two ($\theta = 0$ and $\theta = \pi$ rad) are approximately opposite in sign.

5.3 Idealized aorta vessel with a bulge

Non-uniform elasticity properties in a vessel may be caused by diseases such as stenosis and aneurysms. In this numerical test, we analyze possible changes in the flow dynamics when the parameters G_o and R_o are non-uniform in a localized regions in the artery's wall. In particular, G_o is reduced at $(s = s^\star = 21 \text{ cm}, \theta = \theta^\star = 3\pi/2)$ and R_o is increased near that point, when compared to the previous case. Such changes in the parameters

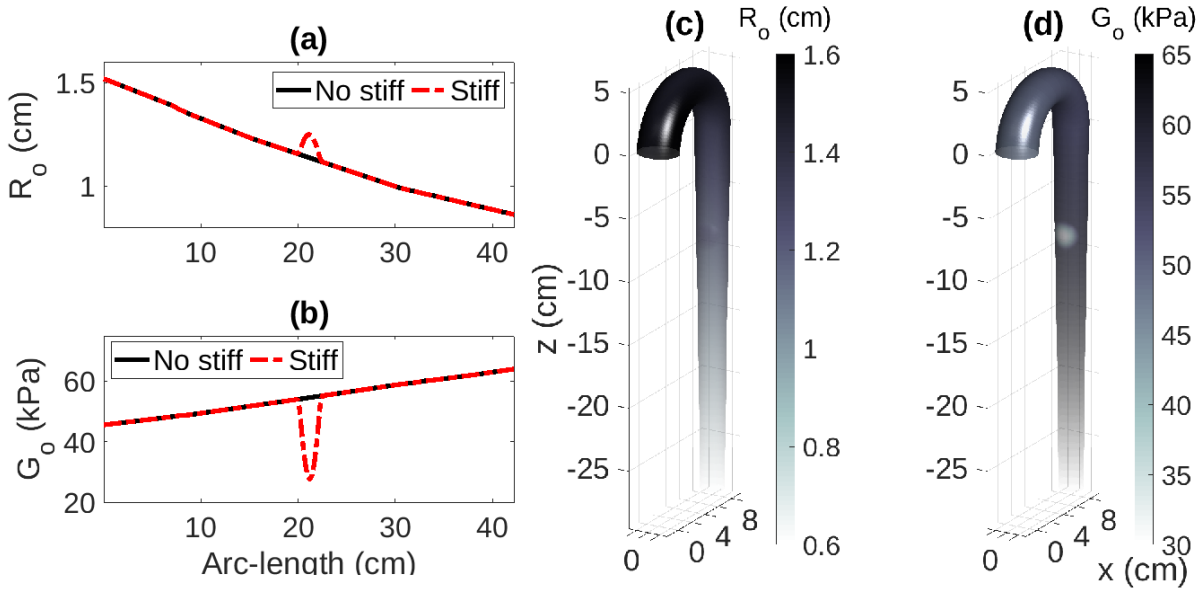

FIGURE 5.4: Parameters for an artery with a bulge in a localized region where the wall is less rigid. In black solid line, profiles of G_o (panel (a)) and R_o (panel (b)) at $\theta = 3\pi/2$ rad are shown, while the red dotted lines correspond to the base case with no bulging. The profiles are given by equations (5.3) and (5.4). Panel (c): 3D visualization of an idealized aorta where the color bar denotes G_o values. Panel (d): same a in middle panel with R_o values in the color bar.

are aimed at simulating an artery with a bulge in a localized region where the artery is also less rigid.

The parameters G_o and R_o are given by

$$G_o(s,\theta) = \begin{cases} G_o^\star(s) & \text{if} \quad d(s,\theta) > h(\theta) R_o^\star(s), \\ \left[1 - \frac{1}{2}\sin\left(\left[1 - \frac{d(s,\theta)}{h(\theta)R_o^\star(s)}\right]\frac{\pi}{2}\right)\right] G_o^\star(s) & \text{if} \quad d(s,\theta) \leq h(\theta) R_o^\star(s), \end{cases} \tag{5.3}$$

and

$$R_o(s,\theta) = \begin{cases} h(\theta)\, R_o^\star(s) & \text{if} \quad d(s,\theta) > h(\theta)\, R_o^\star(s), \\ \left[1 + \frac{1}{5}\sin\left(\left[1 - \frac{d(s,\theta)}{h(\theta) R_o^\star(s)}\right]\frac{\pi}{2}\right)\right] h(\theta)\, R_o^\star(s) & \text{if} \quad d(s,\theta) \leq h(\theta)\, R_o^\star(s), \end{cases} \tag{5.4}$$

where

$$d(s,\theta) = \sqrt{\frac{1}{4}\left[x(s^\star,\theta^\star) - x(s,\theta)\right]^2 + \left[y(s^\star,\theta^\star) - y(s,\theta)\right]^2 + \left[z(s^\star,\theta^\star) - z(s,\theta)\right]^2}.$$

A graph of the parameters at $\theta = 3\pi/2$ rad as a function of s is shown in panels (a) and (b) in Figure 5.4 . A 3D visualization of the aorta using R_o (c) and G_o (d) in the color bar are displayed to localize the region where the elasticity properties of the artery vary.

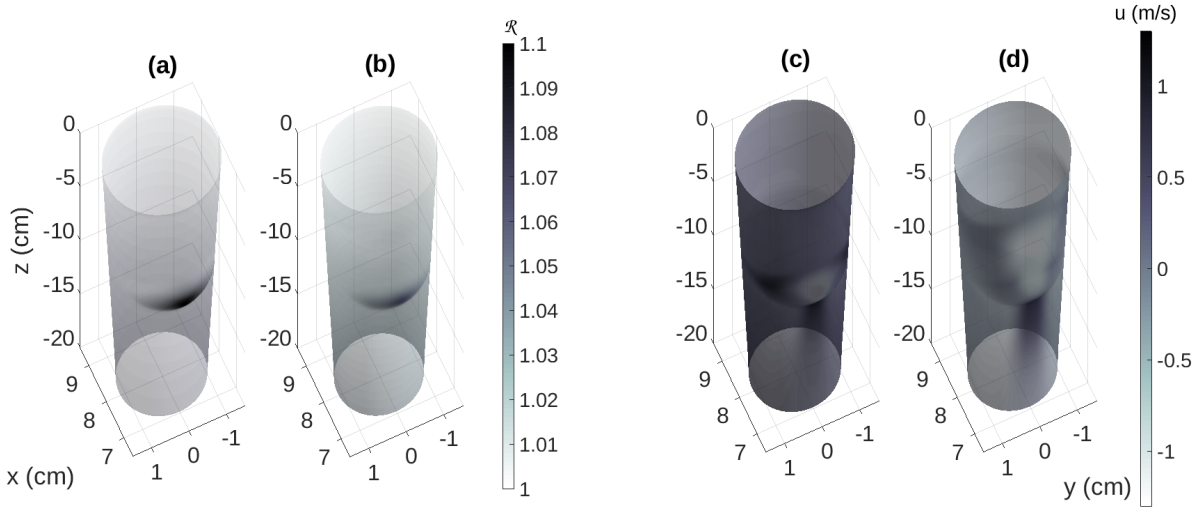

FIGURE 5.5: Panels (a) and (b): 3D view of the artery with color bar computed based on $\mathcal{R} = R/R_o$ at times $t = 0.2$ s and $t = 0.3$ s respectively. Panels (c) and (d): Same as in (a) and (b) with a color bar computed based on u.

As initial conditions, we set

$$R(0,s,\theta) = R_o(s,\theta), \quad u(0,s,\theta) = 0 \quad \text{and} \quad L(0,s,\theta) = 0.$$

Figure 5.5 shows the effect of the bulge with non-uniform elasticity parameters in the flow dynamics. For instance, panels (a) and (b) shows a 3D view of the artery near the bulge where the color bar indicates the ratio R/R_o at times $t = 0.2$ s and $t = 0.3$ s respectively. Such ratio indicates how much the artery's radius has been deformed from the initial conditions. One can observe a stronger deviation from the initial conditions (about 10%) near the bulge at $t = 0.2$ s, when compared to the rest of the artery. Such deviation is reduced at $t = 0.3$ s. On the other hand, a color bar computed based on the axial velocity is displayed in panels (c) and (d). We observe a negative displacement in the upper side of the bulge and a positive displacement in the lower side of the bulge at $t = 0.3$ s. However, the axial velocity becomes positive everywhere at later times (not shown) due to gravity and the fluid discharge in the upstream boundary.

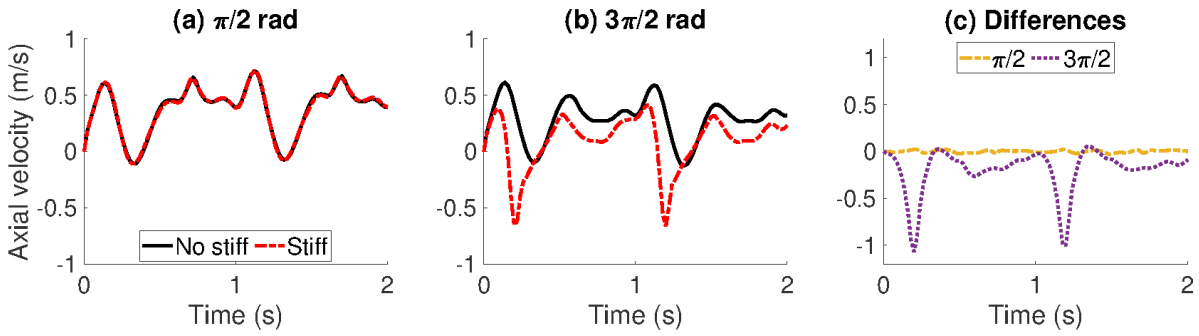

FIGURE 5.6: Axial velocity profiles as a function of time at $s = 21$ cm. Panel (a): Profiles at $\theta = \pi/2$ rad. Panel (b): Profiles at $\theta = 3\pi/2$ rad. Panel (c): Profile differences for $\theta = \pi/2$ rad (ocher dashed line) and $\theta = 3\pi/2$ rad (purple dotted line).

Figure 5.6 exhibits a quantification of the observations discussed in Figure 5.5. Specifically, the axial velocity as a function of time at $s = s^\star$, $\theta = \pi/2$ and $\theta = 3\pi/2$ rad are displayed in panels (a) and (b) respectively. For comparison, we include a graph corresponding to the base case in Section 5.2 . The bulge is at $\theta = 3\pi/2$ rad (panel (b)), where the velocity is decreasing near it. The differences could be up to about 1 ms^{-1}, as we see it in panel (c). Panel (a) shows the axial velocities experienced by the fluid on the opposite side of the wall, where the impact of the bulge does not seem to be significant in the time window considered here.

5.4 Vortex-like structure in aorta vessel with a bulge

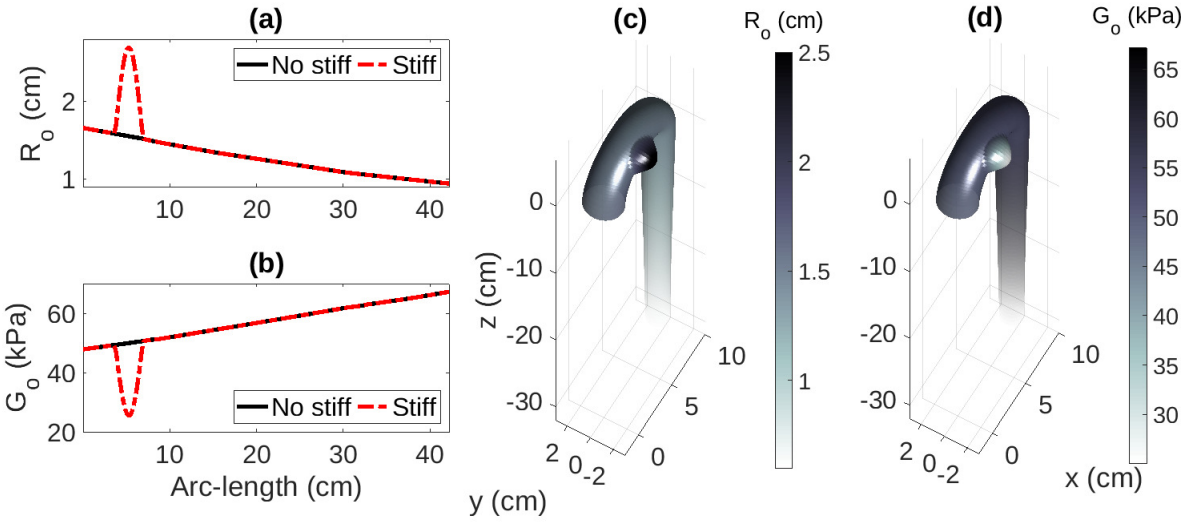

FIGURE 5.7: Parameters R_o and G_o given by equations (5.5) and (5.6) as a function of s at $\theta = \pi$ rad are shown in panels (a) and (b) respectively (red dotted lines). The black solid lines correspond to the base case in Section 5.2. Panel (c): 3D view with color bar denoting R_o. Panel (d): same as in (c) with G_o values in the color bar.

In this numerical example, we consider a situation where the G_o parameter has a negative perturbation in a localized lateral section of the artery near the upstream boundary and R_o is also increased in the same sector, as specified below (see Figure 5.7). This situation is associated with an idealized thoracic aortic aneurysm [47], where the artery's wall is less rigid in a localized zone. The two parameters G_o and R_o are given by

$$G_o(s,\theta) = \begin{cases} G_o^\star(s) & \text{if} \quad d(s,\theta) > h(\theta) R_o^\star(s), \\ \left[1 - \frac{1}{2}\sin\left(\left[1 - \frac{d(s,\theta)}{h(\theta)R_o^\star(s)}\right]\frac{\pi}{2}\right)\right] G_o^\star(s) & \text{if} \quad d(s,\theta) \leq h(\theta) R_o^\star(s), \end{cases} \tag{5.5}$$

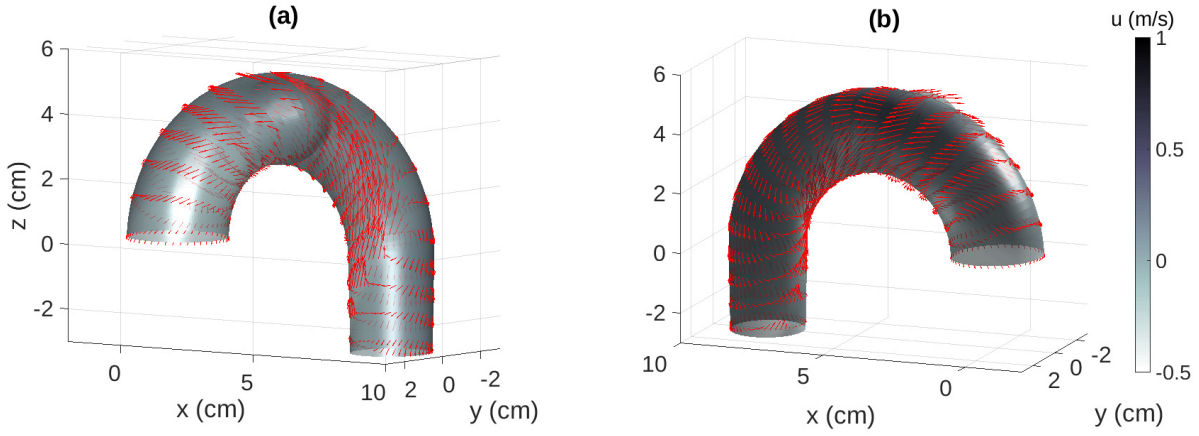

FIGURE 5.8: Circulation pattern in an idealized aorta vessel with a bulge. Three dimensional views of the artery with the velocity field at $t = 0.2$ s (a) and $t = 0.4$ s (b) are shown where the parameters G_o and R_o are given by equations (5.5) and (5.6). The arrows indicate the 3D velocity field given by equation (5.1).

and

$$R_o(s,\theta) = \begin{cases} h(\theta) R_o^\star(s) & \text{if} \quad d(s,\theta) > h(\theta) R_o^\star(s), \\ \left[1 + \frac{3}{4}\sin\left(\left[1 - \frac{d(s,\theta)}{h(\theta)R_o^\star(s)}\right]\frac{\pi}{2}\right)\right] h(\theta) R_o^\star(s) & \text{if} \quad d(s,\theta) \leq h(\theta) R_o^\star(s), \end{cases} \tag{5.6}$$

where

$$d(s,\theta) = \sqrt{[x(s^\star,\theta^\star) - x(s,\theta)]^2 + [y(s^\star,\theta^\star) - y(s,\theta)]^2 + [z(s^\star,\theta^\star) - z(s,\theta)]^2},$$

$$s^\star = 5 \text{ cm}, \theta^\star = \pi \text{ rad}.$$

A 3D view of the artery at time $t = 0.4$ s can be found in panels (a) and (b) of Figure 5.8, respectively. In each panel, the velocity field is shown to analyze the change in the dynamic. The color bar shows the axial velocity contours. Panel (a) shows a section of the artery near the perturbation. The bulge induces a vortex-like structure at time $t = 0.4$ s in the lower region of the bulge but the flow moves in the downstream direction after it passes that region where the artery is less rigid, that is shown at panel (b).

The circulation pattern has been extended to a larger region, where the axial velocity is negative in the right side of the artery ($\pi/2 \leq \theta \leq 3\pi/2$) near the bulge and positive on the opposite side. Circulation patterns can be found on other simulations. See for instance [48].

5.5 A discussion about parameter regimes and the numerical results

The numerical tests presented above focused on evaluating different aspects of the model and the scheme. Regarding the model, the main purpose is to show the higher level of details that it can provide when angular variations are allowed in a non-uniform general cross section. One-dimensional models with axi-symmetry have shown to be in good agreement with 3D models and with experimental data, as explained for instance in [19]. The 2D model derived in this work reduces to the 1D counterpart when the vessel's cross sections are axi-symmetric. Even in that case, they can be in good agreement with experimental data. The interested reader can see more details about such comparisons in [19]. Despite the fact that in our setting we are only focusing in idealized aorta simulations, the profiles for the pressure as a function of time is similar to the profiles obtained in this work. The additional attributes in this model that accounts for variations in the angular directions were obtained by assuming very reasonable assumptions. It allows us to obtain more detailed features of the vessel when the cross sections are irregular. It can provide useful information in situations where experimental data could not be available.

Finding detailed experimental data is not an easy task. When available, one can use such data to estimate the model's parameters. For instance, a relation between stress and strain in a dog's artery is shown in [49]. In this context, the strain $\mathcal{R}$ is the ratio between the midwall radius $R = \dfrac{R_E + R_I}{2}$ and the non-stressed midwall radius R_o, $\mathcal{R} = \dfrac{R}{R_o}$. The outer ($R_E$) and inner ($R_I$) vessel's radii be defined as $R_E = R + \frac{1}{2}h_d, \quad R_I = R - \frac{1}{2}h_d,$

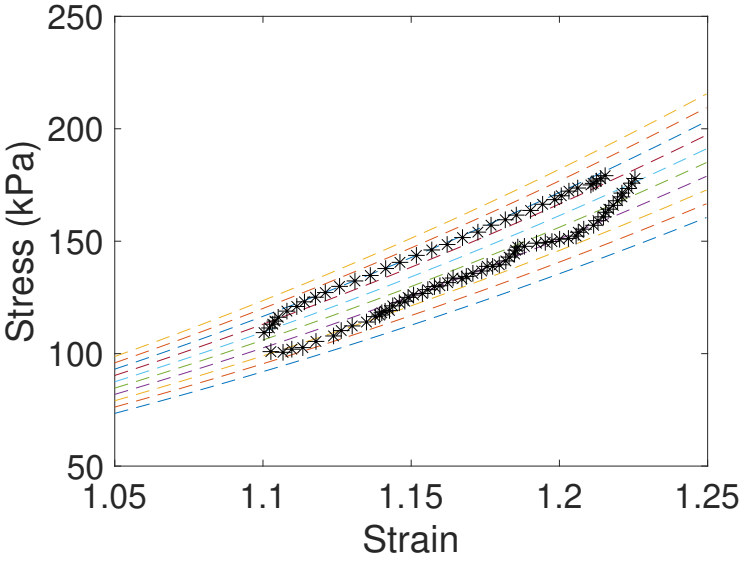

FIGURE 5.9: Relation between strain and stress in dog's arteries. Experimental data from [49] (bottom panel of Figure 1) in star symbols and the corresponding curves for different midwall radii R, and fixing the wall thickness $h_d = 0.5$ mm and the $p_o = 9$ kPa. Furthemore, the pressure p was calculated using $\beta = 2$ and G_o is as (3.16), with $E_Y = 250$ kPa.

where h_d is the wall's thickness. The stress σ is given by

$$\sigma = \frac{2\left[p_o + p\right]}{\left(\frac{R}{R_I}\right)^2 - \left(\frac{R}{R_E}\right)^2},$$

where p is transmural pressure (3.15),(3.16). The relation Strain-Stress relates how much an object is deformed respects its initial state and the force that is required to deform it. Figure 5.9 shows the experimental data in [49] for the strain-stress relation together with different midwall radii R, and fixing the wall thickness $h_d = 0.5$ mm and the $p_o = 9$ kPa. Furthermore, the pressure p was calculated using $\beta = 2$ and G_o is as (3.16), with $E_Y = 250$ kPa. As we can see, the model's parameters can satisfactorily approximate experimental data when chosen properly. Of course, the parameter values used in our numerical tests are different because they are meant for idealized aorta simulations in humans.

Conclusions

Three dimensional blood flow models provide detailed information of the fluid's evolution, giving accurate and realistic results. However, they involve a high computational cost and are not always a practical tool. As an alternative, one dimensional models have been derived in the literature. Those models consist of limiting equations that assume the cross sections to be circular with a small radius when compared to the artery's length. Of course, those models involve a low computational cost but they are limited by the conditions used to derive them. Although they have shown to be useful to simulate pressure waves, one loses detailed information of the artery's evolution.

In the fisrt part of the thesis, we have presented a new intermediate two-dimensional model that allows for arbitrary cross sections. The limiting model is valid for small cross-sectional ratios and other reasonable assumptions. We present this model as an alternative with a better balance between realism and computational cost. The resulting system is conditionally hyperbolic and the spectral properties are described. We have also provided a well-balanced positivity-resulting central-upwind scheme to obtain numerical results. We tested it in idealized aorta models with damaged areas among other scenarios.

In [13], a different expression for the transmural pressure given in (3.15) is offered in order to consider blood flows in veins. It is also possible to do it in this context as long as the fluid is Newtonian. Furthermore, in such situations one could also consider veins with twists. In the present model, the axis passing through the center of the vessel is assumed to be aligned in the (x, z) plane for simplicity. However, it can be easily generalized to any curve as along as the radius curvature does not exceed the vessel radius. The above research directions will be considered in a future work.

Part II

Generalized Quasi-Geostrophy for Moist Spatially Anisotropic Atmospheric Flows with Phase Changes

Chapter 6

Introduction: Generalized Quasi-Geostrophy

A great variety of geophysical phenomena both occurring in the ocean and the atmosphere have a direct impact in the society. Mathematical models based on Partial Differential Equations (PDEs) have demonstrated to be very useful in predicting their evolution. Such models play an important role in the area of atmospheric sciences. Due to the complexity of the phenomena under consideration, it is desirable to have at our disposal simplified models that disentangle some of the processes involved in the formation of coherent structures and their evolution as well as the triggering of atmospheric instabilities.

Among the simplified models referred to above, one of the most successful models is the celebrated quasi-geostrophic (QG) equations, which considers a balance between pressure gradients and Coriolis forces [23]. The success of the QG equations is due in part due to its practical simplicity. Only one equation of motion is necessary for the potential vorticity (PV) and the velocity and density can be diagnosed from it. From the theoretical point of view, the QG equations lead a decomposition of balance (low frequency) and unbalanced (high frequency) components. Slow balanced components are associated, for instance, to the vortices observed in the ocean and in the atmosphere. They evolve on a slow timescale and persist over time (months) as a coherent structure. On the other hand, the fast unbalanced components are associated to intertia-gravity waves and move much

faster. The study of such decomposition of the flow have received a lot of attention and a vast amount of literature exists out there regarding this phenomenon, including the spontaneous generation of inertia-gravity waves and the study of slow manifolds where flows evolve in time near balance. See [24] for a review. It has also been of interest the study of the effect of both slow and fast modes in the formation and evolution of coherent structure. In that direction, interactions between vortical and wave components in the Boussinesq and shallow water equations have been studied in [25–27].

The slow and fast modes have been mainly studied in the Boussinesq and rotating shallow water equations. In the case of the atmosphere, that corresponds to the dry case where no moist is considered at all. Very recently, a huge effort has been dedicated to developing the concept of low and high frequency components in the presence of moist. In [28],[29], the precipitating Quasi-geostrophic equations (PQG) are derived and implemented. In [29], the PQG model was analyzed in both scenarios: with saturated and unsaturated atmosphere. Although this work has been very successful, the implementation of the model is very challenging because the moist potential vorticity involves stiff terms and the the PV-inversion is very complicated.

In [30], quasi-geostrophy was generalized for anisotropic rotating flows in the dry case. The model was derived using asymptotic analysis in terms of the Rossby number and assuming certain assumptions for the characteristical scales. One notes that the asymptotic limit in this setting is different than the regular QG assumptions described above. In particular, in [30] the vertical extend is considered large compared to the horizontal lengthscale. The leading vertical velocity does not vanish, as opposed to the regular QG equations. In this work, we extend that approach taking moist into consideration. One contribution in this thesis is the derivation of a new model that encompasses a concept of balance and unbalance components in the moist case. We generalize quasi-geostrophy to the moist case in a parameter regime typical of those considered in [30]. One aside advantage here is that no PV-inversion is required. The resulting model is multi-scale where the averaged moist and equivalent potential temperature evolve over a slow timescale and the fluctuations evolving on a fast timescale.

6.1 The Boussinesq approximation for a minimal model with moisture, phase changes, turbulence and precipitation

The starting point to derive our model is the system of Boussinesq equations valid for flows in which the depth of fluid motions is small compared to the density scale height [50]. Such system can be derived from the Navier-Stokes equations [51], and are particularly helpful in this context because it filters acoustic waves and nicely decomposes inertia-gravity waves from vortex solutions. In this section we provide more details about this system.

We follow [52] for the derivation of the virtual- and equivalent- potential temperature variables in the description below. The arguments for conservation of mass and balance of momentum can be found in [38].

Conservation of mass

We begin by considering the equation for conservation of mass, which states that the mass rate of change of a parcel in a volume V is equal to the rate at which mass crosses through the boundary of the volume per unit are per unit of time. Letting m be the mass and ρ the density, the rate of change of the mass in the volume V is given by

$$\frac{d}{dt}m(V,t) = \frac{d}{dt}\int_V \rho(\mathbf{x},t)dV = \int_V \frac{\partial}{\partial t}\rho(\mathbf{x},t)dV.$$

Let $\mathbf{u}(\mathbf{x},t)$ denote the velocity field and $\mathbf{n}$ the outer normal vector at the boundary ∂V. The mass passing through the boundary can be computed by projecting the velocity field in the normal direction and taking the overall contribution over the boundary. The above statement together with the divergence's theorem we get

$$\frac{d}{dt}\int_v \rho(\mathbf{x},t)dV = -\int_{\partial V} \rho\mathbf{v}\cdot\mathbf{n}dA = -\int_V \nabla\cdot(\rho\mathbf{u})dV.$$

Since the above relations holds for an arbitrary volume, conservation of mass is finally stated as

$$\frac{\partial \rho}{\partial t} + \nabla \cdot (\rho \mathbf{u}) = 0. \tag{6.1}$$

An incompressible fluid further satisfies that the velocity is divergence free:

$$\partial_x u + \partial_y v + \partial_z w = 0.$$

See [38] for more details.

Balance of momentum

Lagrangian coordinates help us find the equations of motion of the velocity field by describing the movement of a parcel with trajectories influenced by the internal and external forces acting on the fluid. Let $\mathbf{x}(t)$ denote the particle's position at time t. The acceleration of the particle is then given by the so called material invariant

$$\frac{d}{dt} u(\mathbf{x}(t), t)) = \partial_t \mathbf{u} + \mathbf{u} \cdot \nabla \mathbf{u} =: \frac{D\mathbf{u}}{Dt}$$

Let us first consider surface forces acting on the fluid. In this work we first consider normal forces given by the pressure $p(\mathbf{x}, t)$ exerted per unit area over the surface ∂V. The overall contribution over the boundary is

$$S_{\partial V} = -\int_{\partial V} p\mathbf{n} dA = -\int_V \nabla p dV.$$

On the other hand, letting $\mathbf{b}$ denote the body forces per unit of mass, the balance of momentum reads

$$\rho \frac{D\mathbf{u}}{Dt} = -\nabla p + \rho \mathbf{b}.$$

In the Boussinesq approximation, the body forces represent the effects of gravity in the density fluctuations, and are taken to be

$$\mathbf{b} = -g \frac{\rho'}{\rho} \mathbf{k},$$

where the density is decomposed into background density plus density fluctuation $\rho = \rho_o + \bar{b}(z) + \rho'$, and $\mathbf{k} = (0, 0, 1)$ is the direction of gravity. One can rewrite the ideal gas law in terms of this decomposition, giving

$$\frac{\rho'}{\rho} = \frac{P'}{P_o} - \frac{T'}{T_o},$$

where T is the temperature, T_o a reference value and the primes represent deviations from the average value. A scaling analysis for ideal gases shows that the contributions from pressure towards buoyancy is small when $u_o^2/c^2 << T'/T_o$. See [52] for details. Here u_o is a velocity scale and c is the isentropic speed of sound. One can then approximate the buoyancy of a parcel in terms of temperature fluctuations

$$\mathbf{b} \approx g\frac{T'}{T_o}\mathbf{k}.$$

The previous approximation is a good approximation but we need one more appropriate one for a parcel that is composed of different phases such as a moist fluid. In [52], the virtual liquid potential temperature θ_{rv} is proposed to measure the temperature of an ideal gas in a hetereogenus system composed of dry air, water vapour and liquid water. It is given by

$$\theta_{rv} = \theta_v \left(1 - \frac{q_r}{1+q_r}\right)\left(1 - \frac{q_r}{\epsilon + q_t}\right)^{\chi-1}\left(1 - \frac{q_r}{q_t}\right)^{-\gamma} \exp\left[\frac{-\mathcal{L}_v q_r}{(c_{pd} + q_t c_{pv})T}\right], \tag{6.2}$$

and it is the temperature a parcel would have when experiencing volume changes during adiabatic processes but also phase changes between water vapour and liquid water due to saturation. In (6.2), the virtual potential temperature θ_v is given by

$$\theta_v = T_v \left(\frac{P_o}{P}\right)^{\chi},$$

where T_v is the virtual temperature

$$T_v = \frac{T}{1 - \frac{e}{P_d}(1-\epsilon)},$$

and

$$\epsilon = \frac{R_v}{R_d}, \gamma = \frac{q_t R_v}{c_{pd} + q_t c\text{–}pv}, \chi = \frac{R_d + q_t R_v}{c_{pd} + q_t c_{pv}}.$$

Furthermore, q is the mixing ratio in g kg^{-1} for water vapor (q_v), rainwater (q_r) and the total contribution $q_t = q_v + q_r$. The gas constants for water vapor and dry air are respectively R_v and R_d. The environmental and water vapor pressure are given by p and e respectively. Finally, the latent heat release is given by $\mathcal{L}$ and the specific heat at constant pressure for water vapor and dry air are c_{pv} and c_{pd} respectively.

The thermodynamic variables are derived so that they are preserved under adiabatic processes, and in the presence of moisture it involves complicated relations. However, such variables can be simplified under a reasonable assumption: $\frac{q_r}{q_t} << 1$ in which the amount of rain formed is considerably much smaller than the total moisture in the atmosphere as it typically happens in reality. It implies $1 + q_r \approx 1$, and the rainwater virtual potential temperature is reduced to

$$\theta_{rv} \approx \theta_v(1 - q_r) \exp\left(\frac{-\mathcal{L}_v q_r}{c_{pd} T}\right).$$

After taking a linearization θ_v around the static state of rest, we get

$$\theta_v \approx \theta + \theta \frac{e}{P}(1 - \epsilon) \approx \theta + \theta \frac{\epsilon e(1 - \epsilon)}{P\epsilon},$$

$$q_v = \frac{\epsilon e}{P}, \quad \epsilon_o = \frac{1 - \epsilon}{\epsilon}.$$

Substituting the above relations, we get

$$\theta_v \approx \theta + \theta q_v \epsilon_0.$$

Our goal is to linearize the buoyancy term with the leading order terms. In that regard, the exponential term will be ignored due to the fact that q_r is assumed to be small. The linearized rain-water potential temperature is then given by

$$\theta_{rv} \approx \theta_v(1 - q_r) \approx \theta + \theta_o q_v \epsilon_o - \theta_o q_r.$$

We must take into account that the variables associated to potential temperature and water vapor can be decomposed intro background and fluctuation. Following the Boussinesq assumptions, we assume here that the background states are explicit functions of height. As a result, the background states in the buoyancy can be absorbed into the pressure gradient. The background state for rain is zero in the absence of it. So, the buoyancy term can be expressed as

$$\mathbf{b} = \mathbf{k}g\left(\frac{\theta - \tilde{\theta}(z)}{\theta_o} + (q_v - \tilde{q}_v(z))\epsilon_o - q_r\right), \tag{6.3}$$

where $\tilde{\theta}(z)$ and $\tilde{q}_v(z)$ are the background states for potential temperature and water vapor respectively.

Balance of momentum is then expressed as

$$\frac{D\mathbf{u}}{Dt} = -\nabla\phi + \mathbf{k}g\left[\frac{\theta - \tilde{\theta}(z)}{\theta_o} + (q_v - \tilde{q}_v(z))\epsilon_o - q_r\right], \tag{6.4}$$

where $\phi = p/\rho_o$ is the effective pressure.

Time evolution of potential temperature

The potential temperature (θ) is the temperature that an ideal gas would have if it is expanded or compressed adiabatically between two pressure levels. It is a very convenient quantity to consider because it is invariant under dry adiabatic processes. A parcel rising in the atmosphere is assumed to be under an adiabatic process when it does not exchange heat with its environment while its internal energy changes due to the work done by expansion or compression. Mathematically, the potential temperature is given by

$$\theta = T\left(\frac{p_o}{p}\right)^{\frac{R_d}{c_p}},$$

where p_o is a reference pressure (at sea surface), p is the pressure, T the dry air pressure, R_d is the gas constant for dry air and c_p the specific heat capacity at constant pressure for dry air. It follows after differentiation that

$$c_p d\ln\theta = c_p d\ln T - R_d d\ln p.$$

In reversible processes, changes in the specific entropy are given by

$$dS = c_p \frac{dT}{T} - R_d \frac{dp}{p},$$

which gives

$$dS = c_p d \ln \theta.$$

As a result, the specific entropy is given by the logarithmic term of the potential temperature, which is conserved under adiabatic processes.

Based on the above calculations, the potential temperature satisfies

$$\frac{\rho c_p}{\theta} \frac{D\theta}{Dt} = \frac{Q}{T},$$

where Q is the heat production per unit of volume. In this model, this quantity is given in terms of the latent heat release that arises during phase changes but also on condensation (C) and evaporation (E) processes:

$$Q = \rho(\mathcal{L}C - \mathcal{L}E),$$

which leads to the approximation

$$\frac{D\theta}{Dt} = \frac{\mathcal{L}\tilde{\theta}(z)}{c_p \tilde{T}(z)}(C - E). \tag{6.5}$$

The above equation indicates that changes in potential temperature in a moist parcel are due to the latent heat release that happens during phase changes from water vapor to liquid water (condensation) and viceversa (evaporation). During condensation, the potential temperature increases and can direct energy the parcel in order to be transported to higher altitudes where condensation and precipitation are enhanced. On the opposite case, the potential temperature decreases during evaporation and the system requires heat while possibly inhibiting the parcel's vertical ascent.

Time evolution of moisture

In this model, one is assuming that moisture in the atmosphere can only exist in gas phase (water vapor) or in liquid phase that is obtained after condensation when the atmosphere is saturated. Any excess of water from saturation levels is considered rain and falls at a constant rainfall velocity V_T (for simplicity). That is, one assumes that the auto-conversion process where the small droplets collide and form bigger ones is fast as compared to the other processes. As a result, no cloud water suspended in air is present and the only two components of moisture are water vapor and rainwater. Under the above considerations, moisture obeys the conservation law

$$\begin{aligned} \frac{Dq_v}{Dt} &= -C + E \\ \frac{Dq_r}{Dt} - V_T \partial_z q_r &= C - E, \end{aligned}$$

which indicates that condensation (C) converts water vapor into liquid water while evaporation acts in the opposite way. One still needs to parametrize the condensation and evaporation processes. See for instance [53], where the parametrizations involve timescales in which such phase changes occur. Following [54], one also assumes that the timescales associated both to condensation and evaporation are fast. As a consequence, any rainwater that falls into an unsaturated region is instantaneously evaporated until either all rainwater is transformed into water vapor or saturation is reached. Under those assumptions, condensation and evaporation must be whatever it has to be to ensure instantaneous condensation and evaporation in the fast timescale limit. However, we note that one can rewrite the equations in the above limit where the condensation and evaporation terms do not appear explicitly. For instance, adding potential temperature and a water vapor term we get

$$\frac{D\theta_e}{Dt} = 0,$$

where $\theta_r = \theta + \frac{\mathcal{L}}{c_p} q_v$ is the equivalent potential temperature. Analogously, the total water $q_t = q - v + q_r$ satisfies

$$\frac{Dq_t}{Dt} - V_t \partial q_r = 0.$$

Under the fast auto-conversion and evaporation assumptions, water vapor and rainwater can be obtained diagnostically from total water by

$$q_v = \min(q_t, q_{vs}(z)), q_r = \max(q_t - q_{vs}(z), 0),$$

where $q_{vs}(z)$ is the water vapor at saturation.

Together with the incompressibility condition, the *inviscid* version of the FARE model described in [54] is given by

$$\begin{aligned} \frac{D\mathbf{u}}{Dt} &= -\nabla\phi + \mathbf{k}g\left[\frac{\theta-\tilde{\theta}(z)}{\theta_o} + (q_v - \tilde{q}_v(z))\epsilon_o - q_r\right], \\ \frac{D\theta_e}{Dt} &= 0, \\ \frac{Dq_t}{Dt} - V_t\partial q_r &= 0, \\ \partial_x u + \partial_y v + \partial_z w &= 0. \end{aligned} \tag{6.6}$$

The model in (6.6) is taken as the starting point. It is a simplified model that has shown to qualitatively capture observations made in nature in atmospheric flows with phase changes, precipitation and turbulence. For instance, in the presence or absence of wind shear at low altitudes, the model was shown to be able to form squall lines. This model has filtered acoustic waves but allow for slow (vortical) modes but allows for fast inertia-gravity waves. The purpose of this work is to derive new models that filter fast inertia-gravity waves in the limit when the vertical extend is large compared to the horizontal lengthscale. Such scenario is relevant in the presence of vortical hot towers, which are present in the formation of hurricanes among other phenomena.

Chapter 7

The model

As we will see below, the model that we derive here is obtained with a multi-scale approach. Each quantity is decomposed into a background state that depends only on a large vertical scale (Z) and a low time scale (T) and a fluctuation that depends on (x, y, Z) and a fast timescale (t). Both the background states and the fluctuations form a coupled system where certain inertia-gravity waves are filtered out and the fluctuations obey a QG-type evolution.

Our multi-scale model is described by equations involving small timescale for vertical vorticity and fluctuations of the vertical velocity, equivalent potential temperature, and total water. On the long timescale, the background states evolve according to turbulent fluxes given by the fluctuations while the fluctuations are linearly advected by the vertical derivatives of the background states, providing a two-way feedback. The model is given

by

$$
\begin{cases}
\begin{cases}
\partial_t \left(\nabla_\perp^2 \psi'\right) + J\left[\psi', \nabla_\perp^2 \psi'\right] - f\partial_Z w' = \nu \nabla_\perp^2 \zeta', \\
\partial_t w' + J\left[\psi', w'\right] + f\partial_Z \psi' = b' + \nu \nabla_\perp^2 w', \\
\partial_t \theta_e' + J\left[\psi', \theta_e'\right] + w' \partial_Z \overline{\theta_e} = \kappa_e \nabla_\perp^2 \theta_e', \\
\partial_t q_t' + J\left[\psi', q_t'\right] + w' \partial_Z \overline{q_t} - V_T \partial_Z q_r' = \kappa_q \nabla_\perp^2 q_t',
\end{cases} \\
\begin{cases}
\partial_T \overline{\theta_e} + \partial_Z \overline{\theta_e' w'} = \kappa_e \partial_{ZZ}^2 \overline{\theta_e} \\
\partial_T \overline{q_t} + \partial_Z \overline{q_t' w'} = \kappa_q \partial_{ZZ}^2 \overline{q_t}.
\end{cases}
\end{cases}
\tag{7.1}
$$

Here, ψ' is a stream function that defines the horizontal velocity field $\mathbf{u}_h = (u', v') = (-\partial_y \psi', \partial_x \psi')$. The Jacobian is given by $J(A, B) = -\partial_y A\, \partial_x B + \partial_x A\, \partial_y B$. The horizontal Laplacian gives the vertical vorticity $\zeta = \partial_x v - \partial_y u = \nabla_\perp^2 \psi'$. Furthermore, w' is the vertical velocity, θ_e' is the fluctuating equivalent potential temperature, and q_t', q_r' the fluctuating total water and rain water mixing ratio. The rainfall speed is V_T and it is assumed to be constant for simplicity. The horizontally averaged equivalent potential temperature and total water mixing ratios are given by $\bar{\theta}_e$ and $\bar{q}_t$ respectively. The vertical coordinate is written in capital letter Z to denote that it is in long scale. The buoyancy fluctuation is given by

$$
b' = g\left[\frac{\theta_e'}{\theta_o} - \left(\frac{L}{c_p \theta_o} - R_{vd}\right) q_t' + \left(\frac{L}{c_p \theta_o} - R_{vd} - 1\right) q_r'\right].
$$

In the above equation, all the horizontally averaged quantities are denoted with bars $\overline{(\cdot)}$, while the fluctuations are identified with primes. The validation of the model is constrained to the condition $Ro = \epsilon << 1$, where $Ro = \frac{U}{fL}$ is the Rossby number, f, U and L are the Coriolis coefficient, characteristic velocity and lengthscale. All the averaged quantities $\bar{\theta}_e, \bar{q}_t$ but also the velocity fluctuation (u', v', w') are $O(1)$ quantities. On the other hand, fluctuations θ_e', q_t', q_r' are $O(Ro)$.

As opposed to the *standard* quasi-geostrophic equations, the leading order vertical velocity does not vanish. The incompressibility of the fluid is reflected in a solvability equation where the balance occurs between the leading order vertical velocity and the order $O(Ro)$ horizontal component of the velocity. This gives the vertical vorticity equation. The streamfunction and the pressure fluctuation are related by $\psi' = p'/f$. The vertical velocity equation involves a horizontal material derivative in balance with the pressure gradient. The equations for θ_e' involves a horizontal material derivative with stratification given by the brackground averaged profile. A similar expression can be observed for the q_t'-equation, where precipitation is also included with rainfall speed V_T. The background quantities $\bar{\theta}_e$ and $\bar{q}_t$ evolve according to the turbulent fluxes $\overline{\theta_e' w'}$ and $\overline{q_t' w'}$ respectively.

7.1 Derivation of the multi-scale reduced model

7.1.1 The starting point: a minimal CRM model

This section is devoted to the derivation of the multi-scale reduced system. We first consider the FARE model [54], which is a minimal model for precipitating turbulent convection. It uses a Boussinesq approximation for the momentum and equivalent potential temperature equations. The derivation of the model assumes no supersaturation. That is, any excess of water from the water vapor at saturation is considered rain water. Furthermore, any rainwater that falls in unsaturated regions will immediately evaporate until the region saturates or all rain is transformed into water vapor in that region. The resulting model consists of the simplest conservation laws that includes both precipitation and turbulence, and are given by

$$\begin{aligned} D_t \mathbf{u} + f\hat{\mathbf{z}} \times \mathbf{u} &= -\nabla\, p + b\,(\theta_e, q_t, z)\,\hat{\mathbf{z}} + \nu \nabla^2 \mathbf{u}, \\ D_t \theta_e &= \kappa_e \nabla^2 \theta_e, \\ D_t q_t - V_T \partial_z q_r &= \kappa_q \nabla^2 q_t, \\ \nabla \cdot \mathbf{u} &= 0. \end{aligned} \tag{7.2}$$

Here $D_t f \equiv \partial_t f + \mathbf{u} \cdot \nabla f$, $\mathbf{u} = (u, v, w)$ is the velocity, p the relative pressure (resclaed by density), θ_e the equivalent potential temperature, $q_t = q_v + q_r$ the total water, $q_v = \min(q_t, q_{\text{vs}})$ the water vapor, $q_r = \max(q_t - q_{\text{vs}}, 0)$ the rain water, q_{vs} the water vapor at saturation (a known function of height), V_T the rainfall velocity, and b the buoyancy acceleration. Also, ν represents the kinematic viscocity and κ_e,κ_q means the thermal diffusivity of the equivalent potential temperature and the total mixing ratio water. See Chapter 6 for a derivation of the model.

In general, the buoyancy $b = b(\theta_e, q_v, q_r, z)$ is an explicit function of equivalent potential temperature, moist and height. It takes into account the latent heat release across phase changes and rain acts as a sink of energy. The dependance on height takes into account background states of θ_e and q_v such that only the fluctuations can generate a change in buoyancy.

$$b\left(\theta_e, q_t, z\right) = g\left[\frac{\theta_e}{\theta_o} + \left(R_{\text{vd}} - \frac{L_v}{c_p \theta_o}\right) q_t + \left(\frac{L_v}{c_p \theta_o} - R_{\text{vd}} - 1\right) q_r\right]$$

For the moment, we will not choose a specific form of the buoyancy and will assume a general function $b = b\left(\theta_e, q_t, z\right)$.

In order to derive our reduced model, we need to introduce the aspect ratio A_Z, which here is assumed to be large ($A_Z \gg 1$). This gives rise to a new large height scale Z such that $[Z] = A_Z\,[z]$. The background states in FARE are here described by averaged quantities varying on a slow time scale T such $[T] = A_T\,[t]$, with $A_T \gg 1$ to be determined later.

As usual, the vertical and time derivatives are expanded as

$$\begin{array}{c} \textit{Substitution} \\ \hline \partial_z \longrightarrow \partial_z + \partial_Z, \\ \partial_t \longrightarrow \partial_t + \partial_T, \end{array}$$

with a new extension of the material derivative D_t given by

$$D_t + \partial_T + w\partial_Z.$$

The rescaled expanded equations are

$$\begin{aligned}
D_t\mathbf{u} &+ [\partial_T + w\partial_Z]\,\mathbf{u} + f\widehat{\mathbf{z}}\times\mathbf{u} + \nabla p + &&= (b - \partial_Z p)\,\widehat{\mathbf{z}} + \nu\left(\nabla + \partial_Z\widehat{\mathbf{z}}\right)^2\mathbf{u},\\
D_t\theta_e &+ [\partial_T + w\partial_Z]\,\theta_e &&= \kappa_e\left(\nabla + \partial_Z\widehat{\mathbf{z}}\right)^2\theta_e,\\
D_t q_t &+ [\partial_T + w\partial_Z]\,q_t - V_T\left[\partial_z + \partial_Z\right]q_r &&= \kappa_q\left(\nabla + \partial_Z\widehat{\mathbf{z}}\right)^2 q_t,\\
&\nabla\cdot\mathbf{u} + \partial_Z\left(w\right) &&= 0.
\end{aligned} \tag{7.3}$$

7.1.2 The non-dimensional equations

One of the main contributions of this work is the derivation of an asymptotically reduced system assuming a large vertical scale compared to its horizontal counterpart. This is relevant for vortical hot towers and tall plume structures. The model allows us to study balanced components of the flow, heat and moist transport, and study phase changes in Taylor columns. The dry case was already derived in [55]. Here we generalize it to the moist case.

Let T_o, U_o, W_o, L_o, H_o, P_o, B_o, Θ_o and Q_o be the characteristic time, horizontal velocity, vertical velocity, horizontal lenght, vertical lenght, re-scaled pressure, bouyancy force, temperature and total mixing-ratio scales. Taking account that

$$\frac{U_o}{L_o} = \frac{W_o}{H_o} = \frac{1}{T_o}$$

we get the non-dimensional version of (7.3):

$$\begin{aligned}
\tilde{D}_t\tilde{\mathbf{u}} &+ \left[\tfrac{1}{A_T}\partial_{\tilde{T}} + \tfrac{1}{A_Z}\tilde{w}\partial_{\tilde{Z}}\right]\tilde{\mathbf{u}} &&= -E\tilde{\nabla}\,\tilde{p} - \tfrac{1}{R_o}\hat{\mathbf{z}}\times\tilde{\mathbf{u}} + \left[\Gamma\tilde{b} - \tfrac{E}{A_Z}\partial_{\tilde{Z}}\tilde{p}\right]\hat{\mathbf{z}}\\
&&&\quad + \tfrac{1}{Re}\left(\tilde{\nabla} + \tfrac{1}{A_Z}\partial_{\tilde{Z}}\widehat{\mathbf{z}}\right)^2\tilde{\mathbf{u}},\\
\tilde{D}_t\tilde{\theta}_e &+ \left[\tfrac{1}{A_T}\partial_{\tilde{T}} + \tfrac{1}{A_Z}\tilde{w}\partial_{\tilde{Z}}\right]\tilde{\theta}_e &&= \tfrac{1}{Pe^{\theta}}\left(\tilde{\nabla} + \tfrac{1}{A_Z}\partial_{\tilde{Z}}\widehat{\mathbf{z}}\right)^2\tilde{\theta}_e,\\
\tilde{D}_t\tilde{q}_t &+ \left[\tfrac{1}{A_T}\partial_{\tilde{T}} + \tfrac{1}{A_Z}\tilde{w}\partial_{\tilde{Z}}\right]\tilde{q}_t &&= V_r\left[\partial_{\tilde{z}} + \tfrac{1}{A_Z}\partial_{\tilde{Z}}\right]\tilde{q}_r + \tfrac{1}{Pe^{q}}\left(\tilde{\nabla} + \tfrac{1}{A_Z}\partial_{\tilde{Z}}\widehat{\mathbf{z}}\right)^2\tilde{q}_t,\\
&\tilde{\nabla}\cdot\tilde{\mathbf{u}} + \tfrac{1}{A_Z}\partial_{\tilde{Z}}\left(\tilde{w}\right) &&= 0.
\end{aligned} \tag{7.4}$$

Here $\tilde{D}_t\tilde{f} \equiv \partial_{\tilde{t}}\tilde{f} + \tilde{\mathbf{u}}\cdot\tilde{\nabla}\tilde{f}$, $\tilde{\mathbf{u}} = (\tilde{u},\tilde{v},\tilde{w})$. The parameters are known numbers: $E = \frac{P_o}{U_o^2}$ is the Euler number, $R_o = \frac{1}{fT_o}$ is the Rossby number, $\Gamma = \frac{B_oT_o}{W_o}$ is the bouyancy scale, $V_r = \frac{V_TT_o}{H_o}$ is the re-scaled rainfall velocity, $Re = \frac{L_oU_o}{\nu}$ is the Reynolds number, $Pe^\theta = \frac{L_oU_o}{\kappa_e}$ is the Peclet number of the equivalent potential temperature and $Pe^q = \frac{L_oU_o}{\kappa_q}$ is the Peclet number of the total mixing ratio water.

We now proceed to derive a closed set of reduced equations. For that end, let us decompose the variables $\tilde{\mathbf{v}} = \left(\tilde{\mathbf{u}},\tilde{p},\tilde{\theta}_e,\tilde{q}_t,\tilde{q}_r\right)$ as

$$\tilde{\mathbf{v}}\left(\tilde{\mathbf{x}},\tilde{Z},\tilde{t},\tilde{T}\right) = \overline{\tilde{\mathbf{v}}}\left(\tilde{Z},\tilde{T}\right) + \tilde{\mathbf{v}}'\left(\tilde{\mathbf{x}},\tilde{Z},\tilde{t},\tilde{T}\right),$$

where the overbar denotes the averages over the small and fast scales

$$\overline{\tilde{\mathbf{v}}}\left(\tilde{Z},\tilde{T}\right) = \lim_{\tau,V\to\infty}\frac{1}{\tau V}\int_{\tau,V}\tilde{\mathbf{v}}\left(\tilde{\mathbf{x}},\tilde{Z},\tilde{t},\tilde{T}\right)d\tilde{\mathbf{x}}d\tilde{t},$$

and $\tilde{\mathbf{v}}'$ is its fluctuation from its average.

We take the average of equation (7.3) over small and fast scales to obtain equations for the averaged quantities and fluctuations. In particular, the slow evolving averaged quantities are given by

$$\begin{aligned}
\tfrac{1}{A_T}\partial_{\tilde{T}}\,\overline{\tilde{\mathbf{u}}} + \tfrac{1}{A_Z}\partial_{\tilde{Z}}\,\overline{\tilde{w}\tilde{\mathbf{u}}} &= -\tfrac{1}{Ro}\widehat{\mathbf{z}}\times\overline{\tilde{\mathbf{u}}} + \left[\Gamma\overline{\tilde{b}} - \tfrac{E}{A_Z}\partial_{\tilde{Z}}\,\overline{\tilde{p}}\right]\widehat{\mathbf{z}} + \tfrac{1}{ReA_Z^2}\partial^2_{\tilde{Z}\tilde{Z}}\overline{\tilde{\mathbf{u}}},\\
\tfrac{1}{A_T}\partial_{\tilde{T}}\,\overline{\tilde{\theta}_e} + \tfrac{1}{A_Z}\partial_{\tilde{Z}}\,\overline{\tilde{w}\tilde{\theta}_e} &= \tfrac{1}{Pe^\theta A_Z^2}\partial^2_{\tilde{Z}\tilde{Z}}\overline{\tilde{\theta}_e},\\
\tfrac{1}{A_T}\partial_{\tilde{T}}\,\overline{\tilde{q}_t} + \tfrac{1}{A_Z}\partial_{\tilde{Z}}\,\overline{\tilde{w}\tilde{q}_t} &= \tfrac{V_r}{A_Z}\partial_{\tilde{Z}}\overline{\tilde{q}_r} + \tfrac{1}{Pe^qA_Z^2}\partial^2_{\tilde{Z}\tilde{Z}}\overline{\tilde{q}_t},\\
\tfrac{1}{A_Z}\partial_{\tilde{Z}}\,\overline{\tilde{w}} &= 0.
\end{aligned} \tag{7.5}$$

The non-dimensional fluctuating equations are

$$\begin{aligned}
\tilde{D}_t\tilde{\mathbf{u}}' &+ \left[\tfrac{1}{A_T}\partial_{\tilde{T}} + \tfrac{1}{A_Z}\tilde{w}\partial_{\tilde{Z}}\right]\tilde{u}' \\
&+ \tfrac{1}{A_Z}\tilde{w}'\partial_{\tilde{Z}}\overline{\tilde{\mathbf{u}}} - \tfrac{1}{A_Z}\partial_{\tilde{Z}}\overline{\tilde{w}'\tilde{\mathbf{u}}'} &&= -E\tilde{\nabla}\,\tilde{p}' - \tfrac{1}{Ro}\widehat{\mathbf{z}}\times\tilde{\mathbf{u}}' + \left(\Gamma\tilde{b}' - \tfrac{E}{A_Z}\partial_{\tilde{Z}}\,\tilde{p}'\right)\widehat{\mathbf{z}} \\
&&&\quad + \tfrac{1}{Re}\left(\tilde{\nabla} + \tfrac{1}{A_Z}\partial_{\tilde{Z}}\widehat{\mathbf{z}}\right)^2\tilde{\mathbf{u}}', \\
\tilde{D}_t\tilde{\theta}_e{}' &+ \left[\tfrac{1}{A_T}\partial_{\tilde{T}} + \tfrac{1}{A_Z}\tilde{w}\partial_{\tilde{Z}}\right]\tilde{\theta}_e{}' \\
&+ \tfrac{1}{A_Z}\tilde{w}'\partial_{\tilde{Z}}\,\overline{\tilde{\theta}_e} - \tfrac{1}{A_Z}\partial_{\tilde{Z}}\,\overline{\tilde{\theta}_e{}'\tilde{w}'} &&= \tfrac{1}{Pe^\theta}\left(\tilde{\nabla} + \tfrac{1}{A_Z}\partial_{\tilde{Z}}\widehat{\mathbf{z}}\right)^2\tilde{\theta}_e{}', \\
\tilde{D}_t\tilde{q}_t{}' &+ \left[\tfrac{1}{A_T}\partial_{\tilde{T}} + \tfrac{1}{A_Z}\tilde{w}\partial_{\tilde{Z}}\right]\tilde{q}_t{}' \\
&+ \tfrac{1}{A_Z}\tilde{w}'\partial_{\tilde{Z}}\,\overline{\tilde{q}_t} - \tfrac{1}{A_Z}\partial_{\tilde{Z}}\,\overline{\tilde{q}_t{}'\tilde{w}'} &&= V_r\left[\partial_{\tilde{z}} + \tfrac{1}{A_Z}\partial_{\tilde{Z}}\right]\tilde{q}_r{}' + \tfrac{1}{Pe^q}\left(\tilde{\nabla} + \tfrac{1}{A_Z}\partial_{\tilde{Z}}\widehat{\mathbf{z}}\right)^2\tilde{q}_t{}', \\
&\tilde{\nabla}\cdot\tilde{\mathbf{u}}' + \tfrac{1}{A_Z}\partial_{\tilde{Z}}\,\tilde{w}' &&= 0.
\end{aligned} \tag{7.6}$$

We note that the above equations are non-dimensional with coefficients in terms of physically meaningful parameters. We will assume that some of those parameters are small in certain situations in order to derive simplified models. The section is devoted to that with the use of asymptotic expansions.

7.1.3 The asymptotic expansion

The multi-scale model can be derived from an asymptotic expansion with small parameter $\epsilon := Ro$. For the system's closure, we also need the following assumptions

$$\begin{gathered}
A_Z = \epsilon^{-1},\ A_T = \epsilon^{-2},\ \Gamma = \epsilon^{-1}\Gamma^*,\ \Gamma^* = O(1),\ V_r = \epsilon^{-1}V_r^*,\ V_r^* = O(1), \\
Re = O(1),\ Pe^\theta = O(1),\ Pe^\theta = O(1).
\end{gathered} \tag{7.7}$$

That is, the aspect ratio A_Z, the buoyancy force and the rainfall speed are large and inversely proportional to the Rossby number, and A_T is one order or magnitude larger.

Let us expand the dependent quantities $\mathbf{v}$ in terms of the small parameter as

$$\tilde{\mathbf{v}} = \tilde{\mathbf{v}}_0 + \epsilon\tilde{\mathbf{v}}_1 + \epsilon^2\tilde{\mathbf{v}}_2 + \mathcal{O}\left(\epsilon^3\right).$$

Momentum equation relations

The relations obtained by the momentum equations are similar to those given in [55] in the dry case but we recall it here for completeness. Our contribution relies on the extension to the moist case done below.

In order to get hydrostatic balance at the leading order, we assume that $E = \epsilon^{-2}$, giving

$$\partial_{\tilde{Z}}\left(\overline{\tilde{p}}_0\right) = \Gamma^*\overline{\tilde{b}}_0.$$

Examination of the leading-order terms for the averaged horizontal velocities, we find that

$$\overline{\tilde{u}}_0 = \overline{\tilde{v}}_0 = 0.$$

The averaged continuity equation implies that $\overline{\tilde{w}} = 0$, deducing $\tilde{\overline{\mathbf{u}}}_0 = \mathbf{0}$. On other hand, at $\mathcal{O}\left(\epsilon^{-2}\right)$, the fluctuating momentum equations yields

$$\tilde{\nabla}\,\tilde{p}'_0 = \mathbf{0},$$

implying that $\tilde{p}'_0 = 0$. At $\mathcal{O}\left(\epsilon^{-1}\right)$, the same equation implies

$$\tilde{\nabla}\,\tilde{p}'_1 = \left(\tilde{v}'_0, -\tilde{u}'_0, \Gamma^*\tilde{b}'_0\right) \tag{7.8}$$

and, at $\mathcal{O}\left(1\right)$,

$$\tilde{D}^0_{\tilde{t}}\left(\tilde{\mathbf{u}}'_0\right) = -\tilde{\nabla}\left(\tilde{p}'_2\right) - \mathbf{z}\times\tilde{\mathbf{u}}'_1 + \left(\Gamma^*\tilde{b}'_1 - \partial_{\tilde{Z}}\left(\tilde{p}'_1\right)\right)\mathbf{z} + \frac{1}{Re}\tilde{\nabla}^2\left(\tilde{\mathbf{u}}'_0\right).$$

where $\tilde{D}^0_{\tilde{t}} = \partial_{\tilde{t}} + \tilde{\mathbf{u}}'_0\cdot\tilde{\nabla}$.

The fluctuating continuity at $\mathcal{O}(1)$ and $\mathcal{O}(\epsilon)$ are given by

$$\tilde{\nabla} \cdot \tilde{\mathbf{u}}_0' = 0, \quad \text{and} \quad \tilde{\nabla} \cdot \tilde{\mathbf{u}}_1' + \partial_{\tilde{Z}}(w_0') = 0, \tag{7.9}$$

respectively. We recall that the divergence is done with respect to the small scales (x, y, z) and leaves out the large scale $\tilde{Z}$. Equation (7.8) immediately implies

$$\partial_{\tilde{z}} \tilde{w}_0' = 0.$$

Thermodynamic and moist dynamic relations

Since $\overline{\tilde{w}} = 0$, we get $\overline{\tilde{q}\tilde{w}} = \overline{\tilde{q}'\tilde{w}'}$ for any quantity $\tilde{q}$. The leading-order term in the mean buoyancy equation is given by

$$\partial_{\tilde{Z}} \left(\overline{\tilde{\theta}_{e,0}' \tilde{w}_0'} \right) = 0,$$

which implies that $\overline{\tilde{\theta}_{e,0}' \tilde{w}_0'} = 0$. We would take the sufficient condition $\tilde{\theta}_{e,0}' = 0$. That is, we assume that the equivalent potential temperature fluctuations are at least order $\mathcal{O}(\epsilon)$. Thus, at $\mathcal{O}(\epsilon)$, the averaged and fluctuating buoyancy equations become

$$\begin{aligned} \partial_{\tilde{T}} \left(\overline{\tilde{\theta}}_{e,0} \right) + \partial_{\tilde{Z}} \left(\overline{\tilde{\theta}_{e,1}' \tilde{w}_0'} \right) &= \frac{1}{Pe^{\theta}} \partial_{\tilde{Z}\tilde{Z}}^2 \left(\overline{\tilde{\theta}}_{e,0} \right), \\ \tilde{D}_{\tilde{t}}^0 \left(\tilde{\theta}_{e,1}' \right) + \tilde{w}_0' \partial_{\tilde{Z}} \left(\overline{\tilde{\theta}}_{e,0} \right) &= \frac{1}{Pe^{\theta}} \tilde{\nabla}^2 \left(\tilde{\theta}_{e,1}' \right). \end{aligned}$$

Using the fact that $V_r = O(\epsilon^{-1})$, the leading order term in the equation for the averaged moisture equation gives

$$\partial_{\tilde{Z}} \left(\overline{\tilde{q}}_{r,0} \right) = 0.$$

We will assume that $\overline{\tilde{q}}_{r,0}$, which implies that the averaged rain is order $O(\epsilon)$. This is a reasonable assumption since rain is usually much smaller than water vapor. The leading-order term of the averaging mixing ratio equation yields

$$\partial_{\tilde{Z}} \left(\overline{\tilde{q}_{t,0}' \tilde{w}_0'} \right) - V_r^* \partial_{\tilde{Z}} \overline{\tilde{q}}_{r,1} = 0.$$

We will use the solvability condition $\tilde{q}_{t,o}' = 0$, which implies that the total water fluctuations are order $O(\epsilon)$, and consequently $\overline{\tilde{q}}_{r,1} = 0$. This together with $\overline{\tilde{q}}_{r,0} = 0$ implies

that the only leading order moisture term is $\overline{\tilde{q}_t}_{,0}$. Finally, the terms of order $O(\epsilon^2)$ in the averaged moisture equation, the solvability condition $\overline{\tilde{q}_r}_{,2} = 0$, and the terms of order $O(\epsilon)$ in the fluctuating moisture equations are given by

$$\begin{aligned}
\partial_{\tilde{T}}\left(\overline{\tilde{q}_t}_{,0}\right) + \partial_{\tilde{Z}}\left(\overline{\tilde{q}'_{t,1}\tilde{w}'_0}\right) &= \frac{1}{Pe^q}\partial^2_{\tilde{Z}\tilde{Z}}\left(\overline{\tilde{q}_t}_{,0}\right), \\
\tilde{D}^0_{\tilde{t}}\left(\tilde{q}'_{t,1}\right) + \tilde{w}'_0\partial_{\tilde{Z}}\left(\overline{\tilde{q}_t}_{,0}\right) &= V^*_r\Big(\partial_{\tilde{z}}\left(\tilde{q}'_{r,2}\right) + \partial_{\tilde{Z}}\left(q'_{r,1}\right)\Big) + \frac{1}{Pe^q}\tilde{\nabla}^2\left(\tilde{q}'_{t,1}\right).
\end{aligned}$$

The Taylor-Proudman constraints and a streamfunction formulation

Following [55], our next step is to find the Taylor-Proudman constraints. These relations express that the forces leading-order motion on small spatial scales are invariant in the direction of the rotation axis, e.g., f satisfies a Taylor-Proudman constraint if

$$\left(\hat{\mathbf{z}}\cdot\tilde{\nabla}\right)\left(\tilde{f}\right) = 0.$$

The equation $\tilde{\nabla}\left(\tilde{p}'_1\right) = \left(\tilde{v}'_0, -\tilde{u}'_0, \Gamma^*\tilde{b}'_0\right)$ shows that the leading-order flow is in geostrophic balance. As $\tilde{\partial}_z\left(\tilde{w}'_0\right) = 0$ from the continuity equation at $\mathcal{O}(1)$ and assuming that $\tilde{b}'_0 = 0$, we find that

$$\left(\hat{\mathbf{z}}\cdot\tilde{\nabla}\right)\left(\tilde{\mathbf{u}}'_0\right) = \mathbf{0}.$$

Also, $\tilde{b}'_0 = 0$ implies that $\left(\hat{\mathbf{z}}\cdot\tilde{\nabla}\right)\left(\tilde{p}'_1\right) = 0$. Applying $\left(\hat{\mathbf{z}}\cdot\tilde{\nabla}\right)$ to $\tilde{D}^0_{\tilde{t}}\left(\tilde{\theta}'_{e,1}\right)$ we obtain

$$\left(\hat{\mathbf{z}}\cdot\tilde{\nabla}\right)\left(\tilde{\theta}'_{e,1}\right) = 0.$$

These three relations show that $\tilde{\mathbf{u}}'_0$, $\tilde{p}'_1$ and $\tilde{\theta}'_{e,1}$ depend only on the large scale $\tilde{Z}$ in height. We still need to define the solvability equations, that allows us to find the other constraints and the reduced system of equations. These solvability equations are

$$\partial_{\tilde{x}}\left(\tilde{u}'_1\right) + \partial_{\tilde{y}}\left(\tilde{v}'_1\right) + \partial_{\tilde{Z}}\left(\tilde{w}'_0\right) = 0,$$

$$\tilde{D}^0_{\tilde{t}}\left(\tilde{w}'_0\right) = \Gamma^*\tilde{b}'_1 - \partial_{\tilde{Z}}\left(\tilde{p}'_1\right) + \frac{1}{Re}\tilde{\nabla}^2_{\perp}\left(\tilde{w}'_0\right),$$

and

$$\tilde{D}_{\tilde{t}}^{0}\left(\tilde{q}_{t,1}'\right)+\tilde{w}_{0}'\partial_{\tilde{Z}}\left(\overline{\tilde{q}_{t,0}}\right)=V_{r}^{*}\partial_{\tilde{Z}}\left(\tilde{q}_{r,1}'\right)+\frac{1}{Pe^{q}}\tilde{\nabla}_{\perp}^{2}\left(\tilde{q}_{t,1}'\right),$$

and each one provides a Taylor-Proudman constraint:

$$\left(\hat{\mathbf{z}}\cdot\tilde{\nabla}\right)\left(\tilde{w}_{1}'\right)=0,\quad\left(\hat{\mathbf{z}}\cdot\tilde{\nabla}\right)\left(\tilde{p}_{2}'\right)=0,\quad\left(\hat{\mathbf{z}}\cdot\tilde{\nabla}\right)\left(\tilde{q}_{r,2}'\right)=0,$$

respectively. Finally, by the fluctuating horizontal momentum equation, the first equation of the above system is transformed into

$$\partial_{\tilde{t}}\left(\tilde{\nabla}_{\perp}^{2}\tilde{p}_{1}'\right)+u_{0}'\partial_{\tilde{x}}\left(\tilde{\nabla}_{\perp}^{2}\tilde{p}_{1}'\right)+v_{0}'\partial_{\tilde{y}}\left(\tilde{\nabla}_{\perp}^{2}\tilde{p}_{1}'\right)-\partial_{\tilde{Z}}\left(\tilde{w}_{0}'\right)=\frac{1}{Re}\tilde{\nabla}_{\perp}^{2}\left(\tilde{\nabla}_{\perp}^{2}\tilde{p}_{1}'\right).$$

To summarize, the reduced system of equations is given by

$$\begin{aligned}
\partial_{\tilde{t}}\left(\tilde{\nabla}_{\perp}^{2}\tilde{p}_{1}'\right)+\tilde{u}_{0}'\partial_{\tilde{x}}\left(\tilde{\nabla}_{\perp}^{2}\tilde{p}_{1}'\right)+\tilde{v}_{0}'\partial_{\tilde{y}}\left(\tilde{\nabla}_{\perp}^{2}\tilde{p}_{1}'\right)-\partial_{\tilde{Z}}\left(\tilde{w}_{0}'\right) &= \tfrac{1}{Re}\tilde{\nabla}_{\perp}^{2}\left(\tilde{\nabla}_{\perp}^{2}\tilde{p}_{1}'\right),\\
\partial_{\tilde{t}}\left(\tilde{w}_{0}'\right)+\tilde{u}_{0}'\partial_{\tilde{x}}\left(\tilde{w}_{0}'\right)+\tilde{v}_{0}'\partial_{\tilde{y}}\left(\tilde{w}_{0}'\right)+\partial_{\tilde{Z}}\left(\tilde{p}_{1}'\right) &= \Gamma^{*}\tilde{b}_{1}'+\tfrac{1}{Re}\tilde{\nabla}_{\perp}^{2}\left(\tilde{w}_{0}'\right),\\
\partial_{\tilde{t}}\left(\tilde{\theta}_{e,1}'\right)+\tilde{u}_{0}'\partial_{\tilde{x}}\left(\tilde{\theta}_{e,1}'\right)+\tilde{v}_{0}'\partial_{\tilde{y}}\left(\tilde{\theta}_{e,1}'\right)+\partial_{\tilde{Z}}\left(\overline{\tilde{\theta}_{e,0}}\right)\tilde{w}_{0}' &= \tfrac{1}{Pe^{\theta}}\tilde{\nabla}_{\perp}^{2}\left(\tilde{\theta}_{e,1}'\right),\\
\partial_{\tilde{t}}\left(\tilde{q}_{t,1}'\right)+\tilde{u}_{0}'\partial_{\tilde{x}}\left(\tilde{q}_{t,1}'\right)+\tilde{v}_{0}'\partial_{\tilde{y}}\left(\tilde{q}_{t,1}'\right)+\partial_{\tilde{Z}}\left(\overline{\tilde{q}_{t,0}}\right)\tilde{w}_{0}' &= V_{r}^{*}\partial_{\tilde{Z}}\left(\tilde{q}_{r,1}'\right)+\tfrac{1}{Pe^{q}}\tilde{\nabla}_{\perp}^{2}\left(\tilde{q}_{t,1}'\right),\\
\partial_{\tilde{T}}\left(\overline{\tilde{\theta}_{e,0}}\right)+\partial_{\tilde{Z}}\left(\overline{\tilde{\theta}_{e,1}'\tilde{w}_{0}'}\right) &= \tfrac{1}{Pe^{\theta}}\partial_{\tilde{Z}\tilde{Z}}^{2}\left(\overline{\tilde{\theta}_{e,0}}\right),\\
\partial_{\tilde{T}}\left(\overline{\tilde{q}_{t,0}}\right)+\partial_{\tilde{Z}}\left(\overline{\tilde{q}_{t,1}'\tilde{w}_{0}'}\right) &= \tfrac{1}{Pe^{q}}\partial_{\tilde{Z}\tilde{Z}}^{2}\left(\overline{\tilde{q}_{t,0}}\right).
\end{aligned}\tag{7.10}$$

By [56], our reduced system of equations can be adapted at a streamfunction formulation defined by

$$\tilde{\mathbf{u}}'=-\tilde{\nabla}\times\tilde{\psi}\hat{\mathbf{z}}-\tilde{\nabla}\times\tilde{\nabla}\times\tilde{\phi}\hat{\mathbf{z}}.$$

The above constraints helps us to find that

$$\begin{aligned}
\tilde{\mathbf{u}}_{0}' &= \left(-\partial_{\tilde{y}}\tilde{\psi}_{0},\partial_{\tilde{x}}\tilde{\psi}_{0},\tilde{\nabla}_{\perp}^{2}\tilde{\phi}_{0}\right)^{T},\\
\tilde{\mathbf{u}}_{1}' &= \left(-\partial_{\tilde{x}\tilde{Z}}^{2}\tilde{\phi}_{0},-\partial_{\tilde{y}\tilde{Z}}^{2}\tilde{\phi}_{0},0\right)^{T}+\left(-\partial_{\tilde{y}}\tilde{\psi}_{1},\partial_{\tilde{x}}\tilde{\psi}_{1},\tilde{\nabla}_{\perp}^{2}\tilde{\phi}_{1}\right)^{T}.
\end{aligned}$$

If we choose as $\tilde{p}'_1 = \tilde{\psi}_0$, $\tilde{w}' = \tilde{\nabla}^2_\perp \tilde{\phi}$ and define $\tilde{J}\left[\tilde{f}, \tilde{g}\right] := \partial_{\tilde{x}}\tilde{f}\partial_{\tilde{y}}\tilde{g} - \partial_{\tilde{y}}\tilde{f}\partial_{\tilde{x}}\tilde{g}$, the reduced system of equations is

$$\begin{array}{lcllcl}
\partial_{\tilde{t}}\left(\tilde{\nabla}^2_\perp\tilde{\psi}_0\right) & + & \tilde{J}\left[\tilde{\psi}_0, \tilde{\nabla}^2_\perp\tilde{\psi}_0\right] & - & \partial_{\tilde{Z}}\left(\tilde{\nabla}^2_\perp\tilde{\phi}_0\right) & = & \frac{1}{Re}\tilde{\nabla}^2_\perp\left(\tilde{\nabla}^2_\perp\tilde{\psi}_0\right), \\
\partial_{\tilde{t}}\left(\tilde{\nabla}^2_\perp\tilde{\phi}_0\right) & + & \tilde{J}\left[\tilde{\psi}_0, \tilde{\nabla}^2_\perp\tilde{\phi}_0\right] & + & \partial_{\tilde{Z}}\left(\tilde{\psi}_0\right) & = & \Gamma^*\tilde{b}'_1 + \frac{1}{Re}\tilde{\nabla}^2_\perp\left(\tilde{\nabla}^2_\perp\tilde{\phi}_0\right), \\
\partial_{\tilde{t}}\left(\tilde{\theta}'_{e,1}\right) & + & \tilde{J}\left[\tilde{\psi}_0, \tilde{\theta}'_{e,1}\right] & + & \tilde{\nabla}^2_\perp\tilde{\phi}_0\partial_{\tilde{Z}}\left(\overline{\tilde{\theta}}_{e,0}\right) & = & \frac{1}{Pe^\theta}\tilde{\nabla}^2_\perp\left(\tilde{\theta}'_{e,1}\right), \\
\partial_{\tilde{t}}\left(\tilde{q}'_{t,1}\right) & + & \tilde{J}\left[\tilde{\psi}_0, \tilde{q}'_{t,1}\right] & + & \tilde{\nabla}^2_\perp\tilde{\phi}_0\partial_{\tilde{Z}}\left(\overline{\tilde{q}}_{t,0}\right) & = & V_r^*\partial_{\tilde{Z}}\left(\tilde{q}'_{r,1}\right) + \frac{1}{Pe^q}\tilde{\nabla}^2_\perp\left(\tilde{q}'_{t,1}\right), \\
 & & \partial_{\tilde{T}}\left(\overline{\tilde{\theta}}_{e,0}\right) & + & \partial_{\tilde{Z}}\left(\overline{\tilde{\theta}'_{e,1}\tilde{w}'_0}\right) & = & \frac{1}{Pe^\theta}\partial^2_{\tilde{Z}\tilde{Z}}\left(\overline{\tilde{\theta}}_{e,0}\right), \\
 & & \partial_{\tilde{T}}\left(\overline{\tilde{q}}_{t,0}\right) & + & \partial_{\tilde{Z}}\left(\overline{\tilde{q}'_{t,1}\tilde{w}'_0}\right) & = & \frac{1}{Pe^q}\partial^2_{\tilde{Z}\tilde{Z}}\left(\overline{\tilde{q}}_{t,0}\right).
\end{array} \tag{7.11}$$

The reduced system is closed, because

$$\tilde{b}'_1 = \tilde{b}'_1\left(\tilde{\theta}'_{e,1}, \tilde{q}'_{t,1}, \tilde{Z}\right), \quad \tilde{q}'_{r,1} = \tilde{q}'_{r,1}\left(\tilde{q}'_{t,1}, \tilde{Z}\right)$$

are linear functions of their corresponding inputs.

7.1.4 The final system in dimensional form

We recall that the scales are related by $[Z] = \epsilon^{-1}[z]$, and $[T] = \epsilon^{-2}[t]$. In dimensional form, we need to obtain the equations for $\psi_o, w_o, \epsilon\theta'_{e,1}, \epsilon q'_{t,1}, \epsilon q'_{r,1}, \epsilon b'_1, \bar{\theta}_{e,o}$, and $\bar{q}_{t,o}$, which are the terms appearing in the asymptotic expansion. For simplicity, we will redefine them by $\psi, w, \theta'_e, q'_t, q'_r, b', \bar{\theta}_e$, and $\bar{q}_t$ respectively.

In dimensional form, the following relations hold

$$\psi' = p'/f, \quad u' = -\partial_y\psi', \quad v' = \partial_x\psi', \quad \nabla^2_\perp\psi' = \partial_x v' - \partial_y u'.$$

Defining the vertical vorticity by $\zeta' = \partial_x v' - \partial_y u'$, and the Jacobian by $J[A,B] = -\partial_y A \partial_x B + \partial_x A \partial_y B$, we get

$$\begin{aligned}
\partial_t \zeta' &+ J[\psi', \zeta'] - f\partial_Z w' &= \nu \nabla_\perp^2 \zeta', \\
\partial_t w' &+ J[\psi', w'] + f\partial_Z \psi' &= b' + \nu \nabla_\perp^2 w', \\
\partial_t \theta_e' &+ J[\psi', \theta_e'] + w' \partial_Z \overline{\theta_e} &= \kappa_e \nabla_\perp^2 \theta_e', \\
\partial_t q_t' &+ J[\psi', q_t'] + w' \partial_Z \overline{q_t} &= V_T \partial_Z q_r' + \kappa_q \nabla_\perp^2 q_t', \\
\partial_T \overline{\theta_e} &+ \partial_Z \overline{\theta_e' w'} &= \kappa_e \partial_{ZZ}^2 \overline{\theta_e}, \\
\partial_T \overline{q_t} &+ \partial_Z \overline{q_t' w'} &= \kappa_q \partial_{ZZ}^2 \overline{q_t}.
\end{aligned} \tag{7.12}$$

It can also be written in the more conventional form, given by

$$\begin{cases}
\begin{cases}
D_t^h \zeta' - f\partial_Z w' = \nu \nabla_\perp^2 \zeta', \\
D_t^h w' + f\partial_Z \psi' = b' + \nu \nabla_\perp^2 w', \\
D_t^h \theta_e' + w' \partial_Z \overline{\theta_e} = \kappa_e \nabla_\perp^2 \theta_e', \\
D_t^h q_t' + w' \partial_Z \overline{q_t} = V_T \partial_Z q_r' + \kappa_q \nabla_\perp^2 q_t',
\end{cases} \\
\begin{cases}
\partial_T \overline{\theta_e} + \partial_Z \overline{\theta_e' w'} = \kappa_e \partial_{ZZ}^2 \overline{\theta_e}, \\
\partial_T \overline{q_t} + \partial_Z \overline{q_t' w'} = \kappa_q \partial_{ZZ}^2 \overline{q_t}.
\end{cases}
\end{cases} \tag{7.13}$$

where $D_t^h = \partial_t + \mathbf{u}_h' \cdot \nabla_h$ is the horizontal material derivative, $u_h' = (u', v')$ and $\nabla_h = (\partial_x, \partial_y)$. As one can see, the buoyancy fluctuation b' can be any function of θ_e', q_t', z. Here

we take it as in [54], which is

$$b' = g\left[\frac{\theta'_e}{\theta_o} - \left(\frac{L}{c_p\theta_o} - R_{vd}\right)q'_t + \left(\frac{L}{c_p\theta_o} - R_{vd} - 1\right)q'_r\right],$$

where $L_v = 2.5 \times 10^6$ J kg^{-1} is the latent heat factor, $\frac{R_v}{R_d} = R_{vd} + 1$ is a ratio of gas constants for water vapor $R_v = 462$ J kg^{-1} K^{-1} and dry air $R_d = 287$ J kg^{-1} K^{-1}, $R_{vd} \approx 0.6$, $c_p = 10^3$ J kg^{-1} K^{-1} is the specific heat at constant pressure, $\theta_o = 300$ K is a potential temperature reference at sea surface, and $g = 9.81$ m s^{-2} is the acceleration due to gravity. We note that the fluctuating rain q'_r is obtained from the full moisture variable, and it is given by

$$q'_r = \max(\overline{q_t} + q'_t - q_{vs}(Z), 0).$$

That is, rain is any excess of water from the water vapor at saturation $q_{vs}(Z)$, which is assumed to be a given function of height.

The first set of equations corresponds to the variables evolving on a fast timescale t, which are fluctuations from the averages. The background states given by the horizontal averages evolve on the slow timescale T. The first term involving Coriolis effects appears there from the continuity and the Taylor-Proudman constraints. The other term with the Coriolis parameter appears due to the balance of the material derivative of the vertical velocity and the pressure gradient. The averaged quantities in the equations evolving on a slow timescale affect the fluctuations by linear advection. On the other hand, the fluctuations cause changes in the background states through turbulent fluxes.

We note that one needs to recover $\tilde{u}', v'$ from the relation $\nabla^2_\perp \psi' = \partial_x v' - \partial_y \tilde{u}'$. Assuming horizontal periodic boundary conditions, the horizontal Laplacian can be inverted, except for the wavenumber $\mathbf{k}_h = (k_x, k_y) = \mathbf{0}$, which correspond to the horizontal average. However, since $\tilde{u}', v'$ are fluctuations and we are assuming they do not depend on the small scale z, the horizontal averages are zero. As a result, the horizontal Laplacian can be inverted, subject to the above conditions.

Chapter 8

Linear (in)stability of the model

The FARE model was proposed as a simplification of the moist dynamics, and it is that simplicity that we want to exploit to provide a mathematical framework for convective instabilities. In [57], a linearized FARE model was proposed and used to explore conditional instabilities depending on the moisture and potential temperature profiles.

Here, we propose a linearized GQG FARE model to be analyzed. Due to the complexity of phase changes, we analyze the linear model in two separate scenarios: unsaturated vs saturad conditions. The buoyancy has two different expressions in both cases, which are given by

$$b' = \begin{cases} \dfrac{g}{\theta_o}\theta'_e - g\left(\dfrac{L_v}{c_p\theta_o} - R_{\text{vd}}\right) q'_t & \text{in the unsaturated case.} \\ \dfrac{g}{\theta_o}\theta'_e - g q'_t & \text{in the saturated case.} \end{cases}$$

8.1 Unsaturated regime

In unsaturated regions of the atmosphere, $q'_r = 0$. The bouyancy force in this regime is defined as

$$b'_u = \frac{g}{\theta_o}\theta'_e - g\left(\frac{L_v}{c_p\theta_o} - R_{\text{vd}}\right) q'_t.$$

The linearized model of (7.13) may be written as

$$\begin{aligned}
\partial_t \zeta' &- f\partial_Z w' &&= 0,\\
\partial_t w' &+ f\partial_Z \psi' &&= b'_u,\\
\partial_t \theta'_e &+ \partial_Z\left(\overline{\theta_e}\right) w' &&= 0,\\
\partial_t q'_t &+ \partial_Z\left(\overline{q_t}\right) w' &&= 0.
\end{aligned} \tag{8.1}$$

In order to make all variables to have te same units for purposes of eigenvector's presentation, we define

$$\Theta'_e = \frac{g}{\theta_o}\frac{\theta'_e}{|\Gamma_e|^{1/2}}, \quad Q'_u = g\frac{q'_t}{\left(\Gamma_u - \Gamma_e\right)^{1/2}},$$

where

$$\Gamma_e = \frac{g}{\theta_o}\partial_Z\left(\overline{\theta_e}\right), \quad \Gamma_u = \frac{g}{\theta_o}\partial_Z\left(\overline{\theta_e}\right) - g\left(\frac{L_v}{c_p\theta_o} - R_{\text{vd}}\right)\partial_Z\left(\overline{q_t}\right).$$

We note that $\Gamma_u - \Gamma_e$ is always positive but Γ_e may be negative in physically relevant regimes we are interested in. In those variables, the linearized equations become

$$\begin{aligned}
\partial_t \zeta' &- f\partial_Z w' &&= 0,\\
\partial_t w' &+ f\partial_Z \psi' &&= |\Gamma_e|^{1/2}\Theta'_e - \left(\Gamma_u - \Gamma_e\right)^{1/2} Q'_u,\\
\partial_t \Theta'_e &+ \operatorname{sign}\left(\Gamma_e\right)|\Gamma_e|^{1/2} w' &&= 0,\\
\partial_t Q'_u &- \left(\Gamma_u - \Gamma_e\right)^{1/2} w' &&= 0.
\end{aligned} \tag{8.2}$$

Periodic boundary conditions allows for plane-wave solutions of the form

$$(\cdot)\left(\mathbf{x}, t; \mathbf{k}\right) = \widehat{(\cdot)}\left(\mathbf{k}\right)\exp\left\{i\left[\mathbf{k}\cdot x - \sigma\left(\mathbf{k}\right)t\right]\right\}$$

where $\mathbf{x} = (x, y, Z)$ is the position, $\mathbf{k} = (k_x, k_y, k_Z)$ is the wavevector and $k_h = \sqrt{k_x^2 + k_y^2}$

is the horizontal wavenumber. As $\zeta' = \nabla_\perp^2 \psi'$, then $\widehat{\zeta'} = -k_h^2 \widehat{\psi'}$. Then, the equations become

$$
\begin{aligned}
(-i\sigma)\left(-k_h^2\right)\widehat{\psi'} &= f\,(ik_Z)\,\widehat{w'}, \\
(-i\sigma)\,\widehat{w'} &= -f\,(ik_Z)\,\widehat{\psi'} + |\Gamma_e|^{1/2}\widehat{\Theta'_e} - (\Gamma_u - \Gamma_e)^{1/2}\,\widehat{Q'_u}, \\
(-i\sigma)\,\widehat{\Theta'_e} &= -\mathrm{sign}\,(\Gamma_e)\,|\Gamma_e|^{1/2}\widehat{w'}, \\
(-i\sigma)\,\widehat{Q'_u} &= (\Gamma_u - \Gamma_e)^{1/2}\,\widehat{w'}.
\end{aligned}
$$

If $k_h \neq 0$, the equation for $k_h\widehat{\psi'}$,$\widehat{w'}$,$\widehat{\Theta'_e}$ and $\widehat{Q'_u}$ can be written in matrix form as

$$
\begin{pmatrix}
0 & fk_h^{-1}k_Z & 0 & 0 \\
fk_h^{-1}k_Z & 0 & i|\Gamma_e|^{1/2} & -i\,(\Gamma_u - \Gamma_e)^{1/2} \\
0 & -i\,\mathrm{sign}\,(\Gamma_e)\,|\Gamma_e|^{1/2} & 0 & 0 \\
0 & i\,(\Gamma_u - \Gamma_e)^{1/2} & 0 & 0
\end{pmatrix}
\begin{pmatrix} k_h\widehat{\psi'} \\ \widehat{w'} \\ \widehat{\Theta'_e} \\ \widehat{Q'_u} \end{pmatrix}
= \sigma
\begin{pmatrix} k_h\widehat{\psi'} \\ \widehat{w'} \\ \widehat{\Theta'_e} \\ \widehat{Q'_u} \end{pmatrix}. \tag{8.3}
$$

The characteristic polynomial of the above matrix is given by

$$
\sigma^2\left[\sigma^2 - \left(\frac{fk_Z}{k_h}\right)^2 - \Gamma_u\right] = 0.
$$

The eigenvalue $\sigma = 0$ has geometrical multiplicity 2, with eigemodes the following four-dimensional vectors $\left(k_h\widehat{\psi'}, \widehat{w'}, \widehat{\Theta'_e}, \widehat{Q'_u}\right)$

$$
\phi^0 = \begin{pmatrix} i\,(\Gamma_u - \Gamma_e)^{1/2} \\ 0 \\ 0 \\ fk_h^{-1}k_Z \end{pmatrix}, \quad \text{and } \phi^{00} = \begin{pmatrix} 0 \\ 0 \\ (\Gamma_u - \Gamma_e)^{1/2} \\ |\Gamma_e|^{1/2} \end{pmatrix}.
$$

The other eigenvalues are real, subject to the condition

$$
\Gamma_u + \left(\frac{fk_Z}{k_h}\right)^2 > 0.
$$

In this case, the other eigenvalues are:

$$\sigma^{\pm} = \sqrt{\Gamma_u + \left(\frac{f k_Z}{k_h}\right)^2},$$

and their respectively eigenmodes $\left(k_h\widehat{\psi'}, \widehat{w'}, \widehat{\Theta'_e}, \widehat{Q'_u}\right)$ are

$$\phi^{\pm} = \begin{pmatrix} f k_h^{-1} k_Z \\ \sigma^{\pm} \\ -i \,\mathrm{sign}\left(\Gamma_e\right) |\Gamma_e|^{1/2} \\ -i \left(\Gamma_u - \Gamma_e\right)^{1/2} \end{pmatrix}.$$

The above matrix is Hermitian provided that $\mathrm{sign}\left(\Gamma_e\right) = 1$, in which case the eigenvalues are real.

8.2 Saturated regime

In saturated regions of the atmosphere, $q'_v = 0$. The bouyancy force in this regime is defined as

$$b'_s = \frac{g}{\theta_o}\theta'_e - g q'_t.$$

The linearized model of (7.13) may be written by

$$\begin{aligned}
\partial_t \zeta' \;-\; f\partial_Z w' &= 0, \\
\partial_t w' \;+\; f\partial_Z \psi' &= b'_s, \\
\partial_t \theta'_e \;+\; \partial_Z\left(\overline{\theta_e}\right) w' &= 0, \\
\partial_t q'_t \;+\; \partial_Z\left(\overline{q_t}\right) w' &= V_T \partial_Z q'_t.
\end{aligned} \tag{8.4}$$

In order to make all variables have te same units for purposes of eigenvector's presentation, we define

$$\Theta'_e = \frac{g}{\theta_o}\frac{\theta'_e}{|\Gamma_e|^{1/2}}, \quad Q'_s = g\frac{q'_t}{(\Gamma_s - \Gamma_e)^{1/2}},$$

where

$$\Gamma_e = \frac{g}{\theta_o}\partial_Z\left(\overline{\theta_e}\right), \quad \Gamma_s = \frac{g}{\theta_o}\partial_Z\left(\overline{\theta_e}\right) - g\partial_Z\left(\overline{q_t}\right).$$

We note that $\Gamma_s - \Gamma_e$ is always positive but Γ_e may be negative in physically relevant regimes we are interested in. In those variables, the linearized equations become

$$\begin{aligned}
\partial_t\zeta' &- f\partial_Z w' &&= 0,\\
\partial_t w' &+ f\partial_Z\psi' &&= |\Gamma_e|^{1/2}\Theta'_e - (\Gamma_s - \Gamma_e)^{1/2} Q'_s,\\
\partial_t\Theta'_e &+ \operatorname{sign}(\Gamma_e)|\Gamma_e|^{1/2} w' &&= 0,\\
\partial_t Q'_s &- (\Gamma_s - \Gamma_e)^{1/2} w' &&= V_T\partial_Z Q'_s.
\end{aligned} \tag{8.5}$$

Allowing again for plane-wave solutions, the equations become

$$\begin{aligned}
(-i\sigma)\left(-k_h^2\right)\widehat{\psi'} &= f(ik_Z)\widehat{w'},\\
(-i\sigma)\widehat{w'} &= -f(ik_Z)\widehat{\psi'} + |\Gamma_e|^{1/2}\widehat{\Theta'_e} - (\Gamma_s - \Gamma_e)^{1/2}\widehat{Q'_s},\\
(-i\sigma)\widehat{\Theta'_e} &= -\operatorname{sign}(\Gamma_e)|\Gamma_e|^{1/2}\widehat{w'},\\
(-i\sigma)\widehat{Q'_s} &= (\Gamma_s - \Gamma_e)^{1/2}\widehat{w'} + V_T(ik_Z)\widehat{Q'_s}.
\end{aligned}$$

If $k_h \neq 0$, the equation for $k_h\widehat{\psi'}$,$\widehat{w'}$,$\widehat{\Theta'_e}$ and $\widehat{Q'_s}$ can be written in matrix form as

$$\begin{pmatrix}
0 & fk_h^{-1}k_Z & 0 & 0\\
fk_h^{-1}k_Z & 0 & i|\Gamma_e|^{1/2} & -i(\Gamma_s - \Gamma_e)^{1/2}\\
0 & -i\operatorname{sign}(\Gamma_e)|\Gamma_e|^{1/2} & 0 & 0\\
0 & i(\Gamma_s - \Gamma_e)^{1/2} & 0 & -V_T k_Z
\end{pmatrix}
\begin{pmatrix} k_h\widehat{\psi'}\\ \widehat{w'}\\ \widehat{\Theta'_e}\\ \widehat{Q'_s}\end{pmatrix}
= \sigma
\begin{pmatrix} k_h\widehat{\psi'}\\ \widehat{w'}\\ \widehat{\Theta'_e}\\ \widehat{Q'_s}\end{pmatrix}. \tag{8.6}$$

The characteristic polynomial is a fourth order polynomial of σ,

$$\sigma\left\{\sigma^3 + V_T k_Z \sigma^2 - \left[\left(\frac{f k_Z}{k_h}\right)^2 + \Gamma_s\right]\sigma - V_T k_Z\left[\left(\frac{f k_Z}{k_h}\right)^2 + \Gamma_e\right]\right\} = 0. \tag{8.7}$$

In the below subsections, we discuss the form of the eigenmodes associated to the eigenvalores of the characteristic polynomial (8.7) for particular cases: $k_Z = 0$, $V_T = 0$ and $k_Z V_T \neq 0$.

Case $k_Z = 0$.

In this case, the characteristic polynomial is

$$\sigma^2\left(\sigma^2 - \Gamma_s\right) = 0.$$

and the respectively eigenvalues are

$$\sigma^{0,00} = 0, \quad \sigma^{\pm} = \pm\sqrt{\Gamma_s}$$

The corresponding eigenmodes for each eigenvalue are (in the case where $\sigma^{\pm}$ are both real):

$$\phi^0 = \begin{pmatrix} 1 \\ 0 \\ (\Gamma_s - \Gamma_e)^{1/2} \\ |\Gamma_e|^{1/2} \end{pmatrix}, \quad \phi^{00} = \begin{pmatrix} 0 \\ 0 \\ (\Gamma_s - \Gamma_e)^{1/2} \\ |\Gamma_e|^{1/2} \end{pmatrix}, \quad \phi^{\pm} = \begin{pmatrix} 0 \\ \sigma^{\pm} \\ -i\,\mathrm{sign}\,(\Gamma_e)\,|\Gamma_e|^{1/2} \\ -i\,(\Gamma_s - \Gamma_e)^{1/2} \end{pmatrix}.$$

Case $V_T = 0$.

In the absence of rainfall, where $V_T = 0$, the characteristic polynomial is reduced to

$$\sigma^2\left\{\sigma^2 - \left[\left(\frac{f k_Z}{k_h}\right)^2 + \Gamma_s\right]\right\} = 0.$$

and the respectively eigenvalues are

$$\sigma^{0,00} = 0, \sigma^{\pm} = \sqrt{\left(\frac{fk_Z}{k_h}\right)^2 + \Gamma_s}.$$

The corresponding eigenmodes for each eigenvalue are (in the case where $\sigma^{\pm}$ are both real):

$$\phi^0 = \begin{pmatrix} i\left(\Gamma_s - \Gamma_e\right)^{1/2} \\ 0 \\ 0 \\ fk_h^{-1}k_Z \end{pmatrix}, \quad \phi^{00} = \begin{pmatrix} 0 \\ 0 \\ \left(\Gamma_s - \Gamma_e\right)^{1/2} \\ |\Gamma_e|^{1/2} \end{pmatrix}, \quad \phi^{\pm} = \begin{pmatrix} fk_h^{-1}k_Z \\ \sigma^{\pm} \\ -i\,\mathrm{sign}\left(\Gamma_e\right)|\Gamma_e|^{1/2} \\ -i\left(\Gamma_s - \Gamma_e\right)^{1/2} \end{pmatrix}.$$

The eigenmodes of this case are similar to the eigenmodes in the unsaturated case, swapping Γ_u by Γ_s.

Case $k_Z V_T \neq 0$.

The characteristic polynomial (8.6) has a root $\sigma = 0$. Its eigenmode is

$$\phi^0 = \begin{pmatrix} i|\Gamma_e|^{1/2} \\ 0 \\ -fk_h^{-1}k_Z \\ 0 \end{pmatrix}.$$

The above matrix in equation (8.6) is Hermitian when $\mathrm{sign}\left(\Gamma_e\right) = 1$, which implies all the eigenvalues are real. Thus, the equation

$$\sigma^3 + V_T k_Z \sigma^2 - \left[\left(\frac{fk_Z}{k_h}\right)^2 + \Gamma_s\right]\sigma - V_T k_Z \left[\left(\frac{fk_Z}{k_h}\right)^2 + \Gamma_e\right] = 0 \tag{8.8}$$

has three real roots, denoted by $\sigma_{1,2,3}$. The eigenmode for each eigenvalue is

$$\phi^{1,2,3} = \begin{pmatrix} f k_h^{-1} k_Z \left(\sigma_{1,2,3} + V_T k_Z\right) \\ \sigma_{1,2,3} \left(\sigma_{1,2,3} + V_T k_Z\right) \\ -i \,\mathrm{sign}\left(\Gamma_e\right) |\Gamma_e|^{1/2} (\sigma_{1,2,3} + V_T k_Z) \\ i \left(\Gamma_s - \Gamma_e\right)^{1/2} \sigma_{1,2,3} \end{pmatrix}.$$

If $\mathrm{sign}\left(\Gamma_e\right) = -1$, the existence of one real root of the polynomial (8.8) is guaranteed. However, the other roots could be complex, which would correspond to an instability.

Chapter 9

Numerical results

9.1 Introduction

This chapter is devoted to the derivation of a robust and accurate numerical scheme for the derived model (7.1). As usual, periodic boundary conditions are assumed in the horizontal directions and a pseudo-spectral approach with the use of horizontal Fourier transforms is taken. In the vertical direction, the discretization is implemented with the use of staggered grids. However, the stability of the model using the CFL condition could lead to very small timesteps as pointed out in [55]. We follow the approach in [58] to derive a robust and stable numerical scheme that is more appropriate for the present model.

9.2 Decomposition of the numerical flux

We follow the approach in [58] to derive our numerical scheme. For that purpose, we decompose the numerical fluxes of equation (7.1) (in the right-hand side) as its linear and non-linear components, denoted by $L\left[\mathbf{U}'\right]$ and $N\left[\mathbf{U}'\right]$ respectively. That is,

$$\partial_t \mathbf{U}' = \mathbf{F}\left(\mathbf{U}'\right) = L\left[\mathbf{U}'\right] + N\left[\mathbf{U}'\right] \tag{9.1}$$

where $\mathbf{U}' = (\zeta', w', \theta'_e, q'_t)$,

$$L[\mathbf{U}'] = \begin{pmatrix} f\partial_Z(w') + \nu\nabla_\perp^2(\zeta') \\ -f\partial_Z(\psi') + \nu\nabla_\perp^2(w') \\ \kappa_e\nabla_\perp^2(\theta'_e) \\ \kappa_q\nabla_\perp^2(q'_t) \end{pmatrix}, \quad \text{and } N[\mathbf{U}'] = \begin{pmatrix} -J[\psi', \zeta'] \\ -J[\psi', w'] + b' \\ -J[\psi', \theta'_e] - \partial_Z\left(\overline{\theta_e}\right) w' \\ -J[\psi', q'_t] - \partial_Z\left(\overline{q_t}\right) w' + V_T\partial_Z(q'_r) \end{pmatrix}.$$

In the horizontal direction, let assume periodic boundary conditions by a fourier transform

$$\widehat{\mathbf{U}}' := \widehat{\mathbf{U}}'(k_x, k_y, Z, t, T)$$

Based on the above, we obtain the equation

$$\partial_t\widehat{\mathbf{U}}' = \widehat{L}\left[\widehat{\mathbf{U}}'\right] + \widehat{N}\left[\widehat{\mathbf{U}}'\right],$$

where

$$\widehat{L}\left[\widehat{\mathbf{U}}'\right] = \begin{pmatrix} -\nu k_h^2\widehat{\zeta}' + f\partial_Z(\widehat{w}') \\ -\nu k_h^2\widehat{w}' - f\partial_Z\left(\widehat{\psi}'\right) \\ -\kappa_e k_h^2\widehat{\theta}'_e \\ -\kappa_q k_h^2\widehat{q}'_t \end{pmatrix}, \text{ and } \widehat{N}\left[\widehat{\mathbf{U}}'\right] = \begin{pmatrix} -ik_x\widehat{u'\zeta'} - ik_y\widehat{v'\zeta'} \\ -ik_x\widehat{u'w'} - ik_y\widehat{v'w'} + \widehat{b}' \\ -ik_x\widehat{u'\theta'_e} - ik_y\widehat{v'\theta'_e} - \partial_Z\left(\overline{\theta_e}\right)\widehat{w}' \\ -ik_x\widehat{u'q'_t} - ik_y\widehat{v'q'_t} - \partial_Z\left(\overline{q_t}\right)\widehat{w}' + V_T\partial_Z\left(\widehat{q_r}'\right) \end{pmatrix}.$$

The implicit scheme to advance from $\widehat{\mathbf{U}}'_n$, at time t, to $\widehat{\mathbf{U}}'_{n+1}$, at time $t + \Delta t^{(n)}$, has three substeps:

$$\begin{aligned} \widehat{\mathbf{U}}'_{n+\frac{1}{3}} &= H_n &+ \beta_1\Delta t^{(n)}\widehat{L}\left[\widehat{\mathbf{U}}'_{n+\frac{1}{3}}\right], \\ \widehat{\mathbf{U}}'_{n+\frac{2}{3}} &= H_{n+\frac{1}{3}} &+ \beta_2\Delta t^{(n)}\widehat{L}\left[\widehat{\mathbf{U}}'_{n+\frac{2}{3}}\right], \\ \widehat{\mathbf{U}}'_{n+1} &= H_{n+\frac{2}{3}} &+ \beta_3\Delta t^{(n)}\widehat{L}\left[\widehat{\mathbf{U}}'_{n+1}\right], \end{aligned} \tag{9.2}$$

where

$$\begin{aligned} H_n &= \widehat{\mathbf{U}}'_n &+\alpha_1\Delta t^{(n)}\widehat{L}\left[\widehat{\mathbf{U}}'_n\right] &+\gamma_1\Delta t^{(n)}\widehat{N}\left[\widehat{\mathbf{U}}'_n\right], \\ H_{n+\frac{1}{3}} &= \widehat{\mathbf{U}}'_{n+\frac{1}{3}} &+\alpha_2\Delta t^{(n)}\widehat{L}\left[\widehat{\mathbf{U}}'_{n+\frac{1}{3}}\right] &+\gamma_2\Delta t^{(n)}\widehat{N}\left[\widehat{\mathbf{U}}'_{n+\frac{1}{3}}\right] &+\eta_1\Delta t^{(n)}\widehat{N}\left[\widehat{\mathbf{U}}'_n\right], \\ H_{n+\frac{2}{3}} &= \widehat{\mathbf{U}}'_{n+\frac{2}{3}} &+\alpha_3\Delta t^{(n)}\widehat{L}\left[\widehat{\mathbf{U}}'_{n+\frac{2}{3}}\right] &+\gamma_3\Delta t^{(n)}\widehat{N}\left[\widehat{\mathbf{U}}'_{n+\frac{2}{3}}\right] &+\eta_2\Delta t^{(n)}\widehat{N}\left[\widehat{\mathbf{U}}'_{n+\frac{1}{3}}\right]. \end{aligned} \tag{9.3}$$

The suggested values of α, β, γ and η are

$$\alpha_1 = \frac{29}{96}, \alpha_2 = -\frac{3}{40}, \alpha_3 = \frac{1}{6},$$

$$\beta_1 = \frac{37}{160}, \beta_2 = \frac{5}{24}, \beta_3 = \frac{1}{6},$$
$$\gamma_1 = \frac{8}{15}, \beta_2 = \frac{5}{12}, \beta_3 = \frac{3}{4},$$
$$\eta_1 = -\frac{17}{60}, \beta_2 = -\frac{5}{12}.$$

For each substep $k = 1, 2, 3$, we rewrite the system as

$$\begin{aligned}
\left[1 + \nu\beta_k \Delta t^{(n)} k_h^2\right] \widehat{\zeta}'^{n+\frac{k}{3}} - f\beta_k \Delta t^{(n)} \partial_Z \left(\widehat{w}'^{n+\frac{k}{3}}\right) &= H^{(1)}_{n+\frac{k-1}{3}}, \\
\left[1 + \nu\beta_k \Delta t^{(n)} k_h^2\right] \widehat{w}'^{n+\frac{k}{3}} + f\beta_k \Delta t^{(n)} \partial_Z \left(\widehat{\psi}'^{n+\frac{k}{3}}\right) &= H^{(2)}_{n+\frac{k-1}{3}}, \\
\left[1 + \kappa_e\beta_k \Delta t^{(n)} k_h^2\right] \widehat{\theta}_e^{\,\prime n+\frac{k}{3}} &= H^{(3)}_{n+\frac{k-1}{3}}, \\
\left[1 + \kappa_q\beta_k \Delta t^{(n)} k_h^2\right] \widehat{q}_t^{\,\prime n+\frac{k}{3}} &= H^{(4)}_{n+\frac{k-1}{3}}.
\end{aligned} \tag{9.4}$$

We note that $\widehat{\theta}_e^{\,\prime n+\frac{k}{3}}$ and $\widehat{q}_t^{\,\prime n+\frac{k}{3}}$ can be obtained explicitly by the relations

$$\widehat{\theta}_e^{\,\prime n+\frac{k}{3}} = \frac{1}{1 + \kappa_e\beta_k \Delta t^{(n)} k_h^2} H^{(3)}_{n+\frac{k-1}{3}},$$

$$\widehat{q}_t^{\,\prime n+\frac{k}{3}} = \frac{1}{1 + \kappa_q\beta_k \Delta t^{(n)} k_h^2} H^{(4)}_{n+\frac{k-1}{3}}.$$

The solution for $\widehat{\zeta}'^{n+\frac{k}{3}}$ and $\widehat{w}'^{n+\frac{k}{3}}$ are done through a decomposition of the vertical axis Z intro a staggered grid, as it will be presented in the next section.

9.3 Staggered grid for vertical integration

The vertical-integration of the model will be done introducing a sttagered grid, in order to discretizise better the derivatives in Z-direction. Let define the sttagered grid as

$$Z_j^w = (j-1)\,\Delta Z, \quad Z_j^u = \left(j - \frac{1}{2}\right)\Delta Z,$$

where $Z_1^w = 0$ and $Z_{m+1}^w = L$. The variables u', v', ζ', $\overline{\theta_e}$ and $\overline{q_t}$ are defined in the grid Z_j^u, while the variables w', q_t' and θ_e' are defined at the grid Z_j^w. Let us observe that the grid Z_j^u has ghost cells ($Z_0^u = -\frac{\Delta Z}{2}$ and $Z_{m+1}^u = L + \frac{\Delta Z}{2}$). On the other hand, the grid

Z_j^w do not have ghost cells, except for the boundaries. See Figure 9.1 for a schematic of the grid.

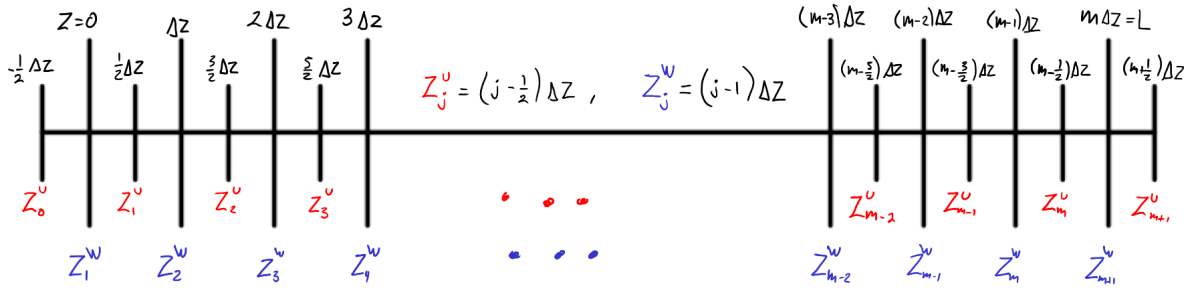

FIGURE 9.1: Schematic of the staggered grid for the model.

We have the following relations:

$$Z_j^w = \frac{1}{2}\left(Z_j^u + Z_{j-1}^u\right), \quad Z_j^u = \frac{1}{2}\left(Z_j^w + Z_{j+1}^w\right)$$

The discretization of $\partial_Z\left(\widehat{w}'\right)$ and $\partial_Z\left(\widehat{\psi}'\right)$ are

$$\partial_Z\left(\widehat{w}'\right)\left(Z_j^u\right) = \frac{\widehat{w}'\left(Z_{j+1}^w\right) - \widehat{w}'\left(Z_j^w\right)}{\Delta Z},$$

$$\partial_Z\left(\widehat{\psi}'\right)\left(Z_j^w\right) = \frac{\widehat{\psi}'\left(Z_j^u\right) - \widehat{\psi}'\left(Z_{j-1}^u\right)}{\Delta Z}.$$

Equation (9.4) is rewritten as

$$\begin{aligned}
&\left[1 + \nu\beta_k \Delta t^{(n)} k_h^2\right] \widehat{\zeta}'^{n+\frac{k}{3}}\left(Z_j^u\right) \\
&-\frac{f\beta_k \Delta t^{(n)}}{\Delta Z}\left[\widehat{w}'^{n+\frac{k}{3}}\left(Z_{j+1}^w\right) - \widehat{w}'^{n+\frac{k}{3}}\left(Z_j^w\right)\right] \quad = \quad H_{n+\frac{k-1}{3}}^{(1)}\left(Z_j^u\right), \\
&\left[1 + \nu\beta_k \Delta t^{(n)} k_h^2\right] \widehat{w}'^{n+\frac{k}{3}}\left(Z_j^w\right) \\
&+\frac{f\beta_k \Delta t^{(n)}}{\Delta Z}\left[\widehat{\psi}'^{n+\frac{k}{3}}\left(Z_j^u\right) - \widehat{\psi}'^{n+\frac{k}{3}}\left(Z_{j-1}^u\right)\right] \quad = \quad H_{n+\frac{k-1}{3}}^{(2)}\left(Z_j^w\right).
\end{aligned} \tag{9.5}$$

The above equations can be solved using a tridiagonal system for $\widehat{w}'^{n+\frac{k}{3}}$:

$$\begin{pmatrix} b & a & 0 & 0 & \dots & 0 & 0 & 0 \\ a & b & a & 0 & \dots & 0 & 0 & 0 \\ 0 & a & b & a & \dots & 0 & 0 & 0 \\ 0 & 0 & a & b & \dots & 0 & 0 & 0 \\ \vdots & \vdots & \vdots & \vdots & \ddots & \vdots & \vdots & \vdots \\ 0 & 0 & 0 & 0 & \dots & b & a & 0 \\ 0 & 0 & 0 & 0 & \dots & a & b & a \\ 0 & 0 & 0 & 0 & \dots & 0 & a & b \end{pmatrix} \begin{pmatrix} \widehat{w}'^{n+\frac{k}{3}}\left(Z_2^w\right) \\ \widehat{w}'^{n+\frac{k}{3}}\left(Z_3^w\right) \\ \widehat{w}'^{n+\frac{k}{3}}\left(Z_4^w\right) \\ \widehat{w}'^{n+\frac{k}{3}}\left(Z_5^w\right) \\ \vdots \\ \widehat{w}'^{n+\frac{k}{3}}\left(Z_{m-2}^w\right) \\ \widehat{w}'^{n+\frac{k}{3}}\left(Z_{m-1}^w\right) \\ \widehat{w}'^{n+\frac{k}{3}}\left(Z_m^w\right) \end{pmatrix} = \begin{pmatrix} c_{n,k}\left(Z_2^w\right) \\ c_{n,k}\left(Z_3^w\right) \\ c_{n,k}\left(Z_4^w\right) \\ c_{n,k}\left(Z_5^w\right) \\ \vdots \\ c_{n,k}\left(Z_{m-2}^w\right) \\ c_{n,k}\left(Z_{m-1}^w\right) \\ c_{n,k}\left(Z_m^w\right) \end{pmatrix} \tag{9.6}$$

with

$$\begin{aligned} a &= -\left(\frac{f\beta_k\Delta t^{(n)}}{\Delta Z}\right)^2, \\ b &= \left[2\left(\frac{f\beta_k\Delta t^{(n)}}{\Delta Z}\right)^2 - k_h^2\left[1+\nu\beta_k\Delta t^{(n)}k_h^2\right]^2\right], \\ c_{n,k}\left(Z_j^w\right) &= -k_h^2\left[1+\nu\beta_k\Delta t^{(n)}k_h^2\right]H^{(2)}_{n+\frac{k-1}{3}}\left(Z_j^w\right) \\ &\quad + \frac{f\beta_k\Delta t^{(n)}}{\Delta Z}\left[H^{(1)}_{n+\frac{k-1}{3}}\left(Z_j^u\right) - H^{(1)}_{n+\frac{k-1}{3}}\left(Z_{j-1}^u\right)\right], \end{aligned} \tag{9.7}$$

and the boundaries condition $w\left(Z_1^w\right) = w\left(Z_{m+1}^w\right) = 0$. After that, we solve for $\widehat{\zeta}^{n+\frac{k}{3}}$ using equation (9.5).

9.4 Numerical tests

9.4.1 Dipole coherent structure

In this section, we provide numerical tests to exhibit part of the dynamics that geophysical flows follows under the assumptions (7.7) of the model (7.1). A first case is based on a dipole coherent structure. In [59], dipole coherent structures are provided and analyzed. For the standard (dry) quasi-geostrophic equations, dipoles represent solutions that propagate as a coherent structure. Here we consider a dipole coherent structure in the presence of moisture.

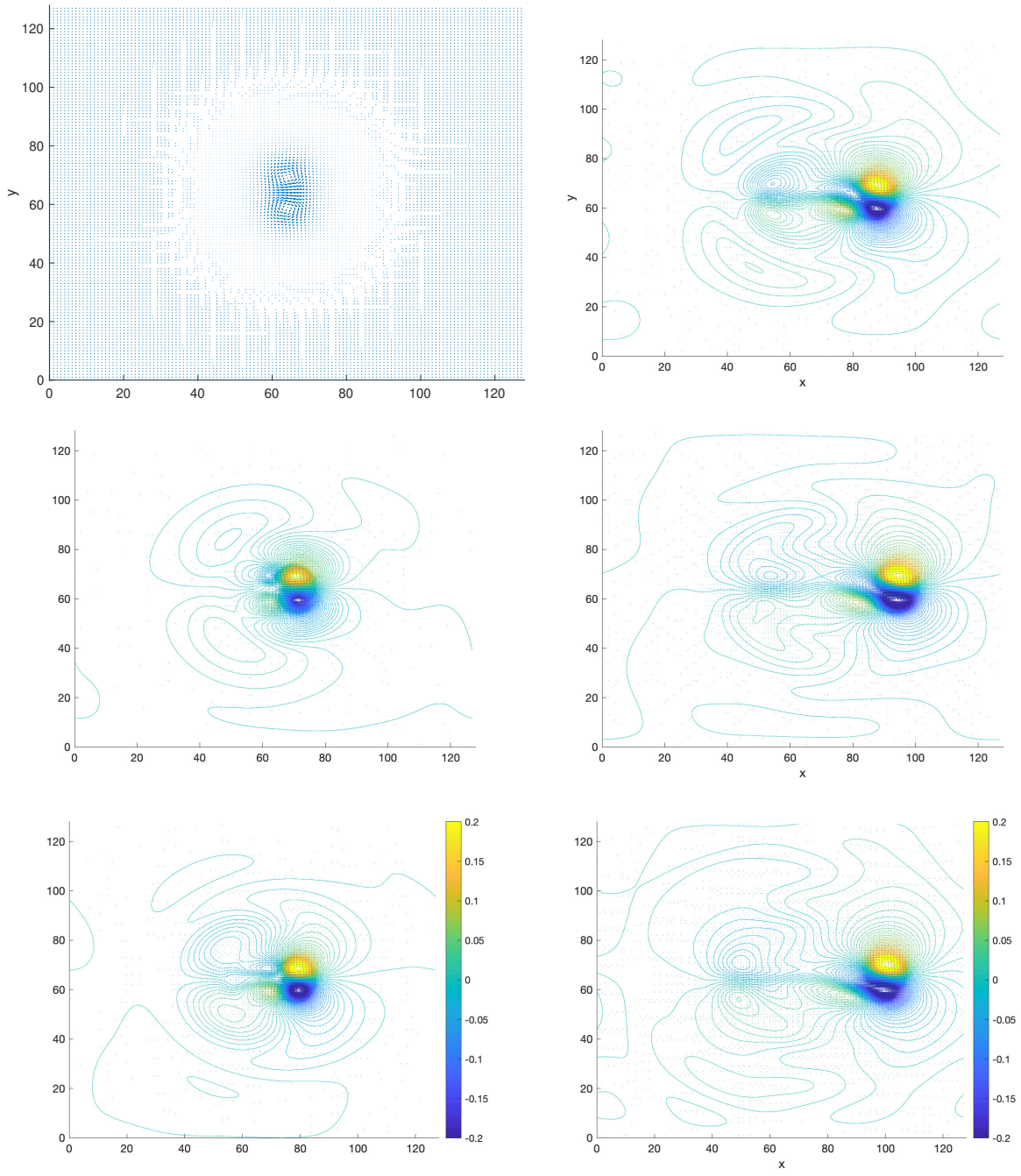

FIGURE 9.2: Horizontal contours of water vapour and velocity field are shown at times $T = 0$ (top left panel), $T = 1$ h (middle left), $T = 2$ h (bottom left), $T = 3$ h (top right), $T = 4$ (middle right) and $T = 5$ h (bottom right). The arrows indicate the velocity field.

The initial conditions are given by a streamfunction satisfying

$$\Delta\psi = s\exp\left(-\frac{(x-x_0)^2+(y-a_2)^2+(z-h_2)^2}{2\gamma}\right) - s\exp\left(-\frac{(x-x_o)^2+(y-a_1)^2+(z-h_1)^2}{2\gamma}\right),$$

where $s = 2$ is the strength's amplitude of the dipole, $\gamma = 0.05$, $x_o = 64$ km, $a = 10$ km,

$a_1 = 64$ km $- \frac{a}{2}$, $a_2 = 64$ km $+ \frac{a}{2}$, $h_1 = 5$ km $- \frac{h}{2}$, $h_2 = 5$ km $+ \frac{h}{2}$, $h = 0.6$ km. The solution is computed on a domain of size $[0, 128\text{ km}] \times [0, 128\text{ km}] \times [0, 15\text{ km}]$.

The horizontal velocity field is initiated in terms of the streamfunction as

$$u = -\partial_y \psi,\ v = \partial_x \psi,\ w = 0.$$

Following the relations for balanced flows in the dry case, here we initiate the equivalent potential temperature as

$$\theta_e = \frac{f}{N} \partial_z \psi.$$

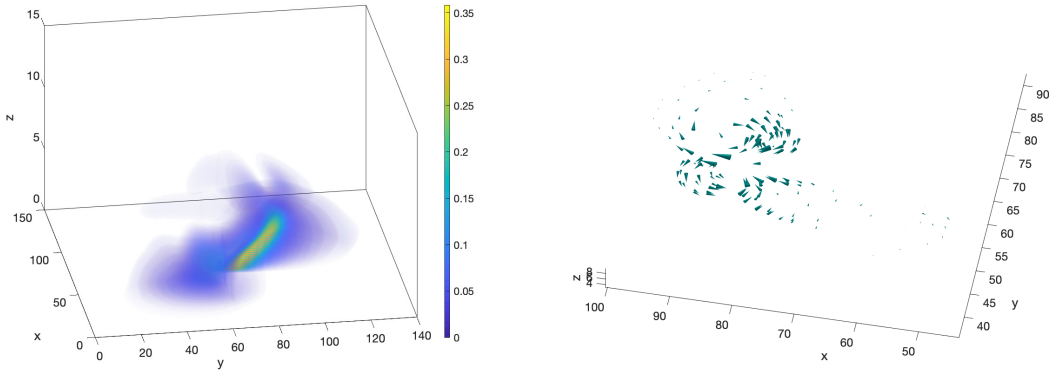

FIGURE 9.3: Left panel: Three dimensional slices of water vapor. Right panel: 3D velocity field near the edge of the vapor bubble. The arrows indicate the velocity field.

The time evolution is shown in Figure 9.2. Horizontal contours of what vapor fluctuations are shown in Figure 9.2. As expected, one can see the dipole propagates eastward as a coherent structure. Such dipoles structures have been studied in many different contexts because of their importance. For instance, dipole-type coherent structures can appear in atmospheric phenomena involving deep convection [60]. Although it is an idealized dipole, the current reduced model derived in this thesis can capture such coherent structure, which propagates in the correct direction.

One advantage of the reduced model presented here is the ability to include moist in the dynamics of the fluid. This is particularly important for applications involving deep convection. In this numerical test, the water vapor has a background state that decreases exponentially with height. See [54] for more details. Furthermore, we perturbe this states

by adding a vapor bubble given by

$$q_v(x, y, z, t = 0) =$$

$$= \begin{cases} 0.2 \text{ g kg}^{-1} \cos\left(\pi \frac{r}{r_c}\right) \left(\frac{z - z_c - 1 \text{ km}}{\text{km}}\right)^2 \left(\frac{z - z_c + 1 \text{ km}}{\text{km}}\right)^2, & \text{if} \quad r \leq r_c, |z - z_c| \leq 1 \text{ km}, \\ 0 & \text{otherwise.} \end{cases}$$

Here,

$$r = \sqrt{(x - x_c)^2 + (y - y_c)^2}$$

is the distance from the center $(x_c, y_c) = (64 \text{ km}, 64 \text{ km})$, and $z_c = 5$ km. The boundary conditions implemented in this numerical test are as follows. In the horizontal direction, we impose periodic boundary conditions. In the vertical direction, the vertical velocity vanishes at the tropopause and at the surface, while the rest of the variables satisfy zero Neumann boundary conditions.

Figure 9.3 shows a 3D plot of the moisture in the fluid at time $t = 5$h. In particular, the left panel shows 3D slices of water vapor. One can observe that the initial column is dragged by the coherent structure. Rain forms initially but is stays weak before it disappears. It may indicate to use that under the present parameter regime and conditions, rain is suppressed by the lack of fast gravity waves. In order to identify the 3D structure of the dipole, the right panel shows the velocity field near the edge of the cloud. It is oriented differently to identify the field. Two vortices, one cyclonic and one anti-cyclonic can be identified.

9.4.2 Random initial conditions

The present numerical test considers random fluctuations in the potential temperature. In this context, the variables have been non-dimensionalized by dividing by characteristic values. Here, the Reynold and Peclet numbers are Re = 20, $\text{PE}^\theta = 7$, $\text{PE}^q = 1$ respectively. The background states are as follows. A reference potential temperature of $\theta_o = 1$ is chosen at the surface. A reference value of 2 for the water vapor background is chosen at the surface.

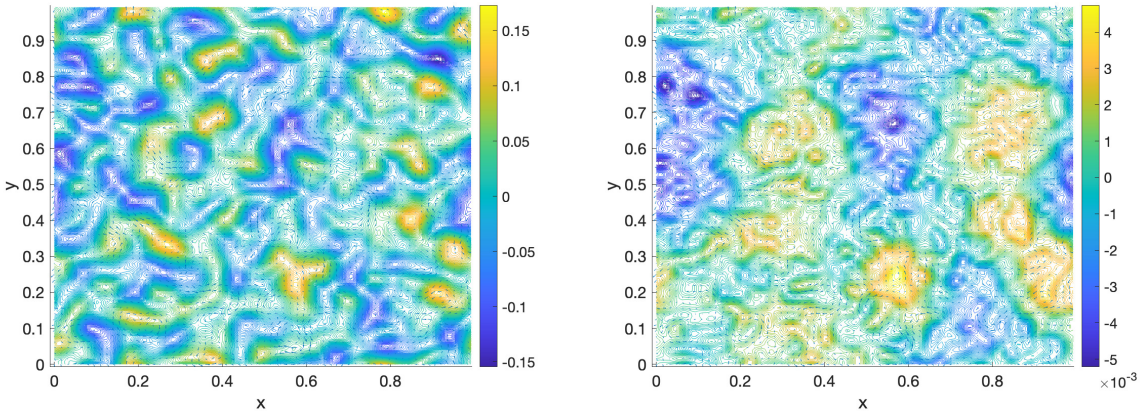

FIGURE 9.4: Left panel: Horizontal contours of potential temperature at $t = 2$ units, $z = L_z/2$. Right panel: the corresponding plot for the water vapor is shown. The arrows indicate the velocity field.

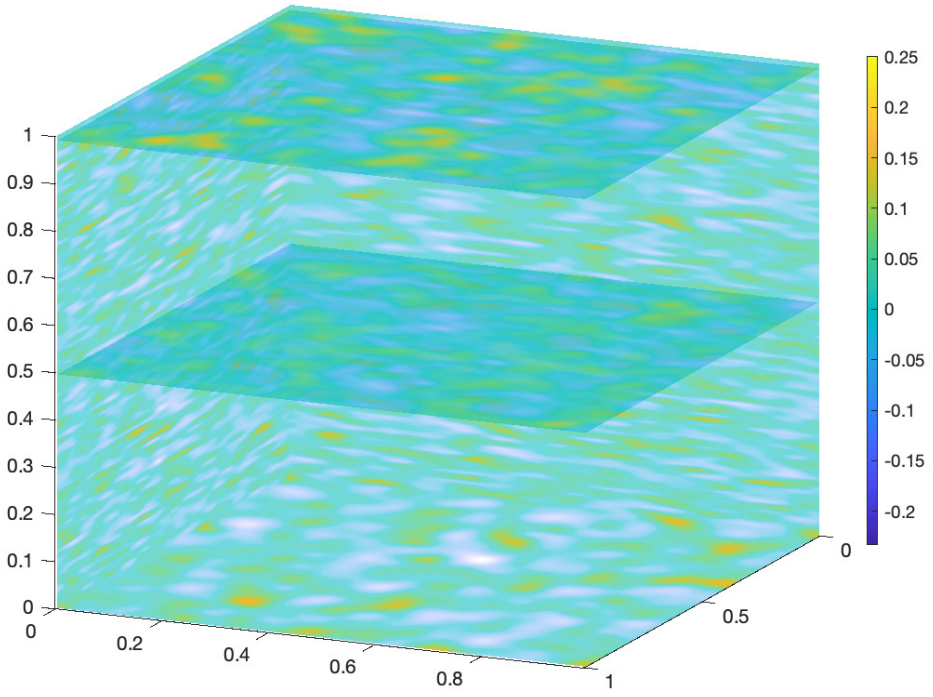

FIGURE 9.5: Contours of potential temperature at the walls and at intermediate heights are shown to help with the 3D visualization.

The initial potential temperature has fluctuations taken from a random uniform distribution where the maximum amplitudes is 0.5 . The left panel of Figure 9.4 shows horizontal contours of this variable after 2 time units, at a height $z = L_z/2$ (in the middle of the

domain). One can observe the formation of coherent structures. The velocity field indicated by the arrows shows the formation of vortices as well. The right panel exhibits contours of water vapor. It shows again the formation of coherent structures.

On the other hand, Figure 9.5 shows contours of potential temperature at the walls and at intermediate heights. This 3D visualization allows us to observe the formation of coherent structures as well as its distribution. Following [55], we choose the horizontal domain size as $L_h = 20 \times 4.8154$ and the vertical extent is $L_z = 1$. We use 128^2 grid points in the horizontal direction with 100 levels in the vertical direction. The rainfall velocity is $V_T^* = 1$. In a future investigation, we will explore different parameter regimes and its response to a variety of Reynold and Peclet numbers.

Conclusions

In the second part of the thesis, we derived a reduced model that generalizes the concept of quasi-geostrophy, including moisture dynamics. The limiting dynamics is valid for situations where the vertical extend is large when compared to the horizontal lengthscale. This is typical for vortical hot towers, which are a coherent structure that appears in a hurricane embryo.

A numerical scheme was presented to compute the approximated solutions. Furthermore, two numerical tests were considered. The first one considered a dipole coherent structure with water vapor in it. The structure propagates in the right direction. The lack of rain in the dynamics might indicate that the exclusion of some gravity waves could suppress the formation of rain. The second idealized test consists of random initial conditions in the potential temperature. It also shows the formation of coherent structures.

In a future work, a deeper numerical investigation will be conducted to explore the qualitative behavior of the solutions under different parameter regimes.

References

[1] Shanthi Mendis, Pekka Puska, Bo Norrving, World Health Organization, et al. *Global atlas on cardiovascular disease prevention and control*. World Health Organization, 2011.

[2] Luca Formaggia, Fabio Nobile, ALFIO Quarteroni, Alessandro Veneziani, and Paolo Zunino. Advances on numerical modelling of blood flow problems. In *European Congress on Computational Methods in Applied Sciences and Engineering (ECCOMAS 2000)*, pages 11–14, 2000.

[3] A. Quarteroni, A. Manzoni, and C. Vergara. The cardiovascular system: Mathematical modelling, numerical algorithms and clinical applications. *Acta Numerica*, 26: 365–590, 2017. doi: 10.1017/S0962492917000046.

[4] Alfio Quarteroni and Luca Formaggia. Mathematical modelling and numerical simulation of the cardiovascular system. *Handbook of numerical analysis*, 12:3–127, 2004.

[5] Christopher J Arthurs, Rostislav Khlebnikov, Alex Melville, Marija Marčan, Alberto Gomez, Desmond Dillon-Murphy, Federica Cuomo, Miguel Silva Vieira, Jonas Schollenberger, Sabrina R Lynch, et al. Crimson: An open-source software framework for cardiovascular integrated modelling and simulation. *PLOS Computational Biology*, 17(5):e1008881, 2021.

[6] David N Ku, Don P Giddens, Christopher K Zarins, and Seymour Glagov. Pulsatile flow and atherosclerosis in the human carotid bifurcation. positive correlation between plaque location and low oscillating shear stress. *Arteriosclerosis, thrombosis, and vascular biology*, 5(3):293–302, 1985.

[7] C.A. Taylor and C.A. Figueroa. Patient-specific modeling of cardiovascular mechanics. *Annual Review of Biomedical Engineering*, 11(1):109–134, 2009. doi: 10.1146/annurev.bioeng.10.061807.160521. URL https://doi.org/10.1146/annurev.bioeng.10.061807.160521. PMID: 19400706.

[8] Luca Formaggia, Daniele Lamponi, and Alfio Quarteroni. One-dimensional models for blood flow in arteries. *Journal of Engineering Mathematics*, 47(3):251–276, Dec 2003. ISSN 1573-2703. doi: 10.1023/B:ENGI.0000007980.01347.29. URL https://doi.org/10.1023/B:ENGI.0000007980.01347.29.

[9] Sunčica Čanić and Eun Heui Kim. Mathematical analysis of the quasilinear effects in a hyperbolic model blood flow through compliant axi-symmetric vessels. *Mathematical Methods in the Applied Sciences*, 26(14):1161–1186, 2003.

[10] Sunčica Čanić. Blood flow through compliant vessels after endovascular repair: wall deformations induced by the discontinuous wall properties. *Computing and Visualization in Science*, 4(3):147–155, 2002. ISSN 1432-9360. doi: 10.1007/s007910100066. URL https://doi.org/10.1007/s007910100066.

[11] Sunčica Čanić, Craig J Hartley, Doreen Rosenstrauch, Josip Tambača, Giovanna Guidoboni, and Andro Mikelić. Blood flow in compliant arteries: an effective viscoelastic reduced model, numerics, and experimental validation. *Annals of Biomedical Engineering*, 34(4):575–592, 2006.

[12] Suncica Canic, Matea Galovic, Matko Ljulj, and Josip Tambaca. A dimension-reduction based coupled model of mesh-reinforced shells. *SIAM Journal on Applied Mathematics*, 77(2):744–769, 2017.

[13] Lucas O. Müller, Carlos Parés, and Eleuterio F. Toro. Well-balanced high-order numerical schemes for one-dimensional blood flow in vessels with varying mechanical properties. *Journal of Computational Physics*, 242:53 – 85, 2013. ISSN 0021-9991. doi: https://doi.org/10.1016/j.jcp.2013.01.050. URL http://www.sciencedirect.com/science/article/pii/S0021999113001277.

[14] Eleuterio F. Toro Gino I. Montecinos, Lucas O Müller. Hyperbolic reformulation of a 1d viscoelastic blood flow model and ader finite volume schemes. *Journal of Computational Physics*, 266:101–123, 2014.

[15] PJ Blanco LO Müller, G Leugering. Consistent treatment of viscoelastic effects at junctions in one-dimensional blood flow models. *Journal of Computational Physics*, 314:167–193, June 2016.

[16] Marie Willemet and Jordi Alastruey. Arterial pressure and flow wave analysis using time-domain 1-d hemodynamics. *Annals of Biomedical Engineering*, 43(1):190–206, Jan 2015. ISSN 1573-9686. doi: 10.1007/s10439-014-1087-4. URL `https://doi.org/10.1007/s10439-014-1087-4`.

[17] Frans N. van de Vosse and Nikos Stergiopulos. Pulse wave propagation in the arterial tree. *Annual Review of Fluid Mechanics*, 43(1):467–499, 2011. doi: 10.1146/annurev-fluid-122109-160730. URL `https://doi.org/10.1146/annurev-fluid-122109-160730`.

[18] David N. Ku. Blood flow in arteries. *Annual Review of Fluid Mechanics*, 29(1):399–434, 1997. doi: 10.1146/annurev.fluid.29.1.399. URL `https://doi.org/10.1146/annurev.fluid.29.1.399`.

[19] Wouter Huberts, Koen Van Canneyt, Patrick Segers, Sunny Eloot, JHM Tordoir, Pascal Verdonck, FN van De Vosse, and EMH Bosboom. Experimental validation of a pulse wave propagation model for predicting hemodynamics after vascular access surgery. *Journal of biomechanics*, 45(9):1684–1691, 2012.

[20] John M Wallace and Peter V Hobbs. *Atmospheric science: an introductory survey*, volume 92. Elsevier, 2006.

[21] Paul A Dirmeyer, C Adam Schlosser, and Kaye L Brubaker. Precipitation, recycling, and land memory: An integrated analysis. *Journal of Hydrometeorology*, 10(1):278–288, 2009.

[22] Lewis F Richardson. *Weather prediction by numerical process*. University Press, 1922.

[23] Jule G Charney. On the scale of atmospheric motions. In *The Atmosphere?A Challenge*, pages 251–265. Springer, 1990.

[24] Jacques Vanneste. Balance and spontaneous wave generation in geophysical flows. *Annual review of fluid mechanics*, 45:147–172, 2013.

[25] Mark Remmel, Jai Sukhatme, and Leslie M Smith. Nonlinear inertia-gravity wave-mode interactions in three dimensional rotating stratified flows. *arXiv preprint arXiv:0903.0693*, 2009.

[26] Jai Sukhatme and Leslie M Smith. Vortical and wave modes in 3d rotating stratified flows: random large-scale forcing. *Geophysical and Astrophysical Fluid Dynamics*, 102(5):437–455, 2008.

[27] Gerardo Hernandez-Duenas, Leslie M Smith, and Samuel N Stechmann. Investigation of boussinesq dynamics using intermediate models based on wave–vortical interactions. *Journal of fluid mechanics*, 747:247–287, 2014.

[28] Leslie M Smith and Samuel N Stechmann. Precipitating quasigeostrophic equations and potential vorticity inversion with phase changes. *Journal of the Atmospheric Sciences*, 74(10):3285–3303, 2017.

[29] Alfredo N Wetzel, Leslie M Smith, and Samuel N Stechmann. Moisture transport due to baroclinic waves: Linear analysis of precipitating quasi-geostrophic dynamics. *Mathematics of Climate and Weather Forecasting*, 3(1):28–50, 2017.

[30] Keith Julien, Edgar Knobloch, Ralph Milliff, and Joseph Werne. Generalized quasi-geostrophy for spatially anisotropic rotationally constrained flows. *Journal of Fluid Mechanics*, 555:233–274, 2006.

[31] Randall J LeVeque and Randall J Leveque. *Numerical methods for conservation laws*, volume 214. Springer, 1992.

[32] William F Ames. *Numerical methods for partial differential equations*. Academic press, 2014.

[33] Randall J LeVeque et al. *Finite volume methods for hyperbolic problems*, volume 31. Cambridge university press, 2002.

[34] François Bouchut. *Nonlinear stability of finite Volume Methods for hyperbolic conservation laws: And Well-Balanced schemes for sources*. Springer Science & Business Media, 2004.

[35] Gerald Warnecke. *Analysis and numerics for conservation laws*. Springer, 2005.

[36] Edwige Godlewski and Pierre-Arnaud Raviart. *Numerical approximation of hyperbolic systems of conservation laws*, volume 118. Springer Science & Business Media, 2013.

[37] Bruno Després. *Numerical methods for Eulerian and Lagrangian conservation laws*. Birkhäuser, 2017.

[38] Alexandre Joel Chorin and Jerrold E Marsden. *A mathematical introduction to fluid mechanics*, volume 3. Springer, 1990.

[39] NP Smith, AJ Pullan, and Peter J Hunter. An anatomically based model of transient coronary blood flow in the heart. *SIAM Journal on Applied mathematics*, 62(3):990–1018, 2002.

[40] Nikolay Bessonov, Adélia Sequeira, Sergey Simakov, Yu Vassilevskii, and Vitaly Volpert. Methods of blood flow modelling. *Mathematical modelling of natural phenomena*, 11(1):1–25, 2016.

[41] Nan Xiao, Jordi Alastruey, and C Alberto Figueroa. A systematic comparison between 1-d and 3-d hemodynamics in compliant arterial models. *International journal for numerical methods in biomedical engineering*, 30(2):204–231, 2014.

[42] AJ Geers, I Larrabide, HG Morales, and AF Frangi. Comparison of steady-state and transient blood flow simulations of intracranial aneurysms. In *2010 Annual International Conference of the IEEE Engineering in Medicine and Biology*, pages 2622–2625. IEEE, 2010.

[43] Alexander Kurganov, Sebastian Noelle, and Guergana Petrova. Semidiscrete central-upwind schemes for hyperbolic conservation laws and hamilton–jacobi equations. *SIAM Journal on Scientific Computing*, 23(3):707–740, 2001.

[44] S. Gottlieb, C.-W. Shu, and E. Tadmor. Strong stability-preserving high-order time discretization methods. *SIAM Rev.*, 43(1):89–112 (electronic), 2001. ISSN 0036-1445. doi: 10.1137/S003614450036757X. URL `http://dx.doi.org/10.1137/S003614450036757X`.

[45] Alexander Kurganov, Guergana Petrova, et al. A second-order well-balanced positivity preserving central-upwind scheme for the saint-venant system. *Communications in Mathematical Sciences*, 5(1):133–160, 2007.

[46] Faidon Kyriakou, William Dempster, and David Nash. Analysing the cross-section of the abdominal aortic aneurysm neck and its effects on stent deployment. *Scientific reports*, 10(1):1–12, 2020.

[47] Daniel Ho, Andrew Squelch, and Zhonghua Sun. Modelling of aortic aneurysm and aortic dissection through 3d printing. *Journal of medical radiation sciences*, 64(1): 10–17, 2017.

[48] FPP Tan, A Borghi, RH Mohiaddin, NB Wood, S Thom, and XY Xu. Analysis of flow patterns in a patient-specific thoracic aortic aneurysm model. *Computers & Structures*, 87(11-12):680–690, 2009.

[49] Ricardo Luis Armentano, Juan Gabriel Barra, Jaime Levenson, Alain Simon, and Ricardo Horacio Pichel. Arterial wall mechanics in conscious dogs: assessment of viscous, inertial, and elastic moduli to characterize aortic wall behavior. *Circulation research*, 76(3):468–478, 1995.

[50] Edward A Spiegel and G Veronis. On the boussinesq approximation for a compressible fluid. *The Astrophysical Journal*, 131:442, 1960.

[51] Benoit Cushman-Roisin and Jean-Marie Beckers. *Introduction to geophysical fluid dynamics: physical and numerical aspects*. Academic press, 2011.

[52] Kerry A Emanuel et al. *Atmospheric convection*. Oxford University Press on Demand, 1994.

[53] Qiang Deng, Leslie Smith, and Andrew Majda. Tropical cyclogenesis and vertical shear in a moist boussinesq model. *Journal of fluid mechanics*, 706:384–412, 2012.

[54] Gerardo Hernandez-Duenas, Andrew J Majda, Leslie M Smith, and Samuel N Stechmann. Minimal models for precipitating turbulent convection. *Journal of Fluid Mechanics*, 717:576–611, 2013.

[55] Michael Sprague, Keith Julien, Edgar Knobloch, and Joseph Werne. Numerical simulation of an asymptotically reduced system for rotationally constrained convection. *Journal of Fluid Mechanics*, 551:141–174, 2006.

[56] Keith Julien, Edgar Knobloch, and Joseph Werne. A new class of equations for rotationally constrained flows. *Theoretical and computational fluid dynamics*, 11 (3-4):251–261, 1998.

[57] Gerardo Hernandez-Duenas, Leslie M Smith, and Samuel N Stechmann. Stability and instability criteria for idealized precipitating hydrodynamics. *Journal of the Atmospheric Sciences*, 72(6):2379–2393, 2015.

[58] Philippe R Spalart, Robert D Moser, and Michael M Rogers. Spectral methods for the navier-stokes equations with one infinite and two periodic directions. *Journal of Computational Physics*, 96(2):297–324, 1991.

[59] GR Flierl. Isolated eddy models in geophysics. *Annual Review of Fluid Mechanics*, 19(1):493–530, 1987.

[60] Matthew H Hitchman and Shellie M Rowe. On the similarity of lower-stratospheric potential vorticity dipoles above tropical and midlatitude deep convection. *Journal of the Atmospheric Sciences*, 74(8):2593–2613, 2017.